Optically Accessible Spin Qubits in ZnO

Vasileios Niaouris

A dissertation
submitted in partial fulfillment of the
requirements for the degree of

Doctor of Philosophy

University of Washington

2024

Reading Committee:
Kai-Mei C. Fu, Chair
Boris B. Blinov
Maxwell F. Parsons

Program Authorized to Offer Degree:
Physics

University of Washington

Abstract

Optically Accessible Spin Qubits in ZnO

Vasileios Niaouris

Chair of the Supervisory Committee:
Kai-Mei C. Fu
Physics

Quantum information science has witnessed significant advancements in the pursuit of fault-tolerant quantum computers with growing emphasis on realizing large-scale quantum networks. However, the community has yet to identify a single or composite quantum system that will enable robust and scalable quantum communication technologies. Among a plethora of candidates, the neutral shallow donor in zinc oxide (ZnO) has recently emerged as a promising platform due to its unique combination of efficient light-matter interaction and potential for long coherence times.

In this dissertation, we present a comprehensive study of the spin and optical properties of aluminum (Al), gallium (Ga), and indium (In) donors in natural isotopic abundance ZnO, with an emphasis on assessing their suitability for photon-based quantum networks. Using optical spin initialization via the donor-bound exciton, we demonstrate ensemble longitudinal spin relaxation times nearing half a second, which suggests a great potential for long transverse spin relaxation (coherence) times in isotopically and chemically purified ZnO. Photoluminescence excitation spectroscopy reveals narrow, non-thermally-broadened ensemble optical linewidths (less than two orders of magnitude larger than the lifetime limit) at liquid helium temperatures, further improvable by isotopic and chemical purification. We further showcase that single In emitters can be spatially and spectrally isolated via focused ion beam milling while preserving their favorable optical properties, albeit with reduced

radiative photoluminescence and increased emission inhomogeneity. Finally, we report on the progress of emission frequency tuning by employing the Stark effect, realized via the fabrication of planar capacitors on the host crystal surface.

Our findings, coupled with the potential for subsequent optimization, establish the neutral shallow donor in ZnO as a compelling platform for photon-based quantum technologies. This work underscores the need for the research and development of higher purity ZnO production techniques. It ushers in future research aimed at deciphering and eliminating optical linewidth broadening mechanisms, achieving scalable and deterministic isolation of single emitters, and, ultimately, integrating this platform in both homogeneous and heterogeneous quantum networks.

TABLE OF CONTENTS

LIST OF FIGURES

Figure Number Page

LIST OF TABLES

GLOSSARY

BS: Beam Splitter

BX: Bound Exciton

CMP: Chemical-Mechanical Polish

CPT: Coherent Population Trapping

CW: Continuous Wave

DC: Direct Current

D^0: Neutral donor-bound electron

D^0X: Neutral donor-bound exciton

E-EVAP: Electron-beam EVAPoration

EBL: Electron-Beam Lithography

EIT: Electromagnetically-Induced Transparency

FIB: Focused Ion Beam

FT: Fourier Transform

FWHM: Full Width Half Maximum

FX: Free Exciton

HWP: Half WavePlate

ISD: Instantaneous Spectral Diffusion

LHE: Liquid Helium

LO: Longitudinal Optical Phonon Replica

MBE: Molecular-beam Epitaxy

NA: Numerical Aperture

NIR: Near InfraRed

OP: Optical Pumping

OQM: Optical Quantum Memory

PD: PhotoDiode

PFIB: Plasma Focused Ion Beam

PH: PinHole

PL: Photoluminescence

PLE: Photoluminescence Excitation

QIS: Quantum Information Science

QWP: Quarter WavePlate

QM: Quantum Memory

QN: Quantum Network

REI: Rare Earth Ion

SEM: Scanning Electron Microscopy

SIMS: Secondary Ion Mass Spectroscopy

SPCM: Single Photon Counting Module

T_1: Longitudinal spin relaxation time

T_2: Hahn spin-echo time

T_2^*: Spin dephasing (or transversal relaxation) time

TD: Tokyo Denpa Co. Ltd.

TES: Two Electron Satellite

UV: Ultra Violet

ZPL: Zero-Phonon Line

ACKNOWLEDGMENTS

First and foremost, I would like to express my gratitude to my advisor, Professor Kai-Mei Fu, for their guidance and support throughout my PhD journey. Their dedication to students' success, brilliant ideas, and scientific rigor have been a constant source of inspiration. Their insightful feedback and commitment to my educational growth have been invaluable in shaping my research and professional development. Their ability to encourage critical thinking, foster a collaborative environment, and nurture a passion for discovery has been instrumental in my achievements. I am grateful for the opportunity to have learned from and worked with such a capable mentor.

I would also like to thank my supervising and reading committee for their instrumental role in my academic journey. Thank you to Professor Boris Blinov, a key member of my supervising and reading committee, who has been a part of my PhD journey since the beginning; from leading the way during my first steps into quantum information science, to finally approving this dissertation. I am also grateful to Max Parsons, who came into my supervising and reading committee within a moment's notice. His feedback helped take this dissertation over the finish line. A special thank you to Mark Rudner, both a member of my supervising committee and a great physics lecturer that taught me a lot. Anna Goussiou, another member of my supervising committee, who has been a source of constant support, especially during my first year in the program, providing me with a much-needed connection to home. I also want to thank Brandi Cossairt and Emily Levesque who served as my GSR during my general and final exams, respectively, for the time they invested and the expertise they provided in this journey.

Outside of my committee, I am also grateful to all the UW professors that helped me suc-

ceed in this program. A thank you to Lukasz Fidkowski, Andreas Karsch, Anton Andreev, Ann Nelson, and Leslie Rosenberg for their immense effort in providing the 2018 first-year graduate students with all the necessary tools to succeed as physicists. I am also thankful to Nathan Wiebe and Subhadeep Gupta for furthering my understanding of quantum information science during my second year in the program. I would also like to thank Jason Detwiler, my first-year graduate student advisor, for his welcoming nature and enthusiastic support. A thank you to Peter Shaffer whose guidance during the first year tutorial classes has made me a better teacher. Lastly, I would like to thank Marcel den Nijs for making sure I kept moving forward with my degree.

I would also like to extend my gratitude to the invisible wheel that keeps the department running: the stuff. Catherine Provost has always been supportive with words and chocolate. Huimei Wu always made sure that everything our lab needed was promptly purchased and taught me a great deal about how procurement works in such a large scale. A thanks to Andrew Sattler, Sandy Chudler, and Mike Kummer for all their administrative support that made our research endeavors smoother. Thank you to Alexis M. Hall, Kayla Troske, and all of the front desk stuff that was helpful for receiving and sending packages, checking out keys, and making sure all the department events and operations run smoothly. I would also like to thank Jason Alferness for heroically managing the building and making sure our cryostat was always up and running. Lastly, I would like to thank the machine shop stuff for their time and guidance; their lessons allowed me to create my own machined equipment that was instrumental to my experiments.

Beside the UW educators, I would have not been here without the support and encouragement of those who came before them. Starting backwards in time, I would like to thank my undergraduate (and unfinished master's) supervisor at AUth, Professor Spyridon E. Tzamarias, for being an exceptional teacher and a great mentor that introduced me to the world of particle physics. His deep understanding of fundamental physics and thirst for knowledge

were inspiring. I would like to thank the rest of the community of nuclear and particle physics professors at AUTh, specifically, Charikleia Petridou, Christos Eleutheriadis, Konstadinos Kordas, Dimitrios Sampsonidis, Alexandra Ioannidou, and Stylianos Stoulos who created a welcoming environment, supported me and believed in my academic endeavors. A thank you to the professors that taught me a lot I didn't know I needed until I got into an experimental optics lab in grad school: Ioannis Arvanitidis, Maria Katsikini, and Konstadinos Vyrsokinos. I would also like to express my gratitude to some more AUTh professors who shaped my early academic path: Loukas Vlahos, Charalambos Moustakidis, and Georgios Vouyatzis. Lastly, I would like to express my profound gratitude for my high-school physics mentor, Argyro Gida, who first recognised my aptitude for physics and science, always believed in me and encouraged me, and inspired me to be the scientist I am today.

This journey would have not been possible without the guidance, support, and camaraderie of my lab mates. Joining the lab, Xiayu Linpeng and Maria L. K. Viitaniemi, the ZnO donor qubit trailblazers, have been exceptional mentors. Xiayu taught me everything one needs to know to survive in an experimental optics lab, and his work ethic was truly inspirational. Maria has always been the wise person I turn to for advice, helping me navigate grad school both professionally and personally. Her influence has been consequential to making this achievement possible. During the pandemic, I worked and learned side-by-side with an incredible postdoc, Chris Zimmermann. I am grateful to him for always being patient with me, looking out for me, and prioritizing my scientific and professional growth in our common scientific explorations. Xingyi Wang and Ethan Hansen, the future of our ZnO team, have been an absolute pleasure to work with. Xingyi, even though we did not work closely together, has been an example of methodical experimentation and thorough research, steadily pushing our understanding of this platform forward by the day. She's also an incredible baker, whose treats-to-share were a very much needed support throughout this journey. Ethan and I have shed blood, sweat, and tears over the course of the last two

years working over an optical table and taming the beast (our beloved cryostat). Together, we learned to be patient, take a step back, and plan ahead. With his direct attitude and deep understanding of himself, guiding Ethan has taught me how to be a better mentor. The moment it was time to part ways to our solo projects, was when I truly understood the value of teamwork and how much I will miss all these incredible colleagues. Another person I worked with for a long time was Samuel D'Ambrosia, a philosopher- and physicist-in-training overflown with scientific curiosity and inquisitive instincts, helped me gain a clearer theoretical understanding of the underlying mechanisms behind the ZnO platform. Luc Street was another undergraduate I co-advised my first summer in the lab whose code has been the backbone of most of the experimental implementations in this dissertation, and the spark to my growing interest for hardware integration software. Roman Kolodka, the most recent addition to the ZnO team, has given me plenty of pleasant escapes with our – sometimes too long – evening chats about our research and the world, and brought something in the lab that felt closer to home.

Outside the ZnO team, our lab has been ans is filled with wonderful people. Alan Logan and Srivatsa Chakravarthi, even though they worked on separate projects, they were always willing to help and teach. I owe my first steps into photonics and fabrication to them. Zeeshawn Kazi, a tremendous mentor whose cheerful spirit and calm demeanor always brought the lab together and inspired confidence that all will be okay. I will always be grateful for his guidance and support through our shared journey of grief over a parent's loss. Christian Pederson is someone that I always admired and looked up to for his deep understanding of everything he is interested in, his exciting new ideas that lead him to new truths, as well as his eagerness to teach and willingness to help. Thank you for being such a good friend and colleague. I would also like to thank Nick Yama and Tommy Nguyen, two amazing teammates and researchers who have made this journey more bearable with their company, support and everything they taught me. Lastly, I would like to thank Carson

Patterson, Ethan Williams, Adam Cox, Asher Han and everyone else who has been part of the lab, making it the friendly, supporting and welcoming place that it was, is and hopefully continue to be.

I would also like to thank our collaborators for lending their expertise to advance our understanding of the ZnO donor qubit. Thank you to Professors Masashi Kawasaki and Yosuke Kozuka and for providing us with pristine ZnO substrates on our research early on. I am also grateful to Professor Mikhail Durnev for his contributions to the understanding of the spin relaxation mechanism. I am appreciative of Edward Bielejec and Michael Titze for the In implantation in our first exploration of In donors as qubits. Thanks to Bethany Matthews and Steven Spurgeon, the isolation of single emitters in ZnO was made possible. I would also like to thank Professor Joe Falson for the provision of ZnO substrates and fabrication advice for the Stark tuning project, and Professor Lasse Vines for the continuous characterization of our ZnO substrates, as well as his fabrication advice and implantation of In donors for the Stark tuning project.

Speaking of fabrication advice, the Stark tuning project would have not been possible without the extensive UW fabrication facilities and people that support them. First, I would like to thank the Washington Nanofabrication Facility stuff for providing excellent support and an efficient workspace. Darick Baker has been an incredible person to learn from, and his PhD experience on ZnO was an important steppingstone for developing a fabrication process. Thanks to Fred Newman's flexibility and expertise, I learned about atomic layer deposition in no time, a much needed last-minute addition to my fabrication process. I would also like to thank Professors David Cobden, Xiaodong Xu, and Matthew Yankowitz and their students for fostering a unique collaborative environment and sharing of equipment between the condensed matter physics labs. A special thanks goes to Eric Lester, a fellow PhD student, for the immense amount of time and effort he has put not only in training me in multiple pieces of equipment, but also actively being interested in the Stark tuning project

and eager to troubleshoot with me whenever I found a roadblock. I would also like to thank Paul Nguyen whose serene approach to equipment trouble always made me feel better when I made mistakes. Lastly, a thank you to Joon Park for his thorough training on the SEM and E-beam lithography.

Of course, life was made easier with daily interactions with fellow basement denizens and my cohort. Our collaboration with Professor Blinov's group brought me close to many of his students. I am grateful to Alex Kato, an amazing colleague and friend whom I always admired for his work life balance and work ethic. His encouragement and compassion offered much needed breaks. A thanks to Carl Thomas, Jane Gunnell, and Aaron Hoytt for our basement corridor run-in discussions and continuous scientific collaboration that made working in the basement a little bit more fun. I would also to thank Tahiyat Rahman, my first-year office-mate with a tenacious spirit for fighting for his fellow students, for his camaraderie and support. Lastly, I would like to acknowledge my fellow cohort-mates Pyxie Star (another other office-mate) and Dara Storer for making this journey more enjoyable.

Coming to Seattle for grad school came with lots of ups and downs, and certainly lots of friends that made Seattle feel like home. Through the Physics program, I met many people who I consider close friends to this day: Dean Huang, Arnab Manna, Wan Jin Yeo, and Dani Koch. Our journey together has spanned from working on homework problems on year one, to spending endless hours together inside and outside the program. Some of my favorite times include our gatherings to new restaurants, playing board games, grabbing boba and drinks, and our potluck dinners and parties. This is the end of an era, and I am lucky to have shared this journey with y'all. Making friends outside the physics department was a necessary escape from reality. First and foremost, I found that in William Atienza, a randomly assigned apartment-mate at UW housing, who quickly became a close friend. His bright and exuberant personality alongside the countless hours of chats, cooking, and exploring the city were a much needed escape. Adhithi Rajan has been another close friend,

and even though our overlap in Seattle was short, I always enjoyed her company and wisdom whenever possible. Lastly, I would like to thank Corina Pierce and Ruhee Nirodi for their continuous support and friendship.

I would also like to thank my friends and community from back home, who have been in my life for a very long time and who I miss dearly. Thank you to Costas Balaskas, and Nikos Avramidis whose frequent calls and visits to Seattle have kept me connected to my roots and provided much-needed support and laughter. I would also like to thank Vaggelis Baslis, Thanasis Michailoudis, Giorgos Bardanikas, Vaggelis Kilipiris, and Costas Keramaris for their texts, calls, and for showing up during all of my personal and academic transitions. As for Katerina Tsiligiri, Ioanna Aslani, Vaggelis Koukolis, Alina Matrapazi, Giannis Abrazis, Nelli Laleni and Xenia Kaberi, I am thankful for all the memories and experiences we shared.

I want to express my deepest gratitude to my family, whose unwavering support has been the bedrock of my academic journey. Thank you to my mom and dad, Christina and Panos, for their unconditional love, nurturing spirit and resilience. Thank you for always pushing me to be my best self and providing me with everything I needed to succeed. I would also like to thank my sister, Anna, for always being on my side and making me laugh even during the most stressful times. Thank you to my grandparents, for inspiring me and keeping me grounded.

Finally, I would like to thank the person who has been the cornerstone of my resilience throughout this journey: my partner, Amy. Thank you for your constant support, patience love, and sacrifices, for all the little moments we have shared, for making me celebrate every little milestone and for reminding me of life outside the lab. Your guffiness, creativity, and witts keep me on my toes and inspire me every.

This dissertation would not have been possible without the support and contributions of all these incredible individuals. Thank you all.

DEDICATION

Στον πατέρα μου, που δε θα δει το τέλος αυτού του ταξιδιού, ούτε την αρχή του επόμενου,
για την αθάνατη αγάπη και σοφία του, που με καθοδηγούν μέχρι και σήμερα.
Στη μητέρα μου, για τις ανιδιοτελείς θυσίες της, την αδιάλειπτη στήριξη και την πίστη της,
χωρίς την οποία δεν θα ήμουν σήμερα εδώ που είμαι.

To my father, who will not see the end of this journey nor the beginning of the next, for his undying love and wisdom that still guide me to this day.
To my mother, for her selfless sacrifices, unwavering support and faith, without whom I would not be where I am today.

Chapter 1

INTRODUCTION

In the past few decades, there has been a growing effort to advance the field of quantum information science (QIS) and develop revolutionary technologies based on the principles of quantum mechanics. Prominent areas of QIS research include quantum computation [1–4] and communication [5–9] networks, quantum sensing [10, 11] and quantum metrology [12–14]. These fields hold the promise of transforming various aspects of technology and science; with quantum computers solving certain types of problems faster than classical computers [15–18], communication and encryption becoming more secure [6], and measurements of physical phenomena becoming more sensitive than classically possible [11, 12]. Recently, QIS has gained significant momentum and visibility, driven by milestones toward the development of commercially viable quantum computing hardware, such as Google's controversial proof-of-concept demonstration of computational quantum advantage [19, 20]. In parallel to the development of quantum computing systems is the development of quantum communication networks with the ambitious goal of a quantum internet [21]. The envisioned quantum internet would be a vast quantum network (QN) that enables or enhances a range of QIS applications [21, 22], including fundamentally secure communication [23] , distributed quantum computing [24] and quantum sensing [25], navigation, timing, and clock synchronization [26].

The overarching concept of QIS is the use of the elementary unit of quantum information, the quantum bit or qubit [27], a quantum system consisting of two energy levels or states. The term 'qubit' encompasses a diversity of physical implementations with different properties that are derived from the nature of the physical two-level system and its interactions with the environment. Ideally, the qubit interacts with the environment only during state

manipulations and measurements. However, realistic physical implementations of qubits are subject to unintentional, state-altering interactions with their environment, resulting in loss of information, or decoherence [3, 28]. Mapping these interactions is challenging, and mitigating their effects poses even greater difficulty, creating unique challenges for the operational performance, reliability, and scalability of QIS applications [29]. However, it is not all dire. These same interactions can be used as an advantage, e.g., to 'sense' the environment [25, 26], alter the inherit qubit properties [30], or interact with other qubits [31–34]. Consequently, different QIS applications may require and/or benefit from use of different qubit platforms.

The search for qubit platforms that sufficiently satisfy the established criteria for quantum computing and communication networks [28] is an ongoing effort. Key criteria for quantum computation include the ability to perform operations much faster than it takes for the qubit to decohere (gate time versus coherence time), the ability to accurately initialize, operate on, and measure the qubit state, and the ability to scale up to large multi-qubit platforms [28]. For quantum communication, we additionally need to convert stationary qubits to flying qubits (e.g. photons) and faithfully transmit them between locations [28]. Many different types of qubits are being investigated for quantum computing applications, including all-photonic platforms, trapped atoms and ions, solid-state color centers, gate-defined and epitaxial quantum dots, and superconducting circuits. Some of these quantum computing qubit candidates can more efficiently couple to photons, making them directly suitable for quantum communication applications as well. All physical implementations come with their own strengths, challenges, and constraints. For example, all-photonic platforms can operate at ambient conditions and can have high operation speed, but they are hard to scale up because of the probabilistic nature of the gates [35]. Trapped atoms and ions boast long coherence times reaching seconds or even hours, can be operated with high fidelity, can be efficiently coupled to photons and can operate at high cryogenic temperature environments, but demonstrated gate times are in the order of 100 ns - 100 µs which inhibits operation speeds [29, 36, 37]. However, they need to operate in ultra high vacuum, suffer from low photoluminescence collection efficiency and rely on tabletop setups for optical control which

poses a significant scaling challenge [29, 37]. Scale-up efforts, e.g. via photonic device integration in on-chip planar traps [38], come with their own set of challenges, including the need to achieve high fabrication precision of increasingly complex electronic and photonic circuits, and need to mitigate optical losses, cross-talk and increased heating [29, 37]. Superconducting qubits have short gate times (10 ns - 1 µs) and superconducting circuit fabrication technology is more advanced. However, they exhibit short coherence times (up to 1 ms), and operate at very low cryogenic temperatures (0.1 K) [29, 39]. Lastly, color centers and quantum dots includes a vast array of quantum systems, each one with different properties, from spin defects in silicon that have great spin properties [40–43], but are challenged by the indirect band gap making for (usually) poor optical efficiency [44, 45], to quantum dots in III-V semiconductors with excellent optical properties but short coherence times due to host lattice nuclear spin baths [46–50]. There is not a clear winner in the quantum network qubit race, and new qubit discovery is an active area of research.

An emerging platform for quantum communication applications is the shallow donor in ZnO. As a material host, ZnO boasts advantages from both group IV and III-V semiconductors. Similar to silicon and diamond, both Zn and O can have stable nuclear spin-free isotopes, which allow for long coherence times. ZnO is a direct band gap material, usually related to favorable optical efficiency, similar to III-V semiconductors such as InP and GaAs. ZnO is also radiation-hard [51] and compatible with excising micro-fabrication processing [52], which are beneficial for defect introduction via ion implantation and device fabrication with focused ion beam milling. Shallow donors in ZnO are of particular interest because they are effective mass point defects, relatively easy to physically create and theoretically model, with an optical coupling to the donor-bound exciton with 90 % efficiency in the zero-phonon line [53]. Recent findings [54] indicate that gallium electron spin ensembles in natural-abundance ZnO yield 100 ms longitudinal spin relaxation T_1 times, and 50 µs spin echo coherence T_2 times via all optical measurements. This result is promising, as the observed times may not represent an inherent limit of the system, but rather a need for higher host purity. The T_1 measurement was constrained by the ensemble spin initialization

at low magnetic fields where the $D^0 \leftrightarrow D^0X$ linewidth is comparable to the Zeeman splitting. Also, T_2 is limited by instantaneous diffusion or the ^{67}Zn nuclear spin diffusion. In addition, gallium and other group III isotopes possess nuclear spin which may exhibit longer coherence times compared to the electron spin due to its weaker coupling to the environment [55]. These nuclear spins can be used as long-lived quantum memories, similar to phosphorus shallow donors in silicon [56]. The shallow donor in ZnO is therefore promising both for photon-based quantum processing and optical quantum memory applications, where information can be transmitted via the donor-bound exciton transition and stored in the electron or nuclear spin. As described in the next section, a quantum platform must meet several criteria before being utilized in such applications. In this dissertation, we take the first steps toward this goal by extending our understanding of the underlying properties of this quantum system and its interactions with the environment; we measure the spin relaxation time and optical linewidth of emitter ensembles, isolate single emitters with favorable optical properties, and report progress on optical frequency tuning.

1.1 Photon-based quantum networks

1.1.1 Realizing a two-node measurement-based quantum network

A quantum network is a collection of quantum nodes and quantum channels (Fig. 1.1a). The quantum node is where information is stored and processed and is comprised by one or more qubits. The quantum channel is the interconnection between nodes which is achieved via quantum entanglement. One way to create a quantum network using photon-emitting defects is to entangle the qubit of each node with the emitted photon and then use a measurement-based protocol where photons interfere on a beam splitter to erase which-path information (Fig. 1.1b). Upon photon measurement, the node qubits are projected into an entangled state. A stationary qubit $|\psi\rangle$ in a pure state can be described by a wavefunction that is a linear combination of the two computational states $|0\rangle$ and $|1\rangle$

$$|\psi\rangle = \alpha\,|0\rangle + \beta\,|1\rangle\,, \tag{1.1}$$

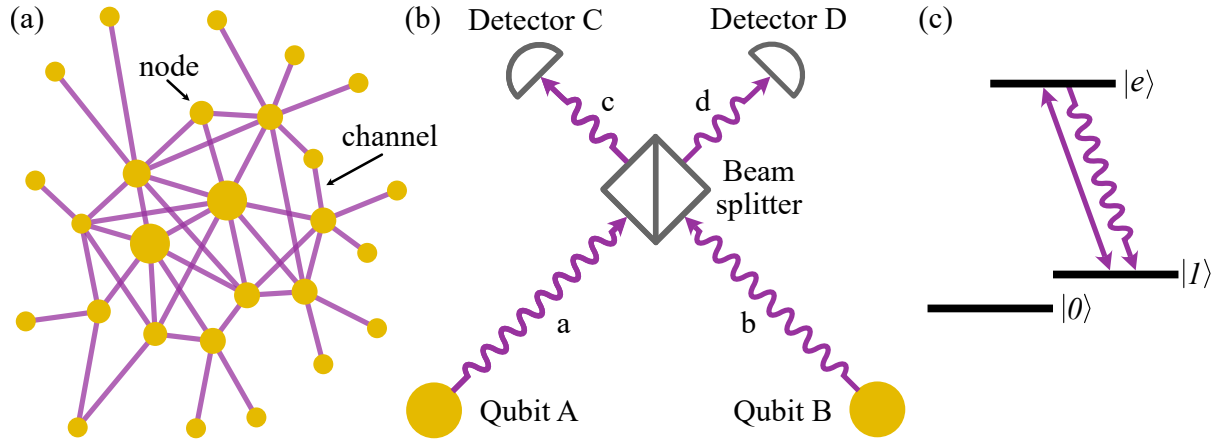

Figure 1.1: (a) Schematic depiction of quantum network with quantum nodes, depicted as spheres, interconnected via quantum channels, depicted as lines. (b) A schematic of the measurement-based entanglement protocol. (c) The energy level diagram for the qubits used in the aforementioned protocol.

where α and β are complex coefficients and correspond to the amplitude of each state with $|\alpha|^2 + |\beta|^2 = 1$.

For this simple quantum network demonstration we utilize two qubits A and B with corresponding states $|\psi\rangle_A$ and $|\psi\rangle_B$. Both qubits have optical access to an excited state $|e\rangle$ via the $|1\rangle$ state (Fig. 1.1c). The excited state is not occupied unless the qubit is driven by an external excitation field, in which case it relaxes back to the $|1\rangle$ state with a lifetime of τ with the emission of a photon in mode (in this case, path) x. The emitted photon can be described as an excitation to the photonic vacuum state $|\text{vac}\rangle$ as $a_x^\dagger |\text{vac}\rangle$, where $a_x^\dagger$ is the raising operator of mode x. Therefore, this two qubit system with optical access can be described by the tensor-product of three states: spin A, spin B, and photonic state as

$$|\Psi\rangle = |\psi\rangle_A \otimes |\psi\rangle_B \otimes |\text{photon}\rangle\,. \tag{1.2}$$

When a photon interacts with a 50-50 beam splitter, the photon path is split in two, a transmitted t and a reflected r path. In this example, we use a beam-splitter that introduces a symmetric phase-shift to the outgoing reflected beams, meaning that the reflected photon

receives a 45° phase shift in each incident direction, yielding a transfer matrix of

$$M = \frac{1}{\sqrt{2}} \begin{pmatrix} 1 & i \\ i & 1 \end{pmatrix}. \tag{1.3}$$

Therefore, the resulting transformation can be described as $a_x^\dagger \rightarrow \frac{1}{\sqrt{2}} \left(a_t^\dagger + i a_r^\dagger \right)$.

Here, we follow the protocol described in Ref. [44] to entangle the two stationary qubits that are optically accessible.

- Initializing each qubits in the $|+\rangle = \frac{1}{\sqrt{2}} \left(|0\rangle + |1\rangle \right)$ state, the system wavefunction is

$$|\Psi\rangle_i = \frac{1}{\sqrt{2}} \left(|0\rangle_A + |1\rangle_A \right) \otimes \frac{1}{\sqrt{2}} \left(|0\rangle_B + |1\rangle_B \right) \otimes |\text{vac}\rangle , \tag{1.4}$$

- After successful initialization, we resonantly drive the optical transition from the $|1\rangle$ state to the $|e\rangle$ state for both qubits. The resulting system wavefunction is

$$|\Psi\rangle_1 = \frac{1}{\sqrt{2}} \left(|0\rangle_A + |e\rangle_A \right) \otimes \frac{1}{\sqrt{2}} \left(|0\rangle_B + |e\rangle_B \right) \otimes |\text{vac}\rangle . \tag{1.5}$$

- Within the time-range of the optical transition lifetime, both qubits will relax back to the $|1\rangle$ state while emitting a photon in two different paths, a and b, coupling the $|1\rangle$ states to their corresponding photons

$$|\Psi\rangle_2 = \frac{1}{\sqrt{2}} \left(|0\rangle_A + |1\rangle_A \, a_a^\dagger \right) \otimes \frac{1}{\sqrt{2}} \left(|0\rangle_B + |1\rangle_B \, a_b^\dagger \right) \otimes |\text{vac}\rangle . \tag{1.6}$$

- Using a 50-50 beam splitter, the photons from paths a and b will interfere with the corresponding transformations $a_a^\dagger \rightarrow \frac{1}{\sqrt{2}} \left(a_d^\dagger + i a_c^\dagger \right)$ and $a_b^\dagger \rightarrow \frac{1}{\sqrt{2}} \left(a_c^\dagger + i a_d^\dagger \right)$. Rearranging the various terms to group by different photon paths, the system wavefunction becomes

$$\begin{aligned} |\Psi\rangle_3 = \frac{1}{2} \Big[& |0\rangle_A \otimes |0\rangle_B + \\ & \frac{|0\rangle_A \otimes |1\rangle_B + i \, |1\rangle_A \otimes |0\rangle_B}{\sqrt{2}} a_c^\dagger + \\ & \frac{i \, |0\rangle_A \otimes |1\rangle_B + |1\rangle_A \otimes |0\rangle_B}{\sqrt{2}} a_d^\dagger + \\ & \frac{i}{2} |1\rangle_A \otimes |1\rangle_B \left(a_d^\dagger a_d^\dagger + a_c^\dagger a_c^\dagger \right) \Big] \otimes |\text{vac}\rangle . \end{aligned} \tag{1.7}$$

- In this form, we notice that the detection of a single photon in path c or d will collapse the wavefunction in a different entangled state of spins. For example, the detection of a single photon in path c results in the final state

$$|\Psi\rangle_f = \frac{1}{\sqrt{2}} \left(|0\rangle_A \otimes |1\rangle_B + i\, |1\rangle_A \otimes |0\rangle_B \right) \tag{1.8}$$

This simple demonstration of a two-node quantum network outlines the requirements of stationary-to-flying qubit quantum networks, most of which have been extensively discussed by Ref. [28] and briefly discussed in the previous section. To realize a complex quantum network with multiple qubits, each qubit must be individually addressable, otherwise entanglement generation between specific qubits is impossible. As we saw, successful qubit initialization is paramount to creating a specific entangled state. Since the protocol is dependent on the reliable emission of a photon after optical excitation, there needs to be efficient coupling between the stationary qubit and the flying qubit. Additionally, photon entanglement necessitates that the photons are identical, both in the frequency and time domains, otherwise the ability to distinguish between photon sources will result in reduced entanglement fidelity. While in this protocol we talk about optically active qubits, any qubit that has access to a flying qubit interface (e.g., superconducting qubits coupled to a microwave-to-optical transducer [57]) can utilize this scheme. Moreover, realization of the entanglement is dependent on the successful measurement of single photons. Finally, in order to perform any quantum operations, the entangled state will need to persist without significant decoherence within the timescales relevant to the realization of the entanglement and any subsequent operations on the qubits. Even in a perfect system this process is probabilistic. Thus, scaling to large networks with single qubit nodes is challenging. Deterministic scaling becomes possible with a local quantum memory at each node. Throughout this thesis, we investigate donor spin qubits in ZnO while reflecting on these requirements.

1.1.2 Optical quantum memories

In photon-based quantum computation, storing information is crucial for synchronizing quantum operations between distant nodes [58]. A key aspect of realizing long-distance quantum networks is the faithful transmittance of photons. However, current communication channels (optical fibers, atmosphere) lose information exponentially with transmission distance due to absorption, making practical quantum networks unfeasible. Quantum repeaters can mitigate this by enabling polynomial loss over distance [58, 59]. These repeaters need to enable entanglement between the receiving and outgoing flying qubits in a synchronous manner, achievable via an optical quantum memory. Thus, both quantum computation and communication networks benefit from storing optical quantum information.

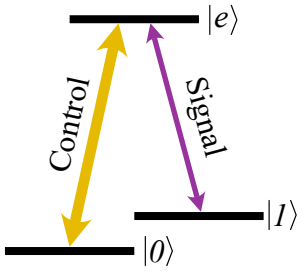

Figure 1.2: The energy level diagram of a three-level system with two driving fields (control and signal) interfering on the $|e\rangle$ state.

There have been many proposals exploring different methods of realizing optical quantum memories [22, 58]. One class of quantum memories that has been proposed and experimentally demonstrated to varying levels of success uses ensembles of optically active qubits to temporarily store an optical pulse in the ensemble [22, 58–60]. These ensemble optical quantum memory protocols are based on electromagnetically induced transparency (EIT) [58–60]. EIT is a quantum interference effect observed in 3-state quantum systems in the presence of two driving fields (Fig. 1.2). Assume an ensemble of quantum systems whose two qubit states $|0\rangle$ and $|1\rangle$ are both optically coupled to an excited state $|e\rangle$. Each driving field, called control and signal is set near each of the $|1\rangle \leftrightarrow |e\rangle$ and $|0\rangle \leftrightarrow |e\rangle$ transition resonances. In

the presence of only the control field, all N qubits in the ensemble will be initialized to the $|1\rangle$ state

$$|\Psi\rangle_{\text{init}} = \bigotimes_{i=1}^{N} |0\rangle_i = |0_1...0_N\rangle \,. \tag{1.9}$$

The two fields destructively interfere with each other, resulting in a superposition state just between the $|0\rangle$ and $|1\rangle$ states of the atomic ensemble. If the signal beam is a single photon, then only a single qubit state will be transferred in the $|0\rangle$, but it is not known which one. The resulting state is

$$|\Psi\rangle_1 = \frac{1}{\sqrt{N}} \sum_{i=1}^{N} \left[\left(\bigotimes_{j \neq i} |0\rangle_j \right) \otimes |1\rangle_i \right] = \frac{1}{\sqrt{N}} \sum_{i}^{N} |0_1...1_i...0_N\rangle \,. \tag{1.10}$$

By turning off the control field adiabatically after the signal is absorbed, the ensemble will stay in this superposition state. The signal pulse can be retrieved by turning back on the control field. Put simply, the single photon signal has been stored in the qubit ensemble and was later retrieved on demand due to a transparency window created by the control field.

This simple protocol outlines the requirements for successful storage and retrieval of information. Firstly, the optical pulse must be fully contained physically in the host medium at the time of storage, and spectrally within the transparency window, which require the contrast of the window – or optical depth of the transition – to be as high as possible [58, 61]. Secondly, the amount of time the information can be stored for is related to the coherence time of the qubit ensemble. Therefore, long storage times require long coherence times. These two requirements are the key characteristics physical systems must satisfy for successful realization of EIT-based optical quantum memories. The most prominent platforms have been atomic ensembles and rare earth doped crystals [62]. Atomic ensembles boast high optical depths, efficient signal retrieval, and storage times up to seconds, while REIs yield storage times in the order of hours, but have limited optical depth [62]. In Chapter 5, we will see how donor ensembles in ZnO could compare with these leading systems.

1.2 Overview

In Chapter 2, we review the properties of neutral shallow donors in ZnO. We discuss how donor impurities such as aluminum, gallium, and indium, can be introduced either during growth or through ion implantation and explore their optical properties in the context of photon-based quantum network applications, where the donor-electron spin-1/2 states in the presence of magnetic field can be the physical qubit implementation.

In Chapter 3, we describe the experimental setup and techniques. We provide a list of key donor properties and explain how each measurement scheme is used to extract them. Common measurement schemes throughout this thesis include photoluminescence, optical pumping, spin relaxation, steady-state resonant photoluminescence excitation with one or two lasers, as well as time-resolved photoluminescence excitation measurements.

In Chapter 4, we focus on the experimental and theoretical study of the longitudinal spin relaxation time (T_1) of *in situ* Ga donor ensembles, a property that determines the maximum possible coherence time of a qubit. We perform T_1 measurements as a function of applied magnetic field, temperature and excitation photon energy. We measure T_1 nearing 0.5 s, at 1.75 T and 1.5 K, with potential for longer values at smaller magnetic fields. Additionally, we find excellent agreement between the experimental data and a theoretical model based on the spin-orbit (admixture mechanism) and electron-phonon (piezoelectric) couplings for ZnO's wurtzite crystal symmetry. This work highlights the potentially advantageous spin properties of the ZnO-base qubit platform.

In Chapter 5, we study optical parameters of *in situ* Al, Ga, and In as well as implanted In donor ensembles essential to quantum network applications – namely the optical linewidth and optical depth. Via photoluminescence excitation spectroscopy, we find that the zero-field linewidths are not thermally broadened at temperatures below 5 K. The extracted 0 K linewidth limit is $7 - 11$ GHz, less than two orders of magnitude larger than the $\mathcal{O}(0.1\,\text{GHz})$ Fourier lifetime-limit. Transmission spectroscopy reveals a nearly identical inhomogeneously broadened linewidth for donor ensembles throughout the entire 0.3 µm-thick crystal. We also

observe a large optical depth of $20 - 300$, a beneficial property for optical quantum memory applications. Utilizing transient spectral hole-burning spectroscopy, we observe a marginally narrower homogeneous linewidth of 4 GHz. While the source of the moderate inhomogeneous broadening is identified as the isotope mass variation between different hyper-local donor environments, the source of the large homogeneous broadening of donor ensembles remains elusive. Nevertheless, the surprisingly narrow optical linewidths and large optical depth of donor ensembles of unintentional dopants in natural abundance ZnO emphasize the favorable optical properties of this system.

While ensemble properties are an important metric of qubit fitness, most quantum network applications require access to individual qubits. Our previous studies focused on unintentionally doped samples with concentrations far exceeding single-defect levels within our probing depth, due to the difficulties in producing high purity ZnO. Chapter 6 shows how we overcome this challenge, by using a focused ion beam to mill a thin slice out of bulk ZnO. Using spatial and frequency filtering, we demonstrate isolation of stable single emitters which are identified as In donors based on their emission frequency and magnetic field spectroscopy signature. This work underlines the qubit's properties' resilience against irradiation and indicates a path toward device integration.

The isolated emitters experience substantial inhomogeneous broadening attributed to the strained environment of the thin ZnO slice. In Chapter 7 we report our progress toward frequency tuning implanted In ensembles by applying a strong electric field parallel to the sample surface. The electric field is generated by applying a voltage differential on planar capacitors fabricated on the ZnO surface. In the first generation of devices, featuring a 10 nm SiO_2 layer and chromium-gold contacts, we observe a small frequency shift – much smaller than predicted – and significant linewidth broadening as a function of applied voltage. Our results indicate that this shift is not due to an electric field, but due to a local change in the temperature of the substrate caused by high current flow. Nevertheless, this is an important step towards the realization of frequency tuning of shallow donors in ZnO.

Finally, Chapter 8 summarizes the key experimental results and outlines the future

prospects for shallow donors in ZnO as qubits. It rehashes our findings on spin properties, optical characteristics, and single donor isolation, highlighting both the promising aspects and the challenges of this platform for quantum network applications. The chapter identifies critical areas for future research, including material purification, photonic integration, and qubit control techniques. By addressing these challenges, we anticipate significant advancements in ZnO-based shallow donor spin qubits, potentially enabling entanglement between single qubits and opening avenues for heterogeneous quantum networks.

Chapter 2

THE NEUTRAL SHALLOW DONOR IN ZINC OXIDE

2.1 Zinc Oxide

2.1.1 Crystal structure

Zinc oxide (ZnO) is a direct band gap semiconductor. It is typically called a II-VI or 12-16 semiconductor due to the columns zinc (Zn) and oxygen (O) occupy in the periodic table, using the old, and modern assignments, respectively. Crystalline ZnO is usually found in a hexagonal wurtzite structure, the most stable structure under ambient conditions. However, cubic zincblend and rocksalt structures are also observed when grown on cubic substrates or under very high pressures, respectively [63]. Here, we will focus on hexagonal wurtzite ZnO crystals. This structure, is characterized by three dimensions, $a \simeq 3.25\,\text{Å}$ and $c \simeq 5.2\,\text{Å}$ and $u \simeq 0.383$ [63], labeled in Fig. 2.1a. It also exhibits an intrinsic polarity between Zn and O, leading to two polar faces: (0001) and $(000\bar{1})$, the Zn-face and O-face, where the $\langle 0001 \rangle$ direction is parallel to the crystal $\hat{c}$ axis.

2.1.2 Crystal growth

Ultra-high-quality single crystal ZnO substrates are still elusive, despite the plethora of growth methods that are being simultaneously researched, including melt growth, seeded chemical vapor transport and hydrothermal (solvothermal with aqueous solvent) growth [65, 66]. Among these bulk crystal growth methods, hydrothermal growth yields the best results in terms of structural quality and chemical purity [65, 66]. The common growth direction is along the $\hat{c}$ axis, and the resulting crystal is called a c-plane or [0001] crystal. After growth, these crystals need to be subsequently processed: the surface needs to be

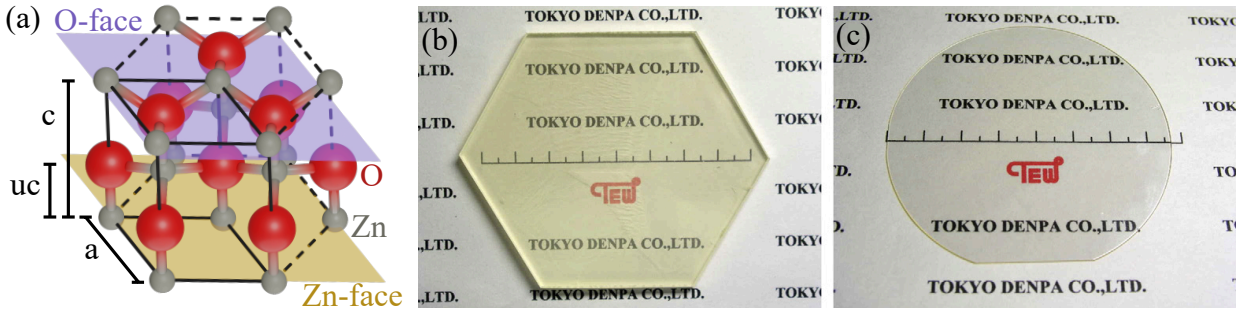

Figure 2.1: (a) ZnO wurtzite structure. Oxygen atoms are depicted with red spheres, while zinc atoms are depicted with smaller gray spheres. The two polar surfaces are depicted as semi-transparent planes (purple (top) for oxygen, yellow (bottom) for zinc). (b) and (c) Images of a 3-inch c-plane ZnO crystal without and with a CMP finish. Scale bar is 80 mm. The images in (b) and (c) are reprinted from [64], with permission from Elsevier.

chemically-mechanically polished (CMP) [67] to a roughness of $\mathcal{O}(1\,\text{Å})$, and high concentrations of lithium (Li) must be removed [64, 66, 68] via annealing in an O_2 atmosphere at 1100 °C [69, 70]. Even after careful preparation and processing, TD substrates still exhibit high concentrations of *in situ* impurities – introduced unintentionally during growth either from the seed substrate, the growth process or contamination of the growth chamber – with concentrations of different contaminants ranging between 10^{14} atoms/cm^3 and 10^{17} atoms/cm^3 [64, 67]. However, higher quality (lower contaminant concentration) ZnO layers can be produced via molecular-beam epitaxy (MBE) [67, 71].

Atomic isotope	^{64}Zn	^{66}Zn	^{67}Zn	^{68}Zn	^{70}Zn	^{16}O	^{17}O	^{18}O
Abundance (%)	49.178	27.740	4.042	18.456	0.611	99.757	0.038	0.205
Spin	0	0	5/2	0	0	0	5/2	0

Table 2.1: Relative isotopic abundance in nature, and nuclear spins of stable zinc and oxygen isotopes [72].

In this dissertation, we study hydrothermally grown c-plane ZnO substrates by Tokyo Denpa Co. Ltd. (TD) [64, 69] (Fig. 2.1b and Fig. 2.1c). In some cases, we study TD

substrates with an MBE layer on the Zn-face. Neither the substrates nor the MBE layers used for this work are isotopically purified; they contain both Zn and O in their natural isotopic abundance (Tab. 2.1).

2.1.3 Band gap structure

ZnO, similar to other II-VI semiconductors, exhibits a wide band gap of 3.437 eV [77] at 0 K and 3.355 eV at room temperature [78–80]. The valance band is split into three bands (A, B, and C from higher to lower energy) due to the crystal field and spin-orbit interactions [74]. A unique characteristic of ZnO is that it boasts a negative and small spin-orbit coupling [74]. Due to the relative anisotropy in the hexagonal wurtzite structure, ZnO properties are different between the longitudinal (parallel to the $\hat{c}$ axis) and transversal (perpendicular to the $\hat{c}$ axis) directions of the crystal lattice. However, the effective electron/hole masses and dielectric constants between the two directions do not substantially differ from each other [73–76] (Table 2.2). This will allow for modeling simplifications later on (App. A.1).

Constant	Value	Reference	Notes
$m_e^{*,\parallel}$	$0.28\,m_e$	[73]	
$m_e^{*,\perp}$	$0.24\,m_e$	[73]	
m_e^*	$0.252\,m_e$	[74]	$3/m_e^* = 1/m_e^{*,\parallel} + 2/m_e^{*,\perp}$
m_h^*	$0.59\,m_e$	[75]	$m_{A,h}^{*,\parallel} = m_{A,h}^{*,\perp} = m_{B,h}^{*,\parallel} = m_{B,h}^{*,\perp}$
$\epsilon_{\mathrm{ZnO}}^{\parallel}$	$8.75\,\epsilon_0$	[76]	
$\epsilon_{\mathrm{ZnO}}^{\perp}$	$7.8\,\epsilon_0$	[76]	
ϵ_{ZnO}	$8.1\,\epsilon_0$	[74]	$3/\epsilon_{\mathrm{ZnO}}^{\perp} = 1/\epsilon_{\mathrm{ZnO}}^{\parallel} + 2/\epsilon_{\mathrm{ZnO}}^{\perp}$

Table 2.2: Band gap structure-related constants for ZnO: electron effective masses, hole effective masses, and static dielectric constant. The parameters m_e and ϵ_0 represent the free electron mass and vacuum permittivity, respectively.

2.1.4 Band-edge photoluminescence

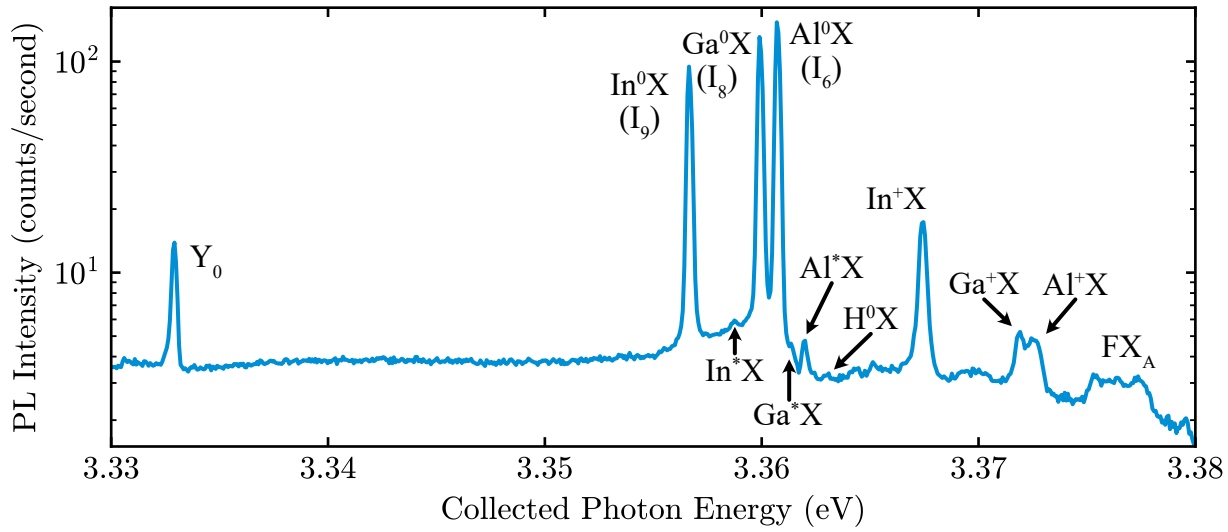

Figure 2.2: A photoluminescence (PL) spectrum of an indium-implanted TD ZnO substrate, taken at 1.7 K. The sample was excited with a 360 nm continuous wave (CW) laser focused near the diffraction limit, with 30 nW excitation power. The reported intensity corresponds to the detected electrons.

With incident light near or above the band gap energy at low temperatures, multiple sharp photoluminescence (PL) lines are observed. Emission near the band-edge is often related to recombination of excitons X (electron-hole pairs) that are either freely traveling throughout the lattice (FX) or bound to a defect such as structural imperfections and impurities (BX). In order to distinguish between these sharp PL lines we must use a spectrometer with high enough resolution. Fig. 2.2 shows an example PL spectrum taken at 1.7 K. In this spectrum we can identify emission related to recombinations of free excitons consisting from a conduction band electron and a valance A band hole (FX_A), neutral and ionized shallow donor-bound excitons (D^0X and D^+X, respectively) – some of which are historically noted as I-lines – and structural defect-bound excitons (Y-lines). Lastly, we can identify the neutral donor first excited bound exciton line as D^0X^* (described further in Chapter 5). The energy difference between the FX_A and a bound exciton recombination line is called the localization

energy ($E_{loc,\mathrm{B}} = E_{\mathrm{FX_A}} - E_{\mathrm{BX}}$). From the I-lines, the I_4 line has been identified as a bound excitonic line of the interstitial hydrogen donor (H_i^0), while I_6, I_8, and I_9 have been identified as bound excitonic lines of neutral Zn-substitutional aluminum, gallium and indium donors (Al_{Zn}^0, Ga_{Zn}^0, and In_{Zn}^0), respectively [76]. Here, we will focus on the substitutional neutral shallow donors Al^0, Ga^0, In^0, where the 'Zn' subscript is dropped for brevity.

2.2 Donor impurities

2.2.1 Introduction of donors to samples

As it was alluded earlier, chemical impurities can be introduced into the ZnO crystal *in situ* during growth. *In situ* impurity concentrations of Al, Ga, and In vary between different samples and different suppliers. Tokyo Denpa ZnO substrates host 10^{15} atoms/cm^3 to 10^{16} atoms/cm^3 of Al and Ga, while In concentrations are below 10^{14} cm^{-3}. Quantum communication protocols utilizing single defect qubits require a scalable method of defect synthesis. To that end, a straightforward solution to introducing defects on demand in existing bulk ZnO substrates is via ion implantation. This method is enabled by ionizing and subsequently accelerating the impurity of interest. The accelerated ions are directed to the target substrate. Varying the total kinetic energy of the ions determines the mean implantation depth, while changing the accelerated atom density and/or irradiation time determines the final concentration of impurities. However, this process can damage the surface and the volume of material ions traveled through and does not guarantee that the implanted impurities will occupy a Zn lattice site. Annealing (heating up) the sample to 700 °C for an hour in an O_2 atmosphere allows some fraction of the implanted impurities to occupy a Zn site and heals some of the implantation damage [81].

2.2.2 Donor properties

The neutral shallow donor, or D^0, in ZnO (Fig. 2.3) is an effective-mass impurity. It has one more electron compared to Zn, loosely bound to the positive donor nucleus. Since

the longitudinal and transversal effective electron masses and dielectric constants do not substantially differ from each other [73–76] (Table 2.2), these impurities can be approximated as a hydrogen-like system with an isotropic single electron mass (App. A.1). The energy difference of the effective 1s orbital level of a donor from the conduction band is called donor binding energy ($E_{b,\mathrm{D}}$). Following second order perturbation theory, this energy is modified by a mere 0.1 % due to the crystal anisotropy [76], inconsequential compared to the uncertainties of the effective mass and dielectric constants that define the donor binding energy. However, the short-range chemical potential of the impurity leads to a significant differentiation of the donor binding energy among impurity species [76] (Table 2.4). Higher level orbitals (2s, 2p) are more affected by the crystal anisotropy and are further modified due to interaction with optical phonons [76]. The effective D^0-electron Bohr radius (where the probability density is maximized) is about 1.6 nm (Table A.1). Lastly, the D^0-electron state is modified due to the electron-nuclear spin hyperfine interaction, which is different for different impurities. In the absence of an external magnetic field, the D^0 (1s) state, with degeneracy of $2(2I_\mathrm{D}+1)$, will be split in two manifolds with an energy difference of $A_\mathrm{D}\sqrt{1/4+I_\mathrm{D}(I_\mathrm{D}+1)}$, where A_D is the hyperfine constant (Table 2.4) and I_D is the nuclear spin (Table 2.3).

Atomic isotope	^{27}Al	^{69}Ga	^{71}Ga	^{113}In	^{115}In
Abundance (%)	100.00	60.11	39.89	4.28	95.72
Spin	5/2	3/2	3/2	9/2	9/2

Table 2.3: Relative abundance in nature, and nuclear spins of stable aluminum, gallium and indium [72]. It must be noted that ^{115}In is not stable, but its lifetime is estimated to be 441 Ty [72], four orders of magnitude larger than the current estimates of the age of the universe (13.8 Gy) [82].

The neutral donor is optically coupled to the neutral donor-bound exciton (D^0X) at cryogenic temperatures. As the temperature rises, the bound exciton will disassociate to a free exciton and a neutral donor with a disassociation activation energy nearly equal to the donor bound exciton localization energy [83]. The $D^0 \leftrightarrow D^0X$ transition energy is

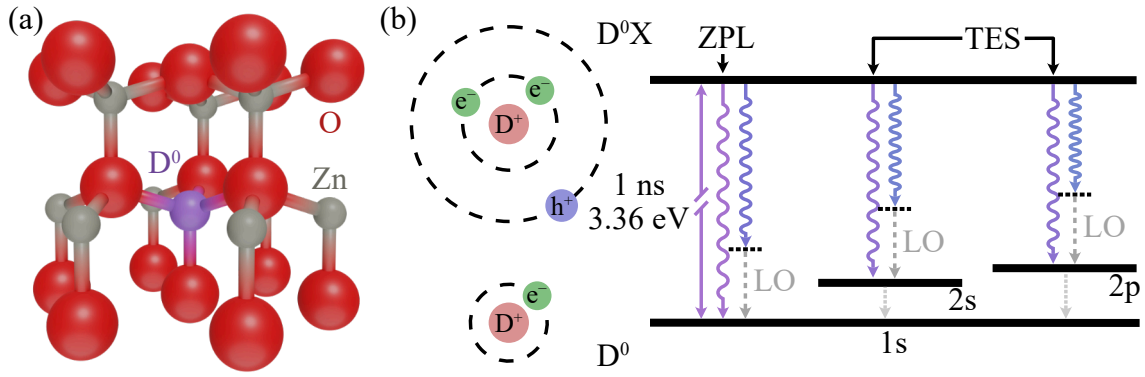

Figure 2.3: (a) A Zn-substitutinal shallow donor in wurtzite ZnO. (b) Donor and donor-bound exciton sketch and corresponding energy diagram. The sketch depicts the electron(s and hole) on the radial distance from the donor nucleus where the probability density is maximized. The energy diagram depicts the $D^0X \rightarrow D^0(1s)$, $D^0X \rightarrow D^0(2s)$, $D^0X \rightarrow D^0(2p)$ and their corresponding first phonon replicas. The energy level differences are not to scale, but can be found on Table 2.4.

approximately 3.36 eV near 0 K, with the exact value dependent on the donor species [76] (Table 2.4). Additionally, the $D^0X \rightarrow D^0$ transition is characterized by a "slow" radiative lifetime of ∼1 ns and a "fast" non-radiative lifetime of ∼ 300 ps, depending on the donor species [84, 85] (Table 2.4). The latter component is attributed to energy transfer from the D^0X to surface recombination centers that relax non-radiatively. [85]. During radiative relaxation from the D^0X state, approximately 90 % goes to the D^0 (1s) state with only the emission of a photon. This is the zero phonon line (ZPL). Approximately 5 % goes to the D^0 (2s) and D^0 (2p) state with only the emission of a photon (Table 2.4) – also called two electron satellite (TES) transitions – while the rest is phonon-assisted emission to various D^0 states (i.e. 1s, 2s, 2p, etc) – replicas with n number of longitudinal optical phonons (n-LO) [84] with energy $E_{LO} = 72$ meV [86]. All transitions are specific for each donor species and can be used as an identifying signature. We will primarily look at the TES, 1-LO, TES 1-LO, and 2-LO transitions, which we collectively call sideband transitions (Fig. 2.4). The phonon-assisted emission is characterized by the Huang-Rhys factor S, which determines the mean number of created phonons and takes the value of ∼0.06. The intensity of each replica

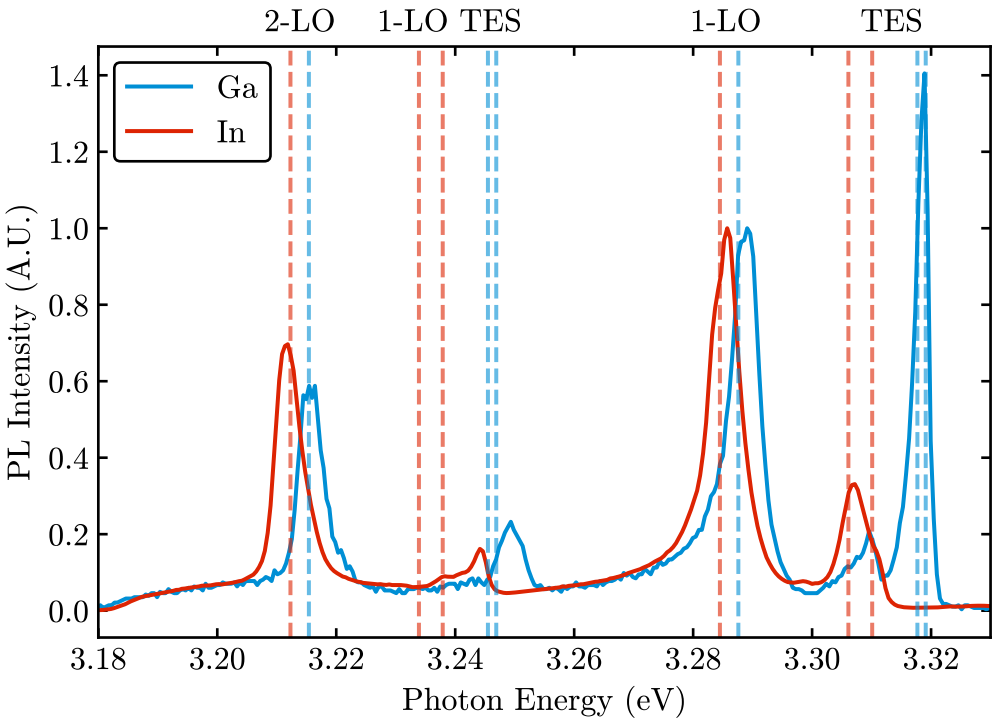

Figure 2.4: Photoluminescence spectra of sideband under resonant continuous wave excitation at 1.7 K and 0 T. The spectra were normalized to the maximum value of the 1-LO transition. Each family of lines is depicted at the top of the figure. The vertical dashed lines correspond to the specific literature value lines within the line family. Each species is represented by a different color corresponding to the spectrum color. For TES-related lines, there will be two lines, with the lower energy being the corresponding 2p line and the higher energy being the corresponding 2s line.

n follows a Poisson distribution [84]

$$I_n = e^{-S}\frac{S^n}{n}. \tag{2.1}$$

The oscillator strength of the $D^0 \rightarrow D^0X$ transition is near 0.35, with a corresponding dipole moment of 12 D (Sec. A.2). Similar to the D^0, the D^0X can be approximated with an effective mass system with a positive donor nucleus and three particles with independent wavefunctions (App. A.1). The two electrons spins form a spin-singlet state and interactions between them and the hole spin are expected to be small [87]. The effective D^0X-electron

Bohr radius is about 2.0 nm, while the D^0X-hole Bohr radius is about 3.3 nm (Table A.1).

Species	$H_i^0(I_4)$	EM	$Al^0(I_6)$	$Ga^0(I_8)$	$In^0(I_9)$
Bound Exciton ZPL (eV)	3.3628	(3.3614)	3.3608	3.3598	3.3567
Bound Exciton TES 2s (eV)	3.3278	(3.3236)	3.3228	3.3191	3.3101
Bound Exciton TES 2p (eV)	3.3287	(3.3240)	3.3220	3.3177	3.3061
Ion. Bound Exciton ZPL (eV)	-	(3.3742)	3.3734	3.3718	3.3676
Localization Energy (meV)	13.1	(14.5)	15.1	16.1	19.2
Binding Energy (meV)	46.1	50.2	51.6	54.6	63.2
Radiative Lifetime (ps)	570	–	750 – 860	800 – 1060	1050 – 1350
Non-radiative Lifetime (ns)	230	–	200 – 320	250 – 375	250 – N/A
Huang-Rhys factor	0.052	–	0.058	–	0.067
Hyperfine constant (MHz)	1.4	–	1.45	11.5	100.2

Table 2.4: Characteristic constants for different donor species including the pure effective mass donor. Bound exciton lines, localization energy, and binding energies were taken from Refs. [76, 84, 88]. The lifetime values are taken from Refs. [84, 85]. The Huang-Rhys factors are taken from [84]. The hyperfine constants where taken from Ref. [89] for H_i^0, Ref. [90] for Al^0, Ref. [91] for Ga^0, and Refs. [91, 92] for In^0. The effective mass (EM) donor is not observed, but the values are listed for comparison between the observed donors and the ideal hydrogen-like impurity.

2.2.3 Donors in the presence of magnetic field - a qubit platform

In the presence of large magnetic field B ($g_e\mu_B B \gg A_D$), where g_e the electron g factor and μ_B the Bohr magneton) the D^0 spin up ($|\uparrow\rangle$) and spin down ($|\downarrow\rangle$) electron states split due to the Zeemann effect. These two states constitute the electron spin qubit. Each electron spin state is a manifold consisting of $(2I_D + 1)$ energy levels due to the hyperfine interaction between the electron and the nuclear spin of the donor, with energy splittings equal to $A_D/2$. The D^0X state will split in two hole-spin manifolds due to the Zeemann effect on the hole, with hole spins up and down ($|\Uparrow\rangle$ and $|\Downarrow\rangle$, respectively). The electrons do not contribute

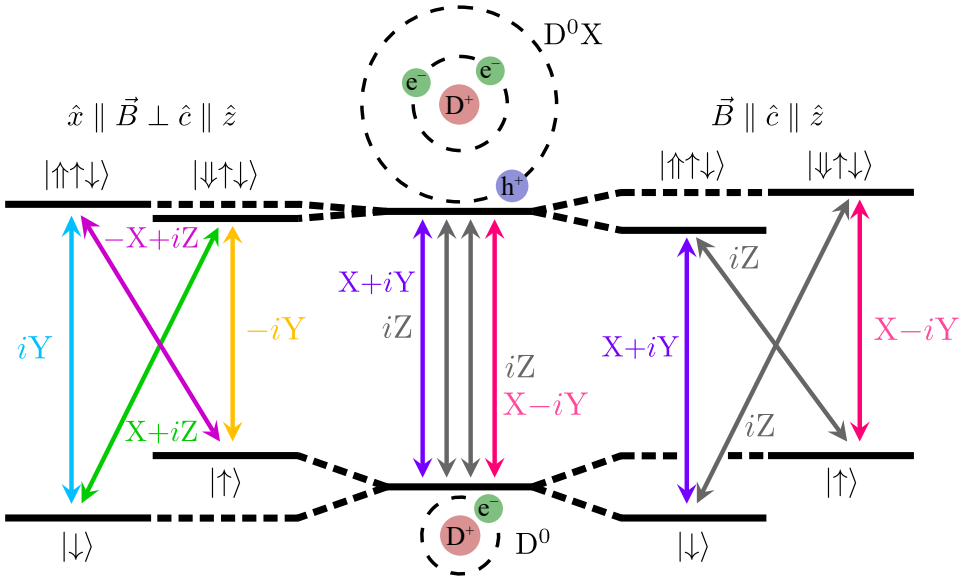

Figure 2.5: Energy diagram of D^0 and D^0X electron/hole spin states (nuclear spin is neglected) and $D^0 \leftrightarrow D^0X$ transition polarization selection rules in the absence (middle) and presence of magnetic field perpendicular (left) or parallel (right) to the crystal axis $\hat{c} \parallel \hat{z}$. The polarization selection rules are deduced by combining results in Refs. [53, 74, 93]. Here, $X = \frac{a}{\sqrt{2}}\hat{x}$, $Y = \frac{a}{\sqrt{2}}\hat{y}$, and $Z = b\hat{z}$ [93], where $a = 0.995$ and $b = 0.0999$ [74]. This figure is reprinted from Ref. [94].

to the splitting because they form a spin-singlet state ($|\uparrow\downarrow\rangle$). Consequentially, the D^0X state will not exhibit a substantial hyperfine splitting, since the hole wavefunction overlaps weakly with the donor nucleus (App. A.1). Due to the anisotropy of the crystal lattice, the hole g factor that determines the D^0X splitting is different for different magnetic field ($\vec{B}$) orientations. Figure 2.5, shows the energy level splittings and polarization selection rules for the different magnetic field orientations.

Throughout most of this thesis, the optical $\hat{k}$ axis is parallel to the crystal $\hat{c}$ axis. In this configuration (Fig. 2.6a-b), we have the Voigt ($\vec{B} \perp \hat{c}$) and Faraday ($\vec{B} \parallel \hat{c}$) geometries. In the Voigt geometry we detect four linearly polarized transitions, and in the Faraday geometry two circularly polarized transitions. Photons emitted via the two cross transitions in the Faraday geometry will primarily travel perpendicular to the crystal $\hat{c}$ axis and will

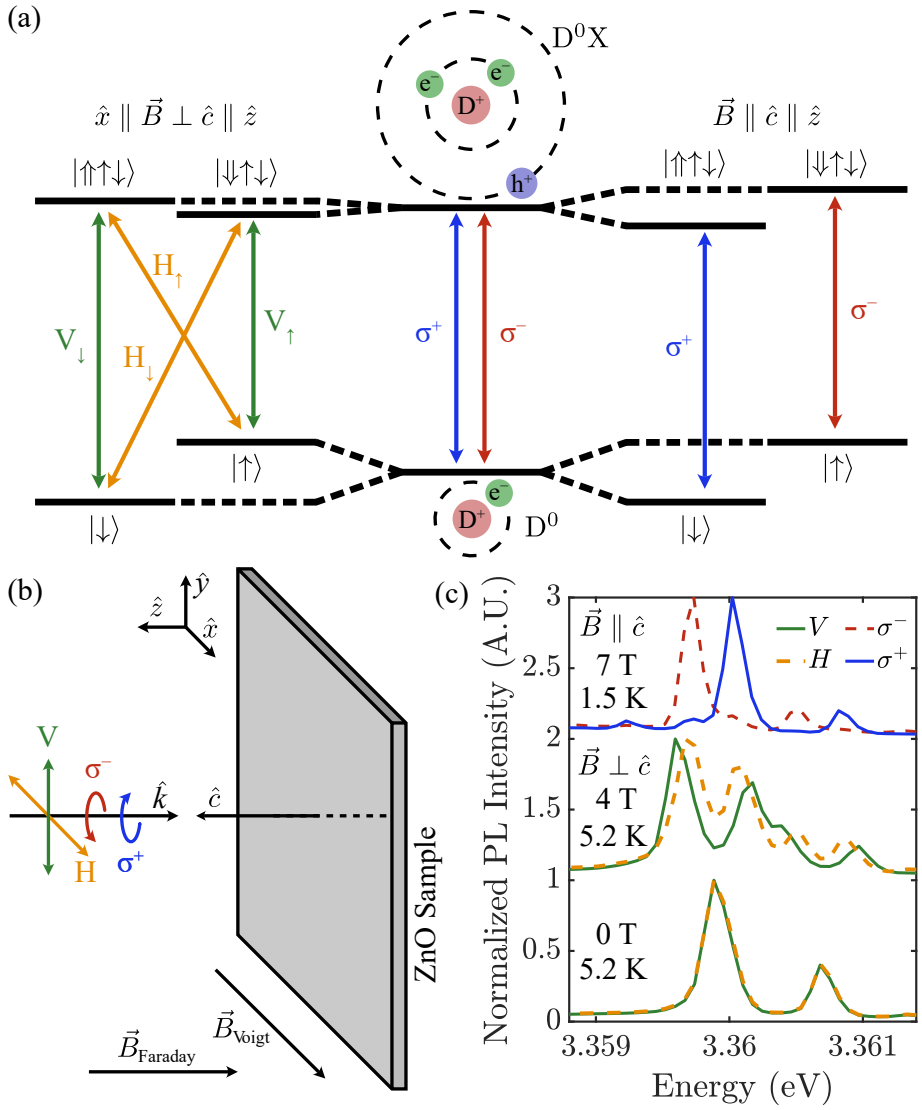

Figure 2.6: (a) Energy diagram of D^0 and D^0X electron/hole spin states (nuclear spin is neglected) and $D^0 \leftrightarrow D^0X$ transition polarization selection rules in the absence (middle) and presence of magnetic field perpendicular (left) or parallel (right) to the crystal axis $\hat{c} \parallel \hat{z}$, when the incident light is parallel to the crystal axis ($\hat{k} \parallel \hat{c}$). V_s, H_s, σ^+, and σ^- represent the vertically linear, horizontally linear, right-handed circular, and left-handed circular polarizations, with the subscript 's' denoting the electron spin state the transitions are associated to. (b) A schematic representation of the sample orientation with respect to the magnetic field and the various incident polarizations. (c) PL spectra under 3.45 eV excitation of *in situ* Al and Ga donor ensembles ($\sim 10^4 - 10^5$) in a TD ZnO substrate with an 700 nm MBE layer grown on top on the Zn-face in different magnetic field configurations. Most collected PL is *not* from the MBE layer. (b) and (c) are reprinted from Ref. [95] with permission from APS.

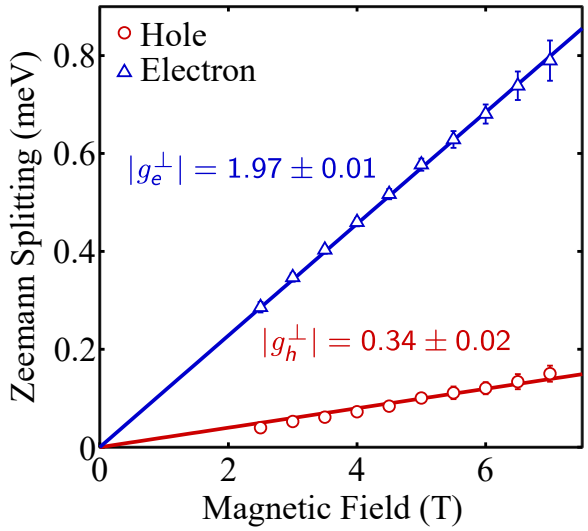

Figure 2.7: Electron and hole Zeeman splitting of Ga donor ensembles (same sample as in Fig. 2.6 as function of the magnetic field in the Voigt geometry. Each point is obtained via Gaussian profile fits of PL spectra under 3.45 eV excitation at different fields and 5.2 K. The error bars depict the standard deviation error of the Gaussian profile fits. The red and blue lines are linear fits of the Zeeman splitting. This figure is reprinted from Ref. [54] with permission from APS.

not be observed. Fig. 2.6c shows PL at zero magnetic field, Voigt, and Faraday geometries, showcasing the different observed transitions.

We can experimentally determine the electron and hole g factors by performing PL spectroscopy over a range of magnetic fields (magneto-PL) and measure the energy difference between the various $D^0X \rightarrow D^0$ transitions. Magneto-PL measurements of donor ensembles reveal that the electron g factor is nearly isotropic with $g_e^{\parallel} = g_e^{\perp} = g_e = 1.95 - 1.97$ [54, 81, 96], while the hole g factor is highly anisotropic, with $-g_h^{\parallel} = 1.2 - 1.32$ and $g_h^{\perp} = 0.1 - 0.34$ [53, 54, 81, 95, 96]. Fig. 2.7 depicts the electron and hole Zeeman splitting in the Voigt geometry and allows us to estimate the electron and hole g factors, $g_e^{\perp}$ and $g_h^{\perp}$, with

$$\begin{aligned} g_e^{\perp}\mu_B B &= E_{V_\downarrow} - E_{H_\uparrow} = E_{H_\downarrow} - E_{V_\uparrow} \\ g_h^{\perp}\mu_B B &= E_{V_\downarrow} - E_{H_\downarrow} = E_{H_\uparrow} - E_{V_\uparrow}, \end{aligned} \tag{2.2}$$

where E_i is the energy of transition i as marked in Fig. 2.6. Assuming $g_e^{\perp} = g_e^{\parallel}$, we can

determine the $g_h^{\parallel}$ by measuring the energy difference between the two $D^0X \rightarrow D^0$ transitions in the Faraday geometry and calculate the hole g factor from the measured effective g factor $g_{\text{eff}}^{\parallel} = g_e^{\parallel} + g_h^{\parallel}$ with $g_{\text{eff}}^{\parallel}\mu_B B = E_{\sigma^+} - E_{\sigma^-}$ (Fig. 2.8).

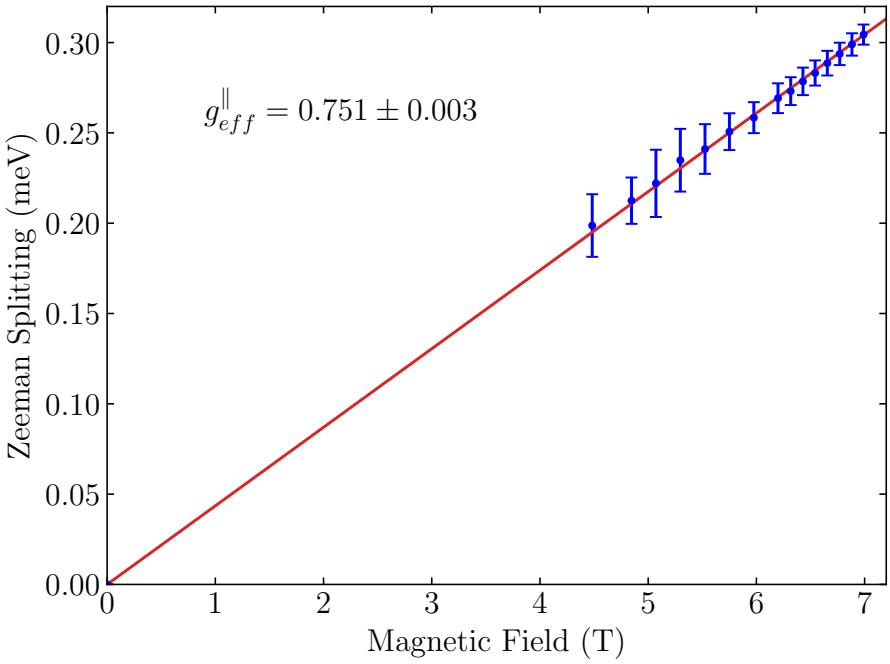

Figure 2.8: Effective Zeeman splitting of Ga donor ensembles (same sample as in Fig. 2.6 as function of the magnetic field in the Faraday geometry. Each point is obtained via Gaussian profile fits of PL spectra under 3.45 eV excitation at different fields and 5.2 K. The error bars depict the standard deviation error of the Gaussian profile fits. The red and blue lines are linear fits of the Zeeman splitting. This figure is reprinted from Ref. [95] with permission from APS.

Chapter 3

EXPERIMENTAL SETUP AND TECHNIQUES

This chapter describes the experimental set-up for fundamental property measurements, including the optical transition linewidth and longitudinal spin relaxation time. We start by describing the base experimental setup, including the microscope, cryostat, and detectors. We next describe various photoluminescence excitation (PLE) measurements, the experimental procedure used to measure the optical transition linewidth. We also describe transmission measurements and how we use them to calculate the optical depth. Lastly, we explain how we optically initialize the spin state with optical pumping (OP) and how this process allows us to measure T_1 and probe transient properties of the optical linewidth.

3.1 Base experimental setup

For all experiments described in this dissertation we use the same base experimental setup. We use a home-built optical microscope assembled on a breadboard for ease of movement between different optical access configurations to a cryostat. While the general microscope structure remains the same, individual components are moved in and out depending on the specific experiment. Figure 3.1a provides a schematic of this base setup.

Usually, the microscope has one or more laser excitation sources – either fiber-coupled or free-space. All excitation sources are combined to a single excitation path, either by using beam splitters or mirrors on flip mounts (BS1 in Fig. 3.1a). We used three different laser systems for above band and resonant excitation. For near above band excitation, we used a CNI MSL-F-360-10mW, which is a continuous wave (CW) laser emitting near 360 nm with a maximum power of 10 mW. For resonant excitation and tunable frequency control we used a SpectraPhysics Matisse-TS Ti:sapphire laser emitting near 738 nm. The Matisse is pumped

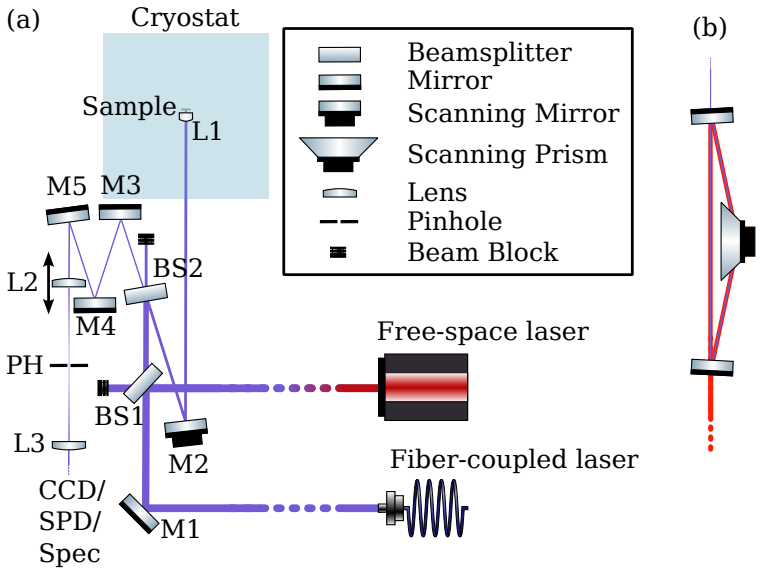

Figure 3.1: Principle design of optical path for various experiments, featuring one or more free-spaced or fiber-coupled excitation lasers to enable confocal imaging of samples in cryogenic temperatures using a CCD, spectrometer, or single photon detector. This figure is reprinted from Ref. [97] with permission from Optica Publishing Group under the Optica Open Access Publishing Agreement.

by a SpectraPhysics Millenia EV CW DPSS 532 nm green laser with a maximum power of 15 W. Under a pump power of 9.5 W, the Matisse emits at 738 nm with 1.4 W of power. The Matisse is doubled to 369 nm with a SpectraPhysics WaveTrain frequency doubler, which utilizes a nonlinear crystal with a unidirectional ring cavity (Fig. 3.1b) and yields a conversation efficiency between 4% and 10%. For two-laser pump-probe measurements the second resonant excitation laser is a Toptica DL pro HP external cavity diode laser emitting near 368.9 nm with a maximum power of 30 mW. The laser emission contains a long tail in the longer wavelength regime, which we filter. Finally, we use the Ti:Saphire SpectraPhysics Tsunami, a pulsed laser configured for 2 ps pulse with a repetition rate of 80 MHz for above band pulsed excitation and lifetime measurements.

Since excitation and collection share a path (reflection from BS2 to sample and back in Fig. 3.1a), we use a beam splitter to allow the emitted photoluminescence (PL) to go to our

detectors. Hence, the excitation path consists of a beam splitter (BS2 in Fig. 3.1a) and a mirror mounted on a piezo-mirror mount (M2 in Fig. 3.1a). The beam splitters we use for the excitation path have a nominal reflection-transmission percentages of either 50 % - 50 % or 5 % - 95 %. While the former is great for measurements where high excitation power is important, the latter is used when the PL signal is weak to we detect as much PL as possible. The mirror on the piezo-mount is used to enable scanning confocal microscopy, which we only use for finding spatially isolated single emitters (App. C.2). Instead of the more established practice of using an objective to focus the beam on the sample, we use a 3.1 mm focal length aspheric lens (L1 in Fig. 3.1a), since the cryostat space is limited and current technologies do not yet permit for small footprint near-UV cryogenic objectives. This limits the numerical aperture of the collected PL to 0.62 (equivalent to a 38° light cone) and results in significant chromatic aberrations. The spot diameter on the sample is measured to be $\sim$ 500 nm.

Once the collection path is split from the excitation path (transmission from BS2 to M3 in Fig. 3.1a), the PL is focused with L2 onto a confocal pinhole (PH) setup, to spatially filter the PL from a small depth range. Due to chromatic aberrations, the image of the reflected input beam is not in the same plane as the image of the PL. Therefore, we adjust the lens L2 of the confocal setup to move between the imaging planes we are interested in. After the PL is collimated (L3 in Fig. 3.1), the collection path leads to three different detectors with the use of flip mirrors: (1) a simple CCD camera for looking at the reflection of the input beam focused on the sample or the emitted PL, (2) an Andor Shamrock 750 spectrometer (Spec) with a Newton DU920P-UVB CCD and a turret with either NIR or near-UV gratings (for the NIR we use the second order, which is not very efficient, but results in higher resolution) to distinguish the photon energy of the PL, (3) a single photon counting module (SPCM) COUNT BLUE COUNT-50B from Laser Components that has a 1 ns timing resolution and is more sensitive in collecting single photons than the spectrometer CCD camera.

All of our optics are graded for use in the near-UV regime. Some notable equipment part numbers are listed below. Our mirrors are either MaxMirror (ultra broadband mirrors) or Thorlabs BB1-E01. For 50/50 beam splitters, we either use Thorlabs BSW21, Newport

UVBS14-1, or Thorlabs PBS051. Achromatic lenses in the confocal pinhole setup are Newport PAC18AR.15, the ashperic lens in the cryostat is a Edmund Optics LightPath 354330, and fiber-coupler aspheric lenses are Thorlabs C610TME-A, C560TME-A, or A397TM-A. Our polarizers are either a Thorlabs A-coated Glan-Thompson GTH or a Thorlabs LPUV050. The waveplates we use are EKSMA Optics 464-4240 ($\lambda/2$) and 464-4440 ($\lambda/4$). The 'PL' filters we use are BrightLine single-band band pass 370/6 nm and BrightLine single-band band pass 380/14 nm. In the rest of this chapter, more detailed schematics are provided for specific experiments.

The samples are mounted in a helium immersion cryostat with a superconducting magnet. The cryostat is operated with a liquid helium reliquifier. This prevents helium losses due to helium evaporation. The cryostat can reach down to 5.2 K without helium loss. The sample is not immersed in liquid helium (LHe), but is rather above the LHe level in the evaporated helium gas. For lower temperatures, we can reduce the pressure in the sample space so that the gas-liquid phase-change temperature is reduced. This can be achieved by pumping on the sample space with the sample either in gaseous or superfluid helium. The former method is stable for temperatures between 2 K and (at least) 6 K, while the later allows us to reach the range of 1.5 K to 2 K. Magnetic fields $\vec{B}$ between ± 7 T can be reached with its direction is fixed. The cryostat has four windows allowing for access of different $\vec{B}$ field directions by moving the optical microscope Alternatively, we can access different $\vec{B}$ field orientation with respect to the crystal orientation by rotating the sample on the plane parallel to the surface of interest.

3.2 Photoluminescence excitation spectroscopy and linewidth

As we have seen in Chapter 2, various optically active defects can be observed, including donors coupled to donor-bound excitons by optically exciting a donor ensemble with photon energy near or above the band gap. In addition to the ZPL, the donor bound exciton state relaxes to the D^0 1s state via different channels (e.g., via other D^0 orbital states or via phonon replicas, collectively called the sideband), which can be used as a species identifier.

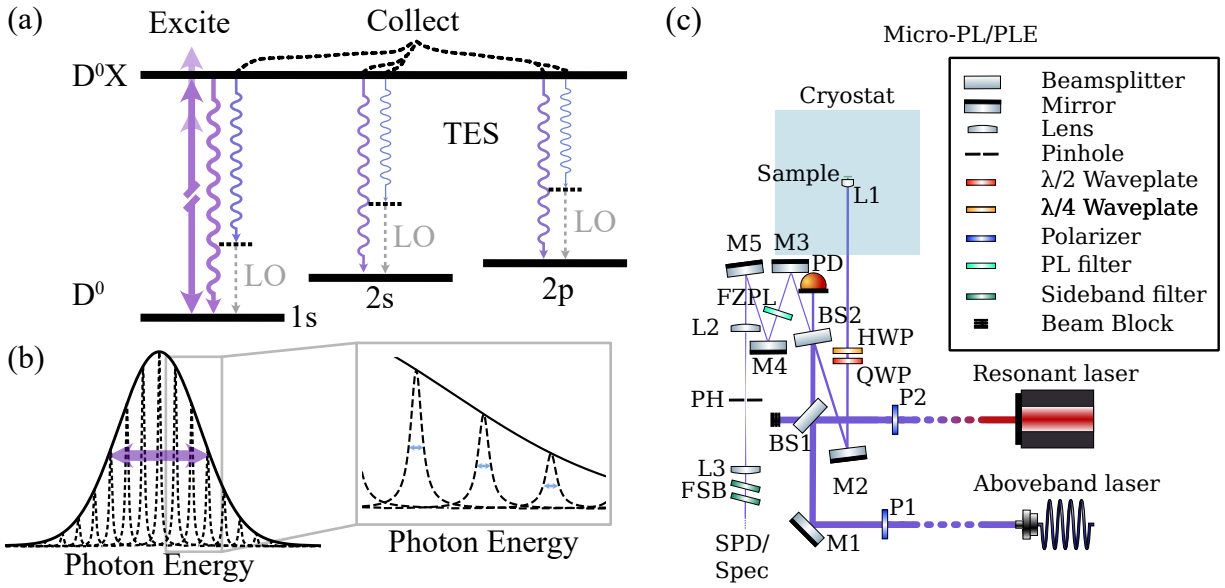

Figure 3.2: (a) Energy level schematic of PLE measurements, where a CW laser is scanned near the $D^0 \leftrightarrow D^0X$ resonance, while collecting sideband PL. (b) Schematic of Voigt profile (convolution of a Gaussian and a Lorentzian profile) where the array of Lorentzians represents an array of evenly spaced sub-ensembles. In the left inset, the purple arrow denotes the total linewidth of the Voigt profile. In the right inset, the blue arrows denote the homogeneous linewidth of the Lorentzian profile. (c) Optical paths for the micro-PL/PLE experiments, where The emitted PL is collected with either an single photon counter (SPD) or a spectrometer. The photo-diode (PD) is used as a power reference when scanning the probe laser to correct for power fluctuations induced by wavelength dependent transmission/reflection of the beam splitter. Subfigure (c) is reprinted from Ref. [97] with permission from Optica Publishing Group under the Optica Open Access Publishing Agreement.

While above-band gap excitation is useful to identify emitters in the substrate, additional information can be obtained with resonant absorption and emission.

Photoluminescence excitation (PLE) spectroscopy (Fig. 3.2a), in which a continuous wave laser is scanned near the transition resonance of interest while collecting emitted PL, allows the measurement of the transition linewidth. The linewidth is important because photon-based quantum communication applications require photon indistinguishability both in frequency and time domains. In addition, the linewidth and frequency dependence on external variables such as temperature and magnetic field may help decipher the fundamental mech-

anisms with which the donor system interacts with its environment.

In the ideal case, the lineshape of a transition in the frequency domain is related to the transition relaxation profile in the time domain by means of the Fourier transform (FT) of the wavefunction. For an exponentially decaying wavefunction amplitude with a lifetime τ, the Fourier transformed wavefunction's amplitude is a Lorentzian profile. In this case, the linewidth Γ – defined as the full width at half maximum of the resonance – is given by

$$\Gamma = \frac{1}{2\pi\tau}, \tag{3.1}$$

and is called the Fourier-transformed lifetime limit. As we will see in Chapters 5 and 6, transitions can be broadened by different interactions with the environment in two main ways, homogeneously, and inhomogeneously. Homogeneous broadening occurs when all emitters in an ensemble are broadened in the same way, regardless of their local environments. Examples of homogeneous broadening include photon-interactions, and coherent excitation power broadening effects. In contrast, inhomogeneous broadening occurs when the emission is affected differently between different emitters, and usually has to do with interactions with the microscopic environments, such as the presence a paramagnetic charge trap, or the nuclear isotopic environment.

Mathematically, each different broadening mechanism will be convolved with the lifetime-limited linewidth. Homogeneous effects tend to be Lorentzian in nature, and since the convolution of two Lorentzians is a Lorentzian, the two linewidths are simply added. Inhomogeneous effects tend to be Gaussian in nature, and the convolution of a Gaussian with a Lorentzian will result in a Voigt profile (Fig. 3.2b), whose linewidth can be approximated by a the contributing Gaussian Γ_{G} and Lorentzian Γ_{L} contributions [98]

$$\Gamma_{\mathrm{total}} = \frac{\Gamma_{\mathrm{L}}}{2} + \sqrt{\frac{\Gamma_{\mathrm{L}}^2}{4} + \Gamma_{\mathrm{G}}^2}. \tag{3.2}$$

These are the mathematical tools we use to describe PLE lineshape in all chapters.

The transition choice for collected PL depends on various experimental restrictions. In principal, we could excite and collect the same transitions (ZPL). However, filtering the

excitation can be challenging. Thus, throughout most of this thesis, we perform PLE while collecting sideband emission (Fig. 3.2a). With this method, we can spectrally filter the excitation and collection.

The experimental setup to perform PLE measurements on donors a up to few microns from the surface (micro-PLE) is very similar to the base setup and is depicted in Fig. 3.2c. In addition to the base setup, we use a polarizer (P2 in Fig. 3.2c) in the excitation path, as well as half and quarter waveplates (HWP and QWP) in the excitation/collection path to set the appropriate excitation polarization. We also add a photodiode (PD) to collect reference power data for the excitation laser because both the 50-50 beam splitter transmission/reflection coefficients and the output power from the doubling cavity are wavelength dependent. In the collection path we add two sideband filters (FSB) to cut both the Y-line emission very close to the TES transitions as well as the retroreflected probe laser. As for the experimental process, first we find the central frequency of the transition of interest from the above band excitation PL spectrum. Then, we scan the resonant laser frequency while detecting sideband PL with either the spectrometer or the SPCM. We also measure the laser power transmitted through the BS2 beamsplitter on the PD photodiode to correct for the frequency dependence of the incident power on the sample, as described in App. A.4. The scan is performed in discrete steps where at each step the donor system has time to reach a steady state.

3.3 Transmission measurements and optical depth

As we have seen in Sec. 1.1.2, the optical depth is an important metric to optical quantum memories. We can measure the optical depth at a given donor ZPL with transmission measurements. In the approximation of small transmittance, valid due to near band edge absorption, the optical depth is

$$OD = \alpha d = \ln\left(\frac{(1-R)^2}{T}\right), \tag{3.3}$$

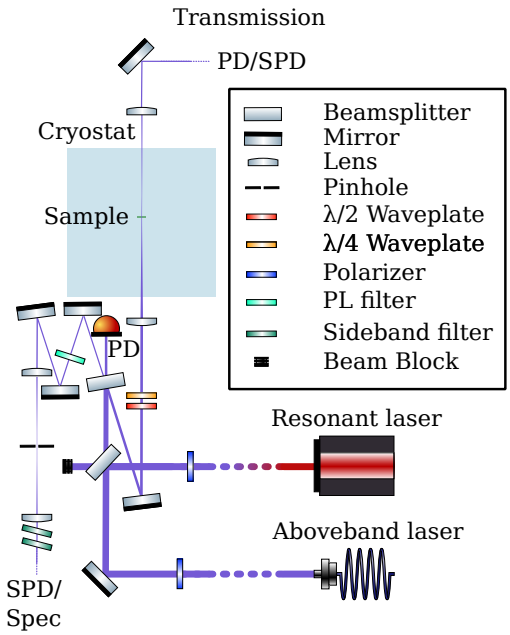

Figure 3.3: Optical path for the transmission experiments, where the transmitted laser power is measured with either with a PD or a calibrated SPD. The input power is calculated by the picked-off input laser in the microscope's excitation path. This setup still allows for measurement of emitted PL in the spectrometer. This figure is reprinted from Ref. [97] with permission from Optica Publishing Group under the Optica Open Access Publishing Agreement.

where R and T are the experimentally measured reflectance and transmittance, respectively. Refer to App. A.3 for a derivation of this approximation.

Similar to PLE measurements, in transmission measurements we scan a continuous wave laser near the resonance of interest. We measure the incident and transmitted laser powers. Unlike micro-PLE which only probes donors a few microns from the surface, transmission measurements probe donors throughout the entire sample.

For focusing the excitation beam on the sample and collimating the transmitted beam, we use two 200 mm focal length lenses that are placed outside the cryostat. These yield a spot diameter of about 40 µm. Figure 3.3 depicts the optical path schematic for this type of measurement.

3.4 *Optical pumping and spin relaxation measurements*

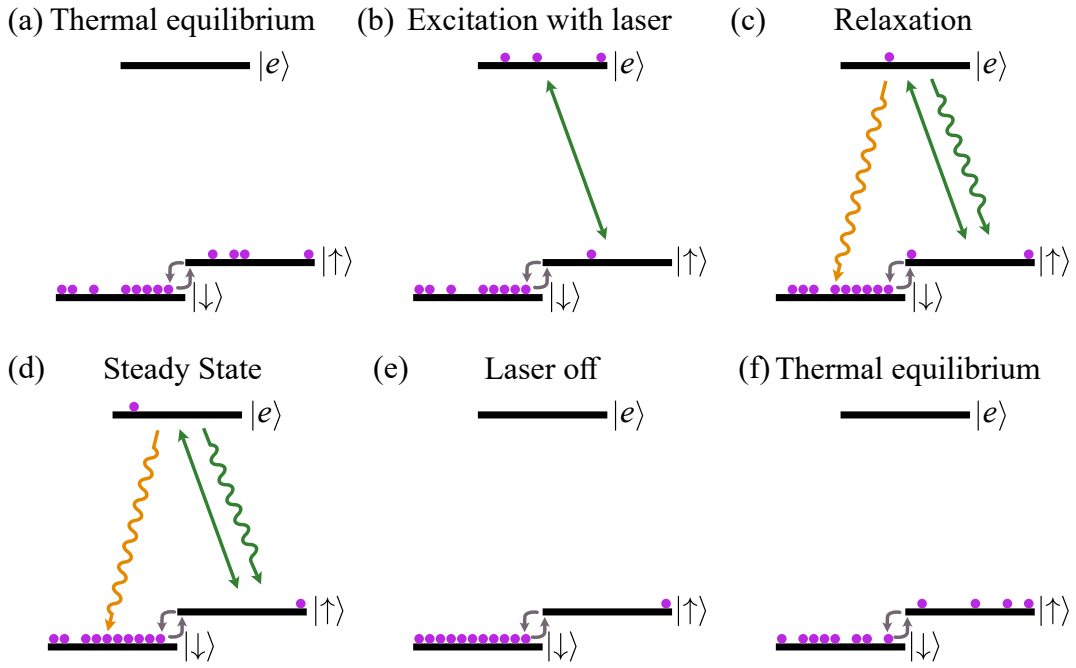

Figure 3.4: Energy level diagrams showing the pulsed optical pumping process for a 3-level Λ-system.

Optical pumping (OP) is a method to change the state of a quantum system with the use of a third intermediary state optically coupled to the initial and final state. We can use this process to initialize our qubit to the $|\uparrow\rangle$ or $|\downarrow\rangle$ state using one of the D^0X states. Let us assume an ensemble of shallow donors in ZnO at cryogenic temperatures ($\sim 4\,K$) in the presence of magnetic field in the Voigt geometry with the crystal axis $\hat{c}$ parallel to the optical axis $\hat{k}$. In these temperatures, most of the population will occupy the less energetic $|\downarrow\rangle$ state (Fig. 3.4a). We initialize the qubit to the $|\uparrow\rangle$ state with a laser resonant to either the $H_\downarrow \equiv |\downarrow\rangle \leftrightarrow |\Downarrow\uparrow\downarrow\rangle$ or the $V_\downarrow \equiv |\downarrow\rangle \leftrightarrow |\Uparrow\uparrow\downarrow\rangle$ transitions. For simplicity, Fig. 3.4 depicts only one D^0X state, marked as $|e\rangle$. The laser will excite the $|\downarrow\rangle$ population to the $|e\rangle$ state. Due to the finite lifetime of the$|e\rangle$ state, the population will relax back to one of the D^0 states (Fig. 3.4c). In this specific case, due to the chosen geometry, the probability to relax

to either the $|\uparrow\rangle$ or $|\downarrow\rangle$ state is approximately 50 %. Over time, the population that relaxed to the $|\downarrow\rangle$ state will be re-excited and relax over and over again until, after some time, nearly the entire population is in the $|\uparrow\rangle$ state (Fig. 3.4d). In order to measure this behaviour we can collect PL from any observable transition from $|e\rangle$. The PL intensity from $|e\rangle$ will be proportional to the population in the $|\uparrow\rangle$ state. Hence, collecting PL while illuminating the donor ensemble will result in an exponentially decaying PL that eventually reaches a steady state, where the decay rate depends on the relaxation time, excitation power, and branching ratio from the $|e\rangle$ to the final states. Such 3-level systems can be described mathematically by a set of rate equations, as it is done for example in Ref. [99].

If there were no other processes taking place, the ensemble would stay in the $|\uparrow\rangle$ state even when the excitation laser is off. However, there is also relaxation between the $|\uparrow\rangle$ and $|\downarrow\rangle$ states, which eventually brings the donor ensemble back to thermal equilibrium (Fig. 3.4e and Fig. 3.4f). This spin relaxation time T_1 is an important qubit metric, since it serves as the ultimate limit of the coherence time T_2. In order to measure the amount of time it takes for the spins to relax back to thermal equilibrium, we need to monitor one of the two states' population as a function of 'laser-off' time. To realize this measurement, we perform sequential OP measurements with varying wait-time between measurements. As we mentioned earlier, the PL intensity is proportional to the state's population. Hence, if we integrate a small window of time in the beginning of the OP curve, we can have a measure of the initial population of the $|\uparrow\rangle$ state as a function of 'laser-off' or wait-time. In this measurement, the integrated PL intensity in the beginning of each OP process will increase with increasing wait-time, meaning that the $|\uparrow\rangle$ state is being repopulated. This is an exponential behaviour which can be fitted with an exponential curve, whose exponent coefficient is the spin relaxation time T_1.

As was the case with PLE measurements, the transition from which we choose to collect PL is determined by the experimental geometry. Collecting ZPL is challenging under resonant excitation because it is difficult to distinguish the emitted ZPL from the excitation beam retroreflection. Two ways to achieve that in the presence of strong magnetic field is

by either collecting transitions with different polarization (and slightly different frequency) compared to the excitation beam or collecting the sideband transitions whose transition wavelength is more than 10 nm away from the ZPL. These two methods are employed when performing optical pumping or spin relaxation measurements in Chapters 4 and 5.

3.5 Two-laser photoluminescence excitation measurements

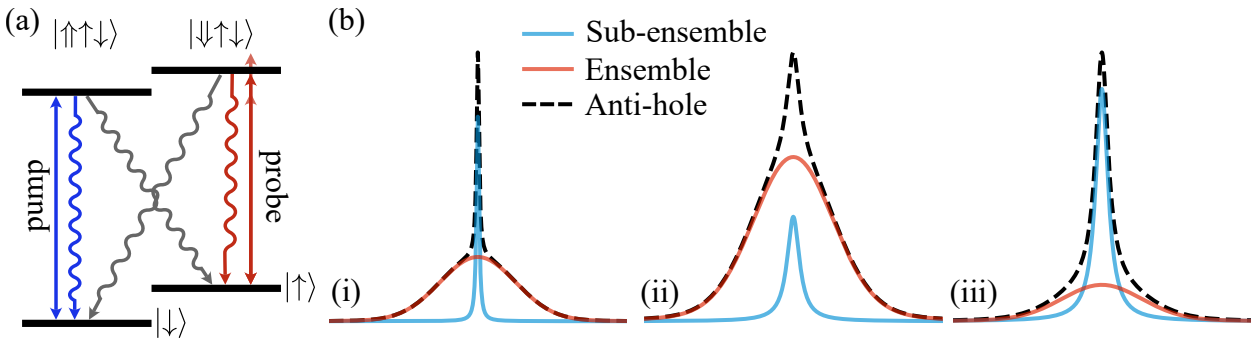

Figure 3.5: (a) Energy level diagram for a two laser anti-hole measurement in the Faraday geometry. The two lasers do not address the same states. (b) Expected behaviour of anti-hole measurements (i) $\Gamma_{\text{hom}} = \Gamma_{\text{inh}}/25$ and (ii, iii) $\Gamma_{\text{hom}} = \Gamma_{\text{inh}}/5$, where Γ_{hom} and Γ_{inh} correspond to the homogeneous and inhomogeneous linewidth contributions, respectively, with a homogeneous contribution amplitude: $a_{\text{hom,iii}} = 10a_{\text{hom,ii}} = 10a_{\text{hom,i}}$.

While PLE is an excellent way to measure a resonance's total linewidth, it does not allow us to measure the homogeneous contributions to the linewidth for an ensemble of donors. However, adding a second (pump) laser to the PLE measurement allows us to probe the specific subensemble resonant with the pump and, hence, the homogeneous linewidth (Fig. 3.5a). Assume that we have an inhomogeneously broadened donor ensemble in ZnO and that the magnetic field is oriented in the Voigt geometry. If we set the pump laser on the $|\downarrow\rangle \leftrightarrow |\Uparrow\uparrow\downarrow\rangle$ (Fig. 3.5a) transition resonant with a specific sub-ensemble of donors, the sub-ensemble population will be optically pumped to the $|\uparrow\rangle$ state. If the probe laser scans the $|\uparrow\rangle \leftrightarrow |\Downarrow\uparrow\downarrow\rangle$ transition (Fig. 3.5a), we should observe two different features. The sub-ensemble to which the pump laser is *not* resonant will emit PL as if there was no pump

laser on (red curve in Fig. 3.5b). However, the sub-ensemble to which the pump laser *is* resonant will experience a cycling of population between the $|\uparrow\rangle$ and $|\downarrow\rangle$ states, resulting in a substantially increased PL at this frequency, called an anti-hole (blue curve in Fig. 3.5b). As we see in Fig. 3.5b, the anti-hole becomes harder to distinguish from the ensemble linewidth the closer the homogeneous linewidth is to the inhomogeneous one. Furthermore, depending on the efficiency of the population cycling, the sub-ensemble contribution can become so large that the ensemble contribution will be insignificant in comparison (Fig. 3.5biii). Hence, the collected PL is the sum of the two contributions, an inhomogeneously broadened background and a more intense homogeneously broadened resonance, thus rendering this measurement a tool in determining the nature of transition linewidth broadening.

Experimentally, we have to bring both lasers in the same optical path using a beam splitter, and the beams must spatially overlap. Similarly, the beam diameters must be the same, otherwise one beam could address a larger amount of population than the other and therefore reduce the observed anti-hole contrast. Therefore, the best option is to bring the two beams on the microscope via a single fiber output, where the individual outgoing beam profiles will be exactly the same. Additionally, since the transitions we are exciting are oppositely polarized, we must set each polarization before the beam splitter.

3.6 Time-resolved photoluminescence excitation measurements

Both single- and two-laser PLE measure the emitted PL while the quantum system is in a steady state, an equilibrium state different from thermal equilibrium due to the presence of two driving optical fields. Hence, these measurements prevent the measurement of time-dependent effects on the linewidth such as spectral diffusion. Time dependent effects can be probed with time-resolved two-laser PLE measurements. Time resolved two-laser PLE draws from techniques used for OP and two-laser PLE measurements. Let us assume an inhomogeneously broadened donor ensemble. The pump laser is set resonant to a sub-ensemble (e.g. with transition $|\downarrow\rangle \leftrightarrow |\Uparrow\uparrow\downarrow\rangle$ from Fig. 3.5a) and pulsed at the beginning of the measurement sequence so that the qubit is initialized to the $|\uparrow\rangle$ state. After a delay

time, the probe laser pulse, set near the $|\uparrow\rangle \leftrightarrow |\Downarrow\uparrow\downarrow\rangle$ resonance (Fig. 3.5a), probes a specific sub-ensemble. This method allows us to track the PLE linewidth as a function of probe-on time, by integrating the PL collected during the probe laser pulse at different time instances.

Experimentally, we set each laser at a given frequency and collect the emitted sideband PL throughout multiple pump-probe cycles. During these cycles, the probe laser frequency remains constant. Only at the end of a set of experiments do we change the probe laser frequency and initiate a new collection session. Therefore, this process provides information about the average behavior during a given probe-on time window, but it does not capture individual instances of instantaneous spectral diffusion or spectral drift.

Chapter 4

LONGITUDINAL SPIN RELAXATION OF DONOR ENSEMBLES

Unless noted otherwise, originally published as [95]: V. Niaouris, M. V. Durnev, X. Linpeng, M. L. K. Viitaniemi, C. Zimmermann, A. Vishnuradhan, Y. Kozuka, M. Kawasaki, and K.-M. C. Fu, "Ensemble spin relaxation of shallow donor qubits in ZnO", Phys. Rev. B **105**, 195202 (2022).

Reprinted with permission from APS.

In this chapter, we present an experimental and theoretical study of the longitudinal electron spin relaxation (T_1) of shallow donors in the direct band-gap semiconductor ZnO. T_1 is measured via resonant excitation of the Ga and In donor-bound exciton for *in situ* Ga and implanted In ensembles. T_1 exhibits an inverse-power dependence on magnetic field $T_1 \propto B^{-n}$, with $4 \leq n \leq 5$, over a field range of 1.75 T to 7 T. We derive an analytic expression for the donor spin-relaxation rate due to spin-orbit (admixture mechanism) and electron-phonon (piezoelectric) coupling for the wurtzite crystal symmetry. Excellent quantitative agreement is found between experiment and theory suggesting the admixture spin-orbit mechanism is the dominant contribution to T_1 in the measured magnetic field range. Temperature, excitation-energy, and implantation fluence dependent measurements indicate a donor density dependent interaction may contribute to small deviations between experiment and theory. The longest T_1 measured is 480 ms at 1.75 T with increasing T_1 at smaller fields theoretically expected. This work highlights the extremely long longitudinal spin-relaxation time for ZnO donors due to their small spin-orbit coupling.

4.1 Introduction

Long coherence times are an essential requirement of quantum computation and communication networks [28]. The coherence time of a qubit is ultimately limited by the relaxation time between the two qubit states. Therefore, the relaxation time is an important metric of the a qubit's potential. Understanding the mechanisms that govern state relaxation can also reveal how the qubit interacts with its environment and how to extend the relaxation time. Spin relaxation of quantum dots in semiconductors have been investigated both on a theoretical and experimental level [43, 100–104]. A recent study made significant steps towards understanding the more robust spin donor systems in three semiconductors of the III-IV and II-VI groups [105]. While the spin relaxation time of shallow donors in ZnO has been investigated to some extent experimentally, a theoretical description remained elusive. Here, we study the dependence of T_1 on magnetic field, temperature and excitation energy to gain a fundamental understanding of the mechanisms limiting T_1.

This chapter is organized as follows: Sec. 4.2 summarizes the experimental techniques utilized for measuring T_1. Sec. 4.3 reports measurements of T_1 on *in situ* Ga ensembles as a function of magnetic field $\vec{B}$ in both Faraday and Voigt geometries. T_1 as long as 480 ms is measured with longer times expected at lower magnetic fields. In Sec. 4.4 we analytically derive an expression for the T_1 dependence on magnetic field and temperature for a single donor, with $T_1 \propto B^{-5}$. The spin-relaxation model is based on spin-orbit (admixture mechanism) and electron-phonon (piezoelectric) coupling for a wurtzite crystal symmetry. In both Faraday and Voigt geometry, remarkable agreement between theory and experiment in the magnitude of T_1 is observed. However the experimental exponent is smaller than expected, with the difference more pronounced in the Voigt geometry. In Sec. 4.5 and Sec. 4.6, we present measurements of the T_1 dependence on the excitation-energy and temperature, respectively, to further investigate this discrepancy. We observe dependence of T_1 on the excitation energy within the inhomogeneous donor-bound exciton line. This variation in T_1 at a single field suggests a secondary relaxation mechanism dependent on donor density. More-

over, the temperature dependence at a given excitation energy is consistent with the expected phonon-occupation model supplemented with an additional excitation-dependent contribution. In Sec. 4.7 we validate that the theoretical model adequately describes implanted In donors as well. Indium implantation at different fluences enables a more straightforward study of the effect of the donor density on T_1, and is presented in Sec. 4.8. This study further strengthens the argument for an additional spin relaxation mechanism dependent on donor density. Sec. 4.9 through Sec. 4.11 address how we can overcome challenges at initializing and optically controlling the spin states at lower fields, and cross out other possible experimental parameter dependencies on excitation power and integration time windows. Finally, section 4.12 concludes with a brief outlook for the ZnO donor system in the context for quantum information applications.

4.2 T_1 measurement

In this work, we study a 360 µm-thick single-crystal ZnO substrate from Tokyo Denpa which is further described in our prior work [54]. The donor concentrations, measured on the back surface, were determined by secondary ion mass spectrometry (SIMS) measurements as $5.3 \cdot 10^{14}\,\mathrm{cm}^{-3}$ for Al and $4.4 \cdot 10^{15}\,\mathrm{cm}^{-3}$ for Ga (App. C.1). The sample is mounted in the cryostat either in Voigt ($\vec{B} \perp \hat{c}$) or Faraday ($\vec{B} \parallel \hat{c}$) geometry. For this chapter, the crystal axis $\hat{c}$ is always parallel to the optical axis $\hat{k}$ (Fig. 4.1(a)). Approximately 10^6 donors of all types are in the optical probing volume.

In the *Voigt geometry* ($\vec{B} \perp \hat{c}$), there are four $\mathrm{D}^0 \leftrightarrow \mathrm{D}^0\mathrm{X}$ transitions: two with horizontal and two with vertical polarization as shown in Fig. 4.1(b). These transitions are labeled as $H_\downarrow \equiv |\downarrow\rangle \leftrightarrow |\Downarrow\uparrow\downarrow\rangle$, $H_\uparrow \equiv |\uparrow\rangle \leftrightarrow |\Uparrow\uparrow\downarrow\rangle$, $V_\downarrow \equiv |\downarrow\rangle \leftrightarrow |\Uparrow\uparrow\downarrow\rangle$, and $V_\uparrow \equiv |\uparrow\rangle \leftrightarrow |\Downarrow\uparrow\downarrow\rangle$ with the subscripts corresponding to the ground spin state of the transition. Prior to measuring the longitudinal spin-relaxation time of the donor ensemble, the spin states are spin-polarized by optical pumping (OP). As shown in Fig. 4.2(a), the spin state is pumped into the $|\uparrow\rangle$ via the $H_\downarrow$ transition. The measurement signal, collected from the $V_\uparrow$ transition, is proportional to the population of the $|\downarrow\rangle$ state. Experimentally, we selectively excite the transition of

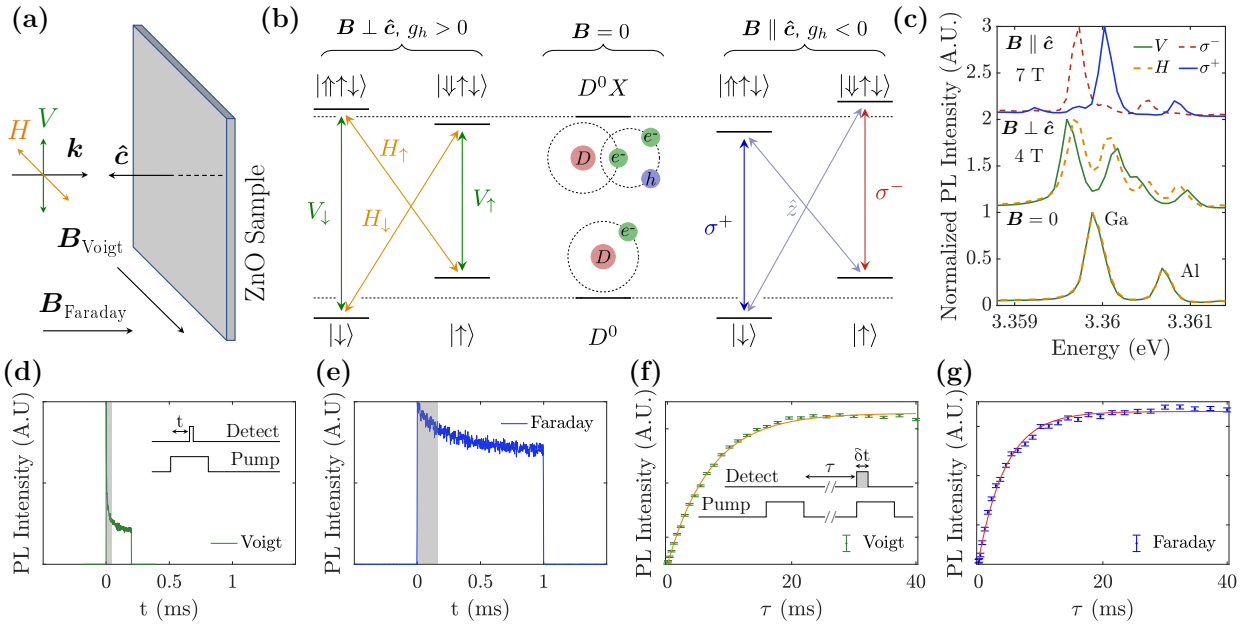

Figure 4.1: (a) Diagram of sample orientation in experimental setup. H and V are the linear polarization axes of a beam with wavevector $\vec{k}$. The beam propagates parallel to the crystal axis $\hat{c}$. The external magnetic field $\vec{B}$ is either parallel ($\vec{B} \parallel \hat{c}$) or perpendicular ($\vec{B} \perp \hat{c}$) to the crystal axis, labeled as Faraday or Voigt geometry, respectively. (b) Energy diagram of the shallow donor system in Voigt geometry (left), no magnetic field (middle) and Faraday geometry (right). We use green-orange colors for Voigt geometry-related figures, and blue-red colors for Faraday geometry-related figures. (c) PL spectra under 3.45 eV excitation in the Faraday geometry (7 T, 1.5 K), in the Voigt geometry (4 T, 5.2 K) and zero field (0 T, 5.2 K). (d) Optical pumping curve in the Voigt geometry, 5.5 T, and 1.5 K. The inset shows the OP laser sequence, (e) OP curve in the Faraday geometry, 5 T, and 1.5 K. (f) Spin-relaxation curve in the Voigt geometry, 5.5 T, and 1.5 K. The inset shows the T_1 measurement scheme. The error bars depict the photon shot noise. (g) T_1 curve in the Faraday geometry, 5 T, and 1.5 K.

interest via polarized resonant excitation. Figure 4.1(d) depicts a typical optical pumping trace in the Voigt geometry.

We measure the spin-relaxation time by fitting the population recovery of the $|\downarrow\rangle$ state as a function of the time delay τ between OP pulses (Fig. 4.1(f) inset). The population of $|\downarrow\rangle$ is proportional to the total counts at the start of the OP trace. The integration window used is shown in gray in Fig. 4.1(d). Population recovery as a function of delay time τ is fit

with an exponential function, as displayed in Fig. 4.1(f).

In the *Faraday geometry* ($\vec{B} \parallel \hat{c}$), there are also four $D^0 \leftrightarrow D^0X$ transitions as shown in Fig. 4.1(b). Two of the transitions are polarized parallel to the optical axis, denoted as $\hat{z}$, and thus cannot be detected. The other two transitions are circularly polarized with $\sigma^+ \equiv |\downarrow\rangle \leftrightarrow |\Uparrow\uparrow\downarrow\rangle$ and $\sigma^- \equiv |\uparrow\rangle \leftrightarrow |\Downarrow\uparrow\downarrow\rangle$. Because the $\hat{z}$-polarized transitions can not be observed, we utilize the ~ 10 times less luminescent two-electron-satellite (TES) transitions D^0 (2s or 2p) $\leftrightarrow D^0X^*$, one and two longitudinal optical (LO) phonon replicas (1LO, 2LO), and the first phonon replica TES transitions (1LO-TES), as a probe of the D^0 population, as depicted in the energy diagram of Fig. 4.2(b) and the spectrum in Fig. 2.4. We will denote these transitions as the sideband transitions.

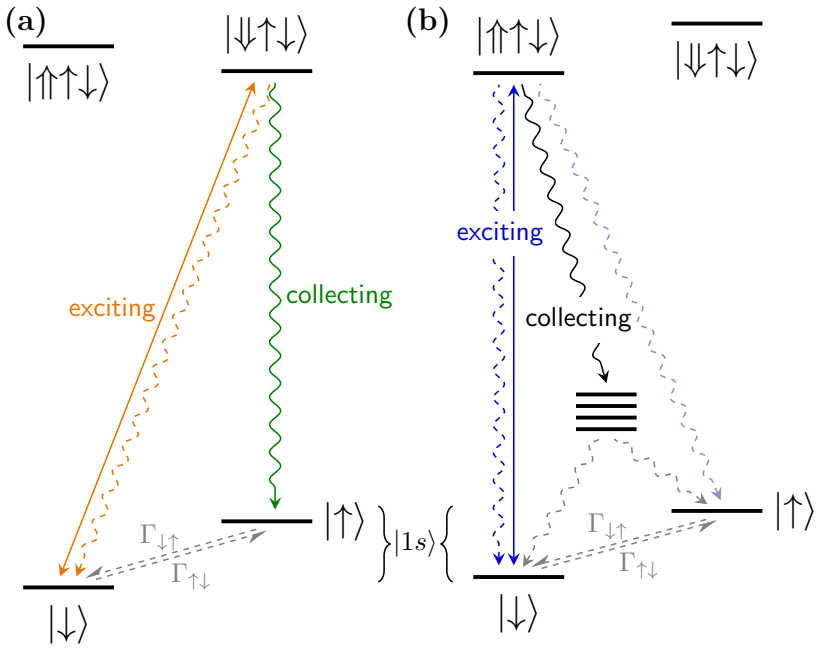

Figure 4.2: Energy diagram for OP and T_1 measurement schemes in the (a) Voigt and (b) Faraday geometry. In (b), the unmarked levels correspond to the energy levels related to the sideband transitions.

The OP and T_1 measurements in Faraday geometry (Figs. 4.1(e) and 4.1(g)) are similar to those in Voigt. In Faraday geometry, the pump-down time is longer compared to Voigt

geometry, because of the ∼50-fold weaker $\hat{z}$ dipole transition [93]. Hence, a longer integration window was utilized.

Overall, we have observed a degradation of OP in both Voigt and Faraday geometries with decreasing magnetic field. We attribute this behaviour to the 84.8 µeV (20.5 GHz) inhomogeneous broadening of the optical transitions, which becomes comparable to the energy difference between the transitions of interest. In the Faraday geometry, the OP contrast is further degraded by collecting the non-resonant sideband transitions and at large fields, due to pump-down times comparable to the spin-relaxation time (Fig. 4.1(e)).

4.3 T_1 dependence on magnetic field

The magnetic field dependence of T_1 at 1.5 K is shown in Fig. 4.3. The minimum magnetic field (2.25 T in the Voigt and 1.75 T in the Faraday geometry) was limited by the increased measurement time and decreased optical pumping contrast at lower fields.

As discussed further in Sec. 4.5, T_1 exhibits a resonant excitation laser energy dependence. To minimize deviations in T_1 due to this dependence, all measurements were taken at the excitation energy where the lowest T_1 was expected. In Faraday geometry, this corresponds to the maximum of the (σ^+) transition. In the Voigt geometry, the energy was chosen to lie between the unresolved $H_\downarrow$ and $V_\downarrow$ transitions.

We observed the longest T_1, 480 ms, at 1.75 T in the Faraday geometry. This is three times higher than the previously reported T_1 [54] where measurements where only performed in Voigt geometry. In Faraday geometry, measurements at lower fields are possible due to larger hole Zeeman splitting and polarization selectivity of the optical transition. We are able to observe optical pumping contrast at fields as low as 0.3 T (Sec. 4.9); however, T_1 measurements were not performed at this field due to the long duty-cycle and low signal contrast. A comparison of the experimental magnetic-field data with theory is made in the next section.

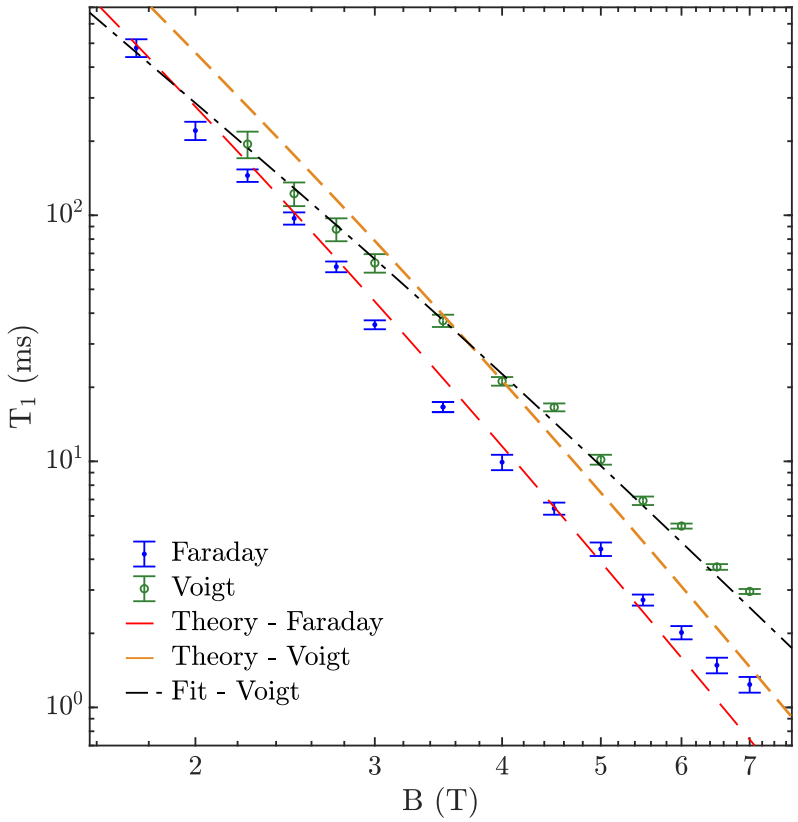

Figure 4.3: T_1 at 1.5 K as a function of external magnetic field. The error bars correspond to one standard deviation of the T_1 fitting error. Theoretical curves are calculated from Eq. 4.12. The curve fitted to the Voigt geometry data was Eq. 4.12, where $\Gamma_{\downarrow\uparrow} = aB^4$, with a single fitted parameter a.

4.4 Theoretical description of T_1 and comparison to experiments

In this section we consider spin-relaxation mechanisms for donor-bound electrons in ZnO and calculate the corresponding T_1. We focus on the spin relaxation mediated by the phonon emission/absorption in the presence of spin-orbit coupling (admixture mechanism), which is the dominant spin-relaxation mechanism for III-V quantum dots [100, 101] and donor-bound electrons in GaAs, InP and CdTe compounds [105]. Due to spin-orbit coupling the spin sublevels of the ground donor state contain an admixture of the excited sublevels with opposite spin projections. As a result, the matrix elements of the spin-independent electron-phonon

interaction between the ground spin sublevels become non-zero resulting in the relaxation of electron spin. The matrix element of this second-order process is given by

$$M_{\downarrow\uparrow} = \sum_e \left[\frac{\langle 1s\downarrow |V_{\rm ph}| e\downarrow\rangle \langle e\downarrow |V_{\rm so}| 1s\uparrow\rangle}{E_{1s\uparrow} - E_{e\downarrow}} + \frac{\langle 1s\downarrow |V_{\rm so}| e\uparrow\rangle \langle e\uparrow |V_{\rm ph}| 1s\uparrow\rangle}{E_{1s\downarrow} - E_{e\uparrow}} \right] . \tag{4.1}$$

Here $|1s\rangle$ is the ground orbital state of the donor-bound electron, $|e\rangle$ denotes the excited orbital states, $E_{1s\uparrow(\downarrow)}$ and $E_{e\uparrow(\downarrow)}$ are the energies of the ground and excited orbital states with $+1/2$ and $-1/2$ spin projections onto magnetic field, $V_{\rm so}$ and $V_{\rm ph}$ are the operators of the spin-orbit and electron-phonon interaction, respectively.

The spin-orbit Hamiltonian for electrons in wurtzite semiconductors contains linear in wave vector $\vec{k}$ terms [106–108]:

$$V_{\rm so} = \alpha(\sigma_x k_y - \sigma_y k_x) , \tag{4.2}$$

where σ_x and σ_y are the Pauli matrices, and α is the constant of spin-orbit coupling. As for the electron-phonon interaction, we consider only piezoelectric interaction with phonons, since it is more efficient at small phonon wave vectors [100, 105]. The corresponding Hamiltonian is

$$V_{\rm ph} = \sqrt{\frac{\hbar}{2\rho\omega_{\vec{q},\alpha}}} \exp\left(\mathrm{i}\vec{q}\cdot\vec{r} - \mathrm{i}\omega_{\vec{q},\alpha}t\right) (eA_{\vec{q},\alpha}) b^\dagger_{\vec{q},\alpha} + \text{c.c.} , \tag{4.3}$$

where

$$A_{\vec{q},\alpha} = \sum_{ijk} \beta_{ijk}\xi_i\xi_j e_k^{(\vec{q},\alpha)} , \tag{4.4}$$

$\vec{q}$ and α denote the phonon wave vector and polarization, ρ is the mass density of the material, $\omega_{\vec{q},\alpha}$ is the phonon frequency, $b^\dagger_{\vec{q},\alpha}$ is the phonon creation operator, $\vec{\xi} = \vec{q}/q$ is the unit vector along the phonon wave vector, $\vec{e}$ is the phonon polarization vector, and β_{ijk} is the piezotensor. The nonzero components of β_{ijk} in wurtzite media are $\beta_{zxx} = \beta_{zyy} = h_{31}$, $\beta_{zzz} = h_{33}$, $\beta_{xxz} = \beta_{xzx} = \beta_{yyz} = \beta_{yzy} = h_{15}$, where h_{31}, h_{33} and h_{15} are piezoelectric constants [109].

In what follows, we use the spherical model for the electronic states of the donor by introducing the averaged electron effective mass m^* and static dielectric constant ε. This

model is supported by the small anisotropy of the electron effective mass and dielectric constant in ZnO [76]. Within the spherical approximation, the donor states can be labeled by electron angular momentum l and its projections, in the same way as in the hydrogen atom. The spin-orbit interaction (4.2) couples the ground $|1s\rangle$ orbital ($l = 0$) and excited $|np\rangle$ orbitals ($l = 1$), where $n = 2, 3 \ldots$. In this section we denote the ZnO c-axis as z. In the Faraday geometry, when $\vec{B} \parallel \hat{z}$, the nonzero matrix elements of $V_{\rm so}$ are $\langle np_+ \downarrow |V_{\rm so}| \, 1s \uparrow\rangle$ and $\langle 1s \downarrow |V_{\rm so}| \, np_- \uparrow\rangle$, where $|p_\pm\rangle = (|p_x\rangle \pm {\rm i} \, |p_y\rangle)/\sqrt{2}$. Keeping in mind that the splittings between spin and orbital sublevels induced by magnetic field are much smaller than the energy distance to excited states, as well the relations between the matrix elements $\langle np_+ \downarrow |V_{\rm so}| \, 1s \uparrow\rangle = -\langle 1s \downarrow |V_{\rm so}| \, np_- \uparrow\rangle$, and $\langle 1s \, |V_{\rm ph}| \, np_+\rangle = \langle np_- \, |V_{\rm ph}| \, 1s\rangle$, the spin-flip matrix element (4.1) is simplified to

$$M_{\downarrow\uparrow}(\vec{B} \parallel \hat{z}) = (\hbar\omega_c - 2g\mu_B B) \times \sum_n \frac{\langle 1s \downarrow |V_{\rm ph}| \, np_+ \downarrow\rangle \, \langle np_+ \downarrow |V_{\rm so}| \, 1s \uparrow\rangle}{(E_{1s} - E_{np})^2} \, . \qquad (4.5)$$

Here E_{1s} and E_{np} are the energies of $1s$ and $np_\pm$ orbitals at zero magnetic field, g is the electron g-factor, μ_B is the Bohr magneton, and $\omega_c = |e|B/(m^*c)$ is the cyclotron frequency. In the derivation of Eq. (4.5), we took into account the splitting $g\mu_B B$ between the spin sublevels of $1s$ and np-orbitals, as well as the splitting $\hbar\omega_c$ between the np_+ and np_- orbital sublevels.

In the Voigt geometry, $\vec{B} \parallel \hat{x}$, the nonzero matrix elements of $V_{\rm so}$ between the states with opposite spin projections are $\langle np_x \downarrow |V_{\rm so}| \, 1s \uparrow\rangle$ and $\langle 1s \downarrow |V_{\rm so}| \, np_x \uparrow\rangle$. Note that here $\uparrow$ ($\downarrow$) denote the spin projections onto the x-axis. Using the same arguments as in the derivation of Eq. (4.5), we obtain

$$M_{\downarrow\uparrow}(\vec{B} \parallel \hat{x}) = -2g\mu_B B \times \sum_n \frac{\langle 1s \downarrow |V_{\rm ph}| \, np_x \downarrow\rangle \, \langle np_x \downarrow |V_{\rm so}| \, 1s \uparrow\rangle}{(E_{1s} - E_{np})^2} \, . \qquad (4.6)$$

In what follows we use the long-wave approximation (LWA) for phonons: $qa_0 \ll 1$, where $q = g\mu_B B/(\hbar s)$, s is the sound velocity, and a_0 is the Bohr radius of a donor. This approximation is valid in the whole range of experimentally studied magnetic fields due to a small Bohr radius of shallow donors in ZnO, $a_0 \approx 1.5$ nm [76]. Using LWA, the relation

$\left\langle np\left|\vec{k}\right|1s\right\rangle = \mathrm{i}m^*(E_{np}-E_{1s})\left\langle np\left|\vec{r}\right|1s\right\rangle/\hbar^2$, and the procedure described in Ref. [100], the matrix elements (4.5) and (4.6) are simplified to

$$\begin{aligned} M_{\downarrow\uparrow}(\vec{B}\parallel\hat{z}) &= (2g\mu_B B-\hbar\omega_c)\frac{\alpha m^*\beta(\mathcal{E}_x+\mathrm{i}\mathcal{E}_y)}{2e\hbar^2}\,, \\ M_{\downarrow\uparrow}(\vec{B}\parallel\hat{x}) &= g\mu_B B\frac{\alpha m^*\beta\mathcal{E}_x}{e\hbar^2}\,. \end{aligned} \tag{4.7}$$

Here $\vec{\mathcal{E}}=-\mathrm{i}\,\vec{q}V_{\mathrm{ph}}(\vec{r}=0)/e$ is the electric field induced by a phonon at the location of the donor, and

$$\beta = 2e^2\sum_n \frac{\langle 1s\left|x\right|np_x\rangle^2}{E_{np}-E_{1s}} \tag{4.8}$$

is the donor polarizability for electric field lying in the (xy)-plane. In the spherical approximation that we use, the polarizability is found analytically [110]: $\beta = 9\varepsilon a_0^3/2$. This expression omits the impurity's short-range chemical potential, which is addressed in Sec. 7.2.

The spin-flip transition rates are found using Fermi's golden rule, e.g., for the transition from $|1s\uparrow\rangle$ to $|1s\downarrow\rangle$ with emission of a phonon:

$$\Gamma_{\downarrow\uparrow} = \frac{2\pi}{\hbar}\sum_{\vec{q},\alpha}|M_{\downarrow\uparrow}|^2\,\delta(\hbar q s_\alpha - g\mu_B B)\,. \tag{4.9}$$

Accurate averaging over $\vec{q}$ direction in Eq. (4.9) is difficult due to the complicated phonon structure in wurtzite crystals. However simplified estimations can be made within the model of the effective isotropic elastic medium, when the longitudinal and transverse phonons are decoupled and propagate with isotropic sound velocities s_l and s_t [109]. This approximations seems reasonable since the relations $c_{11}\approx c_{33}$, $c_{12}\approx c_{13}$ and $c_{44}\approx(c_{11}-c_{12})/2$ hold for the elastic moduli values in ZnO [111]. The summation in Eq. (4.9) is then performed for a longitudinal mode with $\vec{e}^{\,(\vec{q},l)}=\vec{\xi}$ and two transverse modes with $\vec{e}^{\,(\vec{q},t)}\perp\vec{\xi}$. Averaging over $\vec{\xi}$ direction for transverse phonons is done with the use of the formula $\langle e_i^{(\vec{q},t)}e_j^{(\vec{q},t)}\rangle = (\delta_{ij}-\xi_i\xi_j)/2$. By substituting the matrix elements (4.7) in Eq. (4.9) and performing the summation, we obtain

$$\Gamma_{\downarrow\uparrow}(\vec{B}\parallel\hat{z}) = \frac{\Lambda\Delta_1^3\Delta_2^2}{\hbar E_{1s}^4}\,,\qquad \Gamma_{\downarrow\uparrow}(\vec{B}\parallel\hat{x}) = \frac{\Lambda\Delta_1^5}{2\hbar E_{1s}^4}\,, \tag{4.10}$$

where

$$\Lambda = \frac{9(e\alpha)^2}{448\pi\rho\hbar^3}\left(\frac{5h_{33}^2+8h_{31}^2+32h_{15}^2}{5s_l^5} + \frac{4h_{33}^2+4h_{31}^2+52h_{15}^2}{5s_t^5}\right), \tag{4.11}$$

$\Delta_1 = g\mu_B B$, and $\Delta_2 = \Delta_1 - \hbar\omega_c/2$. Calculation based on Eqs. (4.10) and (4.11) using parameters listed in Tab. 4.1 yields $\Lambda \approx 0.02$, $\Gamma_{\downarrow\uparrow}(\vec{B} \parallel \hat{z})/B^5 \approx 0.08$ $\mathrm{s^{-1}T^{-5}}$, and $\Gamma_{\downarrow\uparrow}(\vec{B} \parallel \hat{x})/B^5 \approx 0.04$ $\mathrm{s^{-1}T^{-5}}$.

Parameter	Value	Reference
ρ (kg/m^3)	5.6×10^3	
m^*/m_0	0.25	[76]
ε	8.1	[76]
α (meV Å)	1.1	[108]
g	2	[54]
h_{33} (V/m)	1.5×10^{10}	[111]
h_{31} (V/m)	-0.6×10^{10}	[111]
h_{15} (V/m)	-0.6×10^{10}	[111]
s_l (m/s)	6.1×10^3	[111]
s_t (m/s)	2.9×10^3	[111]

Table 4.1: Parameters of ZnO used in calculations of T_1. The piezoelectric constants are calculated using the values of piezoelectric stress moduli e_{ij} as $h_{ij} = e_{ij}/(\varepsilon\varepsilon_0)$, where ε is the static dielectric constant, and ε_0 is the vacuum permittivity. the electron effective mass and dielectric constant are calculated as $3/m^* = 1/m_{e\parallel} + 2/m_{e\perp}$, $3/\varepsilon = 1/\varepsilon_\parallel + 2/\varepsilon_\perp$, the sound velocities $s_l = \sqrt{c_{11}/\rho}$, $s_t = \sqrt{c_{44}/\rho}$.

The measured spin-relaxation time T_1 at nonzero temperature is $T_1 = 1/[\Gamma_{\downarrow\uparrow}(T)+\Gamma_{\uparrow\downarrow}(T)]$, where $\Gamma_{\downarrow\uparrow}(T) = \Gamma_{\downarrow\uparrow}[N_{\mathrm{ph}}(T)+1]$, $\Gamma_{\uparrow\downarrow}(T) = \Gamma_{\downarrow\uparrow}N_{\mathrm{ph}}(T)$, and $N_{\mathrm{ph}}(T)$ is the phonon occupation number. With that we find

$$T_1 = \frac{\mathrm{e}^\gamma - 1}{\Gamma_{\downarrow\uparrow}(\mathrm{e}^\gamma + 1)}, \tag{4.12}$$

where $\gamma = g\mu_\mathrm{B}B/k_\mathrm{B}T$ and $k_\mathrm{B}T$ is the thermal energy.

We note that the simple model used here to calculate donor electronic states does not take into account the anisotropy of the electron effective mass and the presence of a short-range impurity potential [76]. These effects result in a small shift of E_{1s} [76] and consequently slightly affect the T_1 value through the denominator in Eq. (4.10). However, we neglect these small corrections in order to keep our model simple. We also note, that the spin-flip rate (4.10) is quite universal, since it does not depend on the electron effective mass, as the E_{1s} value can be taken from experiment. Also, other mechanisms of electron-phonon interaction, such as deformation potential and direct spin-phonon interaction are less efficient at small phonon wave vectors, result in smaller spin-flip rates and $T_1 \propto B^{-7}$ dependence not observed in the experiment [105].

Figure 4.3 includes the theoretically expected T_1 curves. The theoretical T_1 curves include no fit parameters and lie remarkably close to the experimental values. The calculated T_1 values are sensitive to the values of the piezoelectric constants, which have quite a wide spread in the literature. This spread may result in ∼2-times change of the calculated T_1 which still gives a good agreement with experiment. Additionally, through much of the experimental range of magnetic fields, the expected relationship $T_1(\vec{B} \parallel \hat{x}) \approx 2T_1(\vec{B} \parallel \hat{z})$ is approximately observed. However, the experimental exponential dependence deviates from the expected B^{-5} (Eqs. 4.10 and 4.12). Specifically, in the Faraday geometry, a softening of the exponent is observed at higher fields; while, in the Voigt geometry, a B^{-4} dependence is observed across the full experimental range of magnetic fields (as shown in Fig. 4.3). If we extrapolate T_1 to lower fields, we may expect a cross-over between Faraday and Voigt geometry T_1 to occur for fields below 2 T. This discrepancy suggests that while spin-orbit coupling is the dominant relaxation mechanism for donor-bound electrons in ZnO, there is an additional mechanism.

4.5 Excitation energy dependence

T_1 at a fixed magnetic field and temperature was found to depend on the optical pumping excitation energy. Figures 4.4(a,b) show the photoluminescence excitation (PLE) spectra

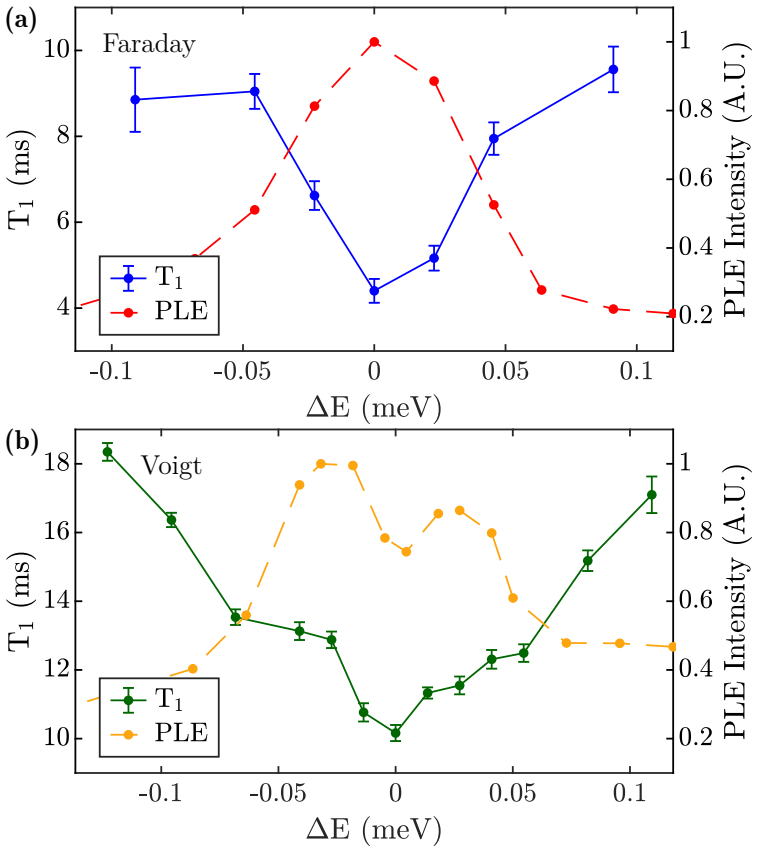

Figure 4.4: T_1 and PLE at 5 T and 1.5 K for varying excitation energy detuning ΔE in (a) Faraday and (b) Voigt geometry. The error bars correspond to one standard deviation of the T_1 fitting error.

(dashed curves) and T_1 (solid curves) in Voigt and Faraday geometry at 5 T and 1.5 K. The PLE spectra were taken by tuning the excitation laser over the $H_\downarrow$ and σ^+ transitions respectively, while collecting the sideband transitions. In Faraday geometry, we observe the expected PLE peak. T_1 reaches a minimum value near the maximum of the PLE. In Voigt geometry, two peaks are observed. The low energy peak corresponds to resonant excitation of the $H_\downarrow$ transition (Fig. 4.1(b)). The high energy peak corresponds to the resonant excitation of the $V_\downarrow$ transition. The observation of the high energy peak indicates either a relaxation of the polarization selection rules or an impure polarization excitation. In Voigt geometry, the spin-relaxation time reaches a minimum in between the two peaks.

A dependence on the pump laser excitation energy for T_1 is not expected for an isolated donor, as the excitation pulse is only used for spin initialization and the relaxation process occurs while the excitation pulse is off. Laser leakage through the acousto-optic modulator (AOM) could result in optical pumping during the spin recovery period which would be more efficient on-resonance if the resonance line is homogeneously broadened. This potential cause of a reduced T_1 on-resonance can be ruled out due to the high AOM extinction ratio ($> 10^4$) compared to the spin-relaxation time to pump-down time ratio, the similar pump-down time observed over all detunings (suggesting an inhomogeneous broadened resonance line), and no observed softening of the exponent or T_1 saturation [46] at the measured fields below 3T with longer T_1 (Fig 4.3). For measuring T_1 further from resonance, increasingly longer pump-on times and varying integration window times were used to fully initialize the system. In control measurements, we find that pump-power, pump-on time (Sec. 4.10) and integration window (Sec. 4.11) do not significantly affect T_1 .

We further investigate the size of the energy dependence of T_1 as a function of field. Figure 4.5 depicts the change of the excitation energy dependence with varying magnetic field in the Faraday geometry. We observe that the T_1 variation does not exceed a factor of 1.25 for low fields (3 T), but can vary by more than a factor of two at higher fields (5 T, 7 T). Hence, the choice of excitation energy can impact the magnetic field dependence shown in Fig. 4.3. For Faraday geometry, the magnetic field dependence deviates from the theoretically predicted behavior at the higher fields ($B \geq 5$ T) where the energy-dependent deviation is largest. However, we note that the softening of the exponent at high fields would be even greater if the magnetic-field dependence had been measured in the off-resonance condition.

The higher spin relaxation at larger D^0X intensity (indicating higher donor density) suggests an additional relaxation mechanism based on donor-donor interactions. The origin of this relaxation mechanism is unknown at this time. We can rule out exchange and dipolar donor-donor interactions. The Bohr radius of the electron donor can be estimated to be $\sim$1.5 nm [76]. Donor densities on the order of $10^{16}\,\mathrm{cm}^{-3}$ yield an average distance between donors of $\sim$30 nm, meaning that exchange interactions would have little to no effect on the the

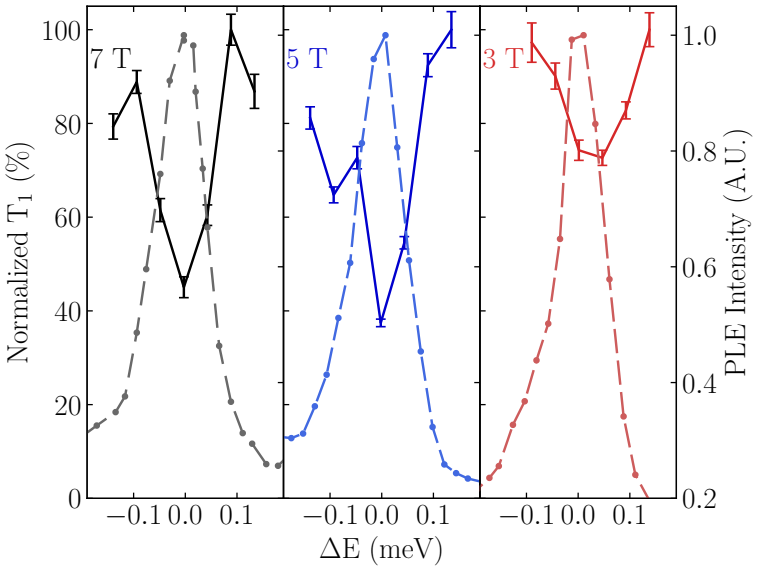

Figure 4.5: Normalized T_1 measurements at 1.8 K, with varying field, and excitation energy in the Faraday geometry (solid line, left axis) and the corresponding PLE spectra (dashed line, right axis). The measurements were taken on a different spot on the sample than the ones on Fig. 4.4(a). The error bars correspond to one standard deviation of the T_1 fitting error. The maximum T_1 observed are 1.55 ms, 6.69 ms, 53.6 ms for 7 T, 5 T, and 3 T respectively, and are equivalent to 100% of the normalized T_1.

ensemble longitudinal spin-relaxation process. Dipolar interaction on the other hand would yield a flip-flop rate of approximately 10 - 1000 Hz, comparable to the the experimentally observed relaxation rate. However, the hyperfine interaction of the donor with the lattice ^{67}Zn induces inhomogeneity of tens of MHz in the Zeeman energies [54]. Due to energy conservation, this hyperfine interaction should effectively block dipolar donor-donor flip-flops in the absence of an additional energy-conserving mechanism.

4.6 Temperature dependence

The temperature dependence of T_1 at 5 T is shown in Fig. 4.6. The measurements were taken in the two magnetic field orientations and at two excitation energies which we label “on-resonance" and “off-resonance". The on-resonant measurements are performed at the wavelength near the minimum T_1. For the off-resonant measurements, we excite 44 µeV

(10.6 GHz) and 118 µeV (28.5 GHz) negatively detuned from the resonance condition for the Faraday and Voigt geometries, respectively. At 1.5 K, T_1 values between the two excitation resonance conditions differ by approximately a factor of 2. At high temperatures ($T > 10$ K), the on- and off-resonance relaxation times converge.

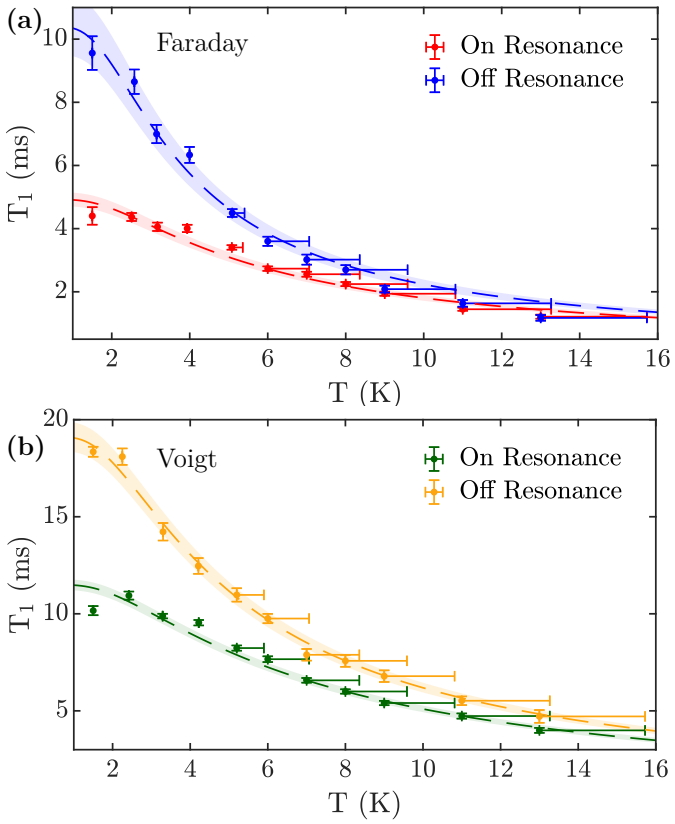

Figure 4.6: Spin-relaxation time as a function of temperature at $B = 5$ T. The error bars in T_1 correspond to one standard deviation of the T_1 fitting error. The increasing uncertainty in temperature rises from a systematic underestimation of the temperature due to the distance and lack of thermal contact between the temperature sensor and the sample. The dashed lines are least-square fits to the function $(\Gamma_{\downarrow\uparrow} F_{\mathrm{ph}}(T) + \Gamma_0)^{-1}$. The shaded areas around each fit depict the model function with $\Gamma_{\downarrow\uparrow} = \Gamma_{\downarrow\uparrow,\mathrm{fit}} \pm \Gamma_{\downarrow\uparrow,\mathrm{fit,err}}$. (a) Faraday, $\Gamma_{\downarrow\uparrow} = 0.1647 \pm 0.0091\,\mathrm{ms}^{-1}$, $\Gamma_{0,\mathrm{on}} = 0.0386 \pm 0.0144\,\mathrm{ms}^{-1}$, $\Gamma_{0,\mathrm{off}} = -0.0685 \pm 0.0108\,\mathrm{ms}^{-1}$ and (b) Voigt, $\Gamma_{\downarrow\uparrow} = 0.0512 \pm 0.0021\,\mathrm{ms}^{-1}$, $\Gamma_{0,\mathrm{on}} = 0.0357 \pm 0.0035\,\mathrm{ms}^{-1}$, $\Gamma_{0,\mathrm{off}} = 0.0011 \pm 0.0027\,\mathrm{ms}^{-1}$.

We are able to obtain reasonable agreement to a simple relaxation model in which the total spin relaxation is proportional to a sum of a phonon-dependent and a constant term;

$(T_1)^{-1} = \Gamma_{\downarrow\uparrow} F_{\mathrm{ph}}(T) + \Gamma_0$, with phonon factor $F_{\mathrm{ph}}(T) = 2N_{\mathrm{ph}}(T) + 1$ (compare with Eq. 4.12). The fit was performed with a common $\Gamma_{\downarrow\uparrow}$ for both on- and off-resonance datasets, and different $\Gamma_{0,\mathrm{on}}$ and $\Gamma_{0,\mathrm{off}}$.

As shown in Fig. 4.6, this simple temperature dependence model describes both on- and off-resonance datasets. In both geometries we find a significantly larger Γ_0 for on-resonance than off-resonance, consistent with the excitation energy dependence. In the Faraday off-resonance case, the fit in fact produces a negative Γ_0, indicating that the additional relaxation mechanism cannot solely be explained by a simple constant. This could indicate a suppression of the phonon-induced spin-relaxation rate when detuned from the ensemble resonance, however the simplicity of the model (which does not include a temperature dependence for Γ_0 or the effect of temperature on the homogeneous exciton linewidth) prevents a firm conclusion. Thus, the origin of the additional relaxation (or stabilization) mechanism is a subject for future study.

4.7 Comparison of T_1 between donor species

Originally published in part in [81]: X. Wang, C. Zimmermann, M. Titze, V. Niaouris, E. R. Hansen, S. H. D'Ambrosia, L. Vines, E. S. Bielejec, and K.-M. C. Fu, "Properties of Donor Qubits in ZnO Formed by Indium-Ion Implantation", Phys. Rev. Appl. **19**, 054090 (2023).

Reprinted with permission from APS.

In Sec. 4.4, we presented a species-agnostic model for the spin relaxation time of shallow donors in ZnO. We found that the spin relaxation time of *in situ* Ga donors adequately follows the theoretically predicted dependence on magnetic field. Since the relaxation rate prefactor a ($\Gamma_{\downarrow\uparrow} = aB^5$) is inversely dependent on the fourth power of the donor binding energy and proportional to the fifth power of the electron g-factor (Eq. 4.10), we expect even longer T_1 for deeper donors, such as In. In a follow-up study, we implanted a separate TD substrate (sample B) with In via ion implantation with a mean depth of 200 nm with

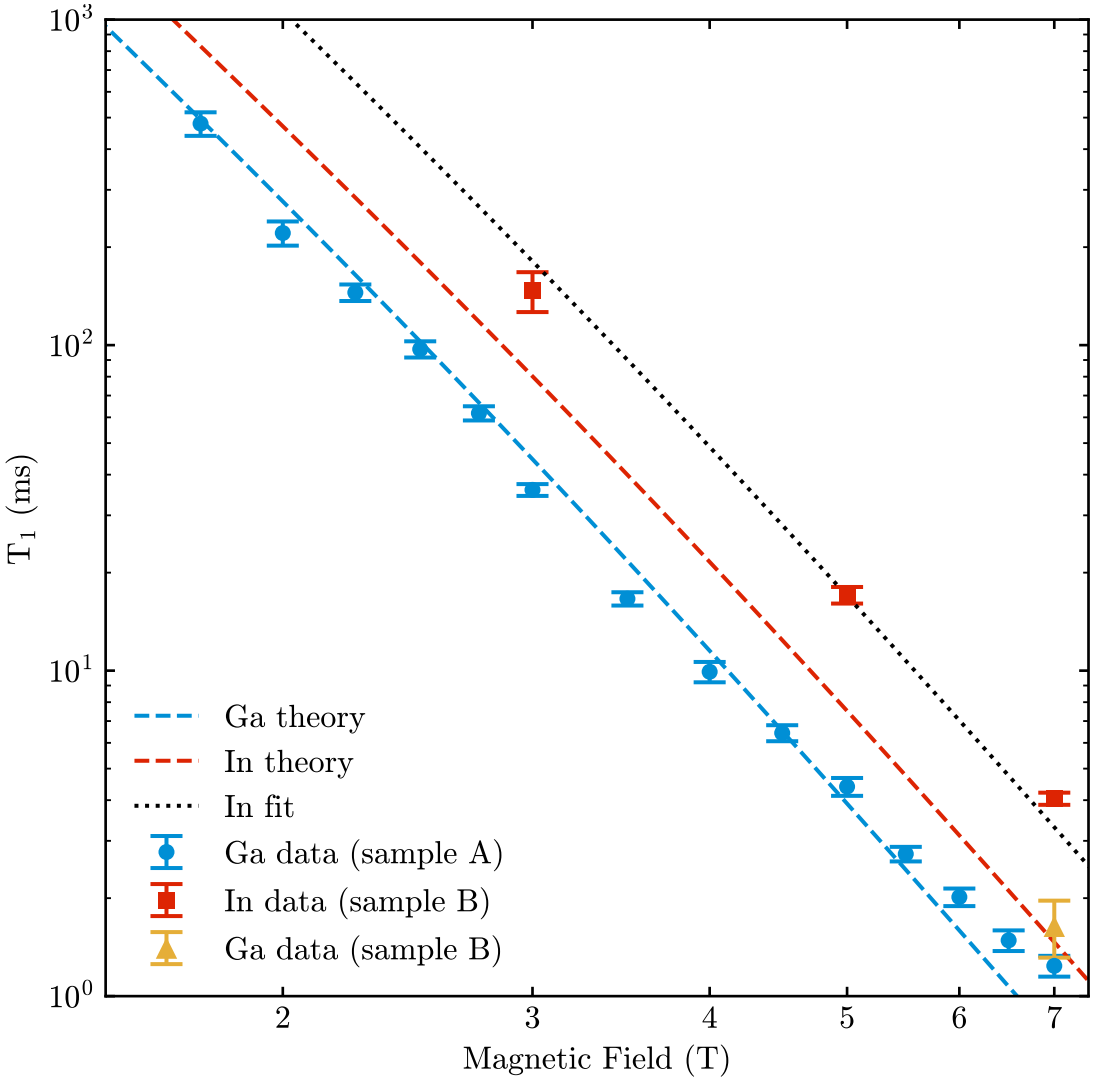

Figure 4.7: Dependence of T_1 on the applied magnetic field for *in situ* Ga and implanted In donors in samples A and B. Sample A refers to the same sample as in Sec. 4.3, and the sample A Ga data are the same as in Fig. 4.3. Sample B refers to the In implanted sample. The dashed lines represent the theoretically expected dependence for Ga (blue) and In (red). The dotted line represents a fitted curve with a single parameter $a = 0.018\,\mathrm{s}^{-1}\,\mathrm{T}^{-5}$ for $\Gamma_{\downarrow\uparrow} = aB^5$. Faraday geometry ($\vec{B} \parallel \hat{c}$), $T = 1.5$ K (for sample A), 1.9 K (for sample B).

varying fluence at different sample locations. Fig. 4.7 shows the dependence of T_1 on B in the Faraday geometry at 1.9 K for *in situ* Ga and implanted In in sample B and compares it to the 1.5 K magnetic field dependence of Fig. 4.3. Theoretically, taking into account

the different binding energy and g factor of In donors we expect that the spin relaxation rate of In will be half of Ga ($a_{\text{theory,Faraday,In}} = 0.04\,\text{s}^{-1}\,\text{T}^{-5}$). Even though the data suggest that In follows the same magnetic field dependence as Ga, the experimentally measured prefactor is $0.018\,\text{s}^{-1}\,\text{T}^{-5}$, four times smaller than the Ga prefactor. A small dependence of T_1 on implantation fluence and excitation photon energy is also observed (Sec. 4.8), which is consistent with the dependence of T_1 on excitation photon energy observed in Ga (Sec. 4.5). These results indicate the longitudinal spin relaxation mechanism is identical for both types of donors, with no degradation observed for In due to residual implantation damage, The difference in theoretically vs experimentally observed prefactors could potentially be due to the effect the donor density has on spin relaxation.

4.8 Dependence of T_1 on donor density

Originally published in part in the Supplemental Material of [81]: X. Wang, C. Zimmermann, M. Titze, V. Niaouris, E. R. Hansen, S. H. D'Ambrosia, L. Vines, E. S. Bielejec, and K.-M. C. Fu, "Properties of Donor Qubits in ZnO Formed by Indium-Ion Implantation", Phys. Rev. Appl. **19**, 054090 (2023).

Reprinted with permission from APS.

In Sec. 4.5, we demonstrated an excitation-energy dependence that was attributed to varying effective donor density at a given resonant (or near-resonant) excitation energy. To directly investigate the donor density dependence of T_1 we measure T_1 in sample B, a TD substrate that has been implanted with In via ion implantation with a mean depth of 200 nm with varying fluences at different sample locations. In Fig. 4.8a we show that for a given In fluence of $\sim 1.3 \times 10^{11}\,\text{cm}^{-2}$, T_1 varies with excitation energy, the same as what was observed with Ga donors. A shorter longitudinal spin relaxation time is observed when probed on resonance with the ensemble implanted In donors, indicating that a higher density of the probed sub-ensemble shortens the measured longitudinal spin relaxation time. Figure 4.8b depicts the dependence of T_1 on the a implantation fluence. At higher implantation fluences,

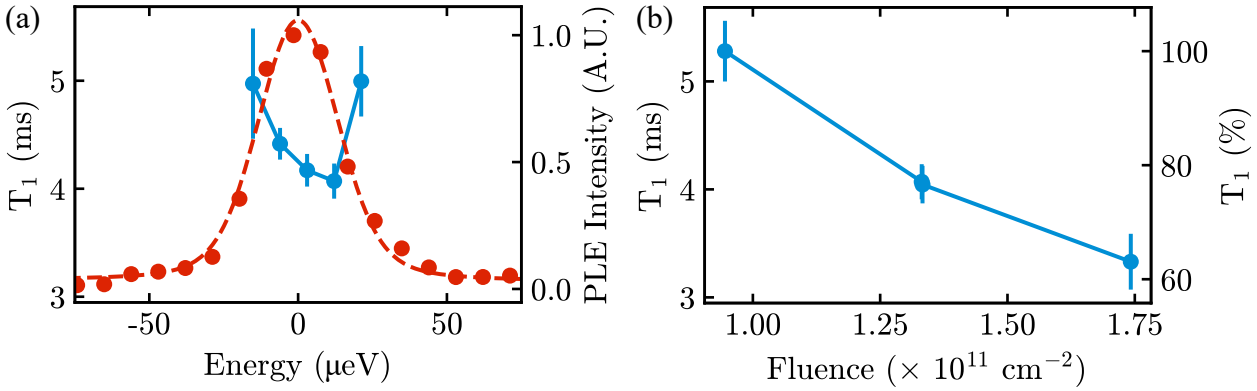

Figure 4.8: Faraday geometry, $B = 7\,\mathrm{T}$ and $T = 1.9\,\mathrm{K}$. Error bars on T_1 correspond to one standard deviation error. (a) Longitudinal spin relaxation time T_1 of In as a function of excitation photon energy (blue points, left y-axis) and PLE spectrum (red points, right y-axis) for an implantation fluence of $\sim 1.3 \times 10^{11}\,\mathrm{cm}^{-2}$. PLE data are fitted with a Voigt profile (red dotted line). Pump pulse resonant with $|\downarrow\rangle \leftrightarrow |\Uparrow\downarrow\uparrow\rangle$. (b) T_1 as a function of the In implantation fluence.

the longitudinal spin relaxation time becomes shorter, which agrees qualitatively with our explanation for the effective donor-density dependence of T_1.

4.9 Low magnetic field optical pumping

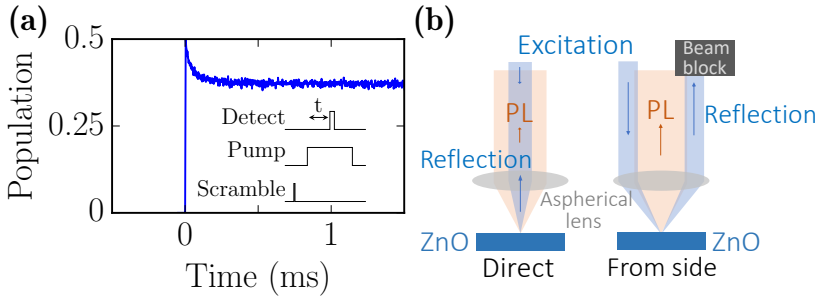

Figure 4.9: (a) Optical pumping of electrons from the $|\downarrow\rangle$ state to the $|\uparrow\rangle$ state (exciting the σ^+ transition) in Faraday geometry, 0.3 T, 1.5 K . A scrambling pulse is used to initialize both neutral donor electron states to 50 %. (b) Optical paths of the excitation beam and emitted photoluminescence in the side-excitation scheme.

In Sec. 4.2, we discussed two ways to verify optical pumping. In the Faraday geometry at low field, the optical pumping contrast becomes too low to be detected via the sideband transitions due to laser background in the corresponding collection energy region. Instead, the excitation laser beam was offset on the focusing lens. This side-excitation scheme allows for the reflected excitation beam and the emitted photoluminescence to be spatially filtered as depicted in Fig. 4.9(b) and resonant photoluminescence to be collected.

Figure 4.9(a) depicts an optical pumping trace at 0.3 T. At such low magnetic fields, T_1 is expected to be very long and hence the wait time between pump-on pulses would deem the experiment very slow. To speed up the measurement, we utilize a short scrambling pulse at 3.45 eV to initialize the two D^0 electron spin states to 50 %.

4.10 Dependence of T_1 on pump-on time and excitation power

For measuring T_1 as a function of the excitation energy (Sec. 4.5), the pump-on time was varied to achieve initialization of the ground-state spins (Sec. 4.2). It is possible that the observed excitation energy dependence of T_1 (Sec. 4.5) might be due to a variation in pump-on time. Additionally, while the nominal excitation power was kept constant during these measurements, it is interesting to test whether T_1 displays a dependence on excitation power in order to understand limiting factors for T_1. Thus, we performed experiments to gauge the influence of different pump-on times and nominal excitation powers on T_1. Performing such experiments similar to the approach presented in Sec. 4.2 is challenging, for example, because at very high excitation powers it is not possible to detect the start population due to very fast optical pumping. This problem can be mitigated by conducting the experiment using two lasers (pump-probe experiment).

In Faraday geometry, the pump laser will be set resonant with the σ^+ transition of a specific sub-ensemble, and for this sub-ensemble, the $|\downarrow\rangle$ population is transferred to the $|\uparrow\rangle$ population. The specific amount of population that is transferred depends on the pump-on time and/or excitation power of the pump laser. After a delay time τ, the probe laser, resonant with the σ^- transition of the sub-ensemble, probes the remaining $|\uparrow\rangle$ population

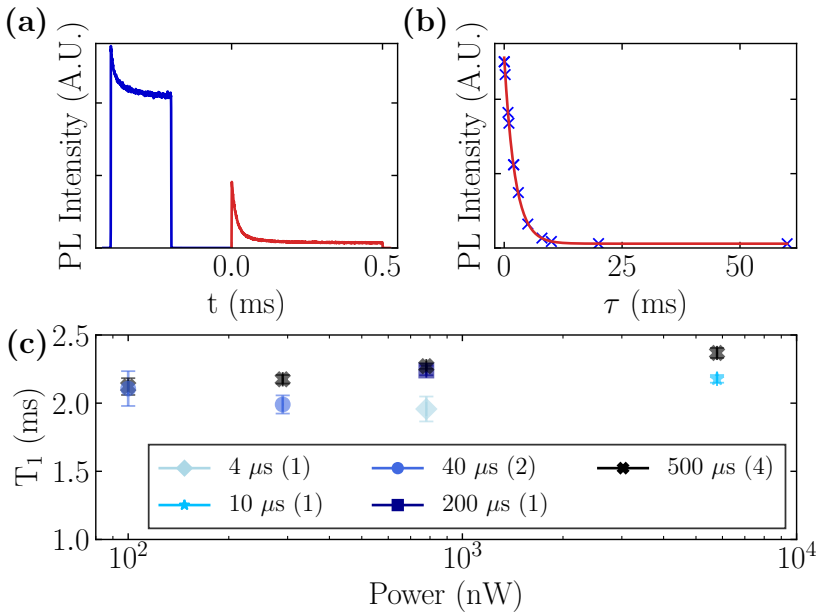

Figure 4.10: (a) Optical pumping curve using a pump and a probe laser in the Faraday geometry at 5 T and 1.9 K. The excitation energy was chosen to be close to the maximum of the ensemble resonance. The inset shows the color-coded spectral position of the pump and probe levels in the energy level diagram. (b) Spin-relaxation trace in the same condition. The red curve is the fit curve from which we extract T_1. The inset shows the OP and T_1 pump-probe measurement schemes. The integration window used is highlighted with gray color both in the inset and in (a). (c) T_1 pump-probe measurements conducted with various pump excitation powers and pump-on times (with constant probe conditions). The horizontal axis depicts the pump powers, while the shape and shade of each point represent the pump-on time. The number of points of each color is displayed between parentheses in the legend.

(Fig. 4.10(a)). Plotting this population as a function of τ can be used to obtain T_1. We then measure T_1 while tuning the pump parameters, allowing the T_1 dependence on pump-on time and excitation power to be measured without varying the probing conditions (Fig. 4.10(b)).

As shown in Fig. 4.10(c), T_1 does not vary more than a factor of 1.2 in dependence on excitation power and/or pump-on time. Thus, it is unlikely that the specific parameters chosen for the T_1 measurements have a significant influence on the measured value for T_1. In Fig. 4.10(c), the data points with a pump-on time of 500 µs resemble closest the conditions used in the main text for determining T_1 because complete spin initialization has been

achieved.

4.11 Dependence of T_1 on optical pumping integration time

When measuring T_1 via optical pumping, we observe different pump-down time for different experimental conditions. Since the goal is to only collect signal from the beginning of the pump-down trace, which is proportional to the population of the state of interest, we need to integrate the signal in the smallest possible time window. However, the smaller the integration window (or gate-on time), the less signal we collect, leading to unsatisfactory statistics. In order to balance the two effects, we choose different gate-on times for each measurement in the main text.

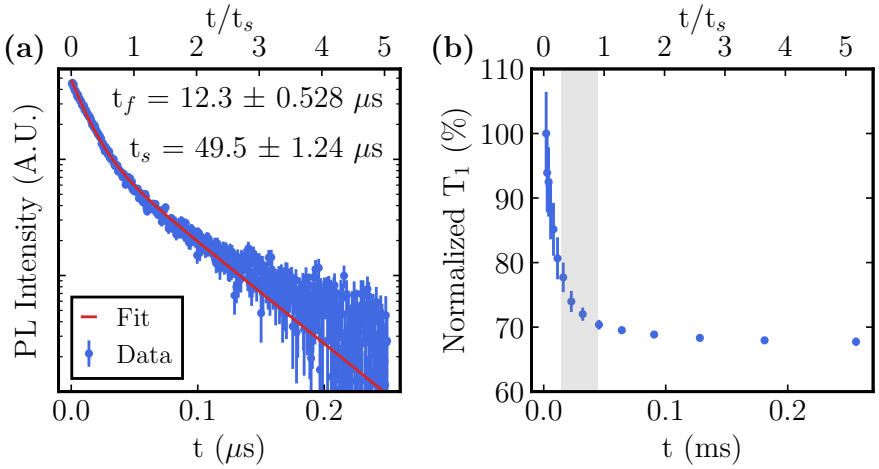

Figure 4.11: (a) Optical pumping trace using a pump and a probe laser in the Faraday geometry at 5 T and 1.9 K, fit with a double exponential model, with fast and slow decays of t_{f} and t_{s} respectively. The y-axis is in logarithmic scale. (b) Normalized T_1 from a single pump-probe experiment, as a function of the window integration time. The gray area depicts the the experimental choices on gate-on time, $0.3\times t_{\mathrm{s}}$ to $0.9\times t_{\mathrm{s}}$.

As shown in Fig. 4.11(a), the OP curve can be sufficiently described by a double exponential decay model. The fast decay time of the OP is roughly up to one order of magnitude shorter than the slow decay time. For the excitation energy dependence experiments, the gate-on time remained between 0.3 to 0.9 times the slow component of the OP curves. To

investigate the effect of choosing such a wide range of gate-on times we utilize a two laser pump-probe experiment (Sec. 4.10). Fig. 4.11(b) shows the normalized T_1 as a function of gate-on time normalized to the slow decay time. We observe that for normalized gate-on times of 0.3 and 0.9 the variation of T_1 is negligible ($\sim$8 %). It is interesting to note that for much smaller normalized integration windows, T_1 can vary as much as 20 %. However, we do not probe such short gate-on times due to the low count rate. Overall, we conclude that the integration window choice does not significantly change the observed T_1 for all experimental data.

4.12 Concluding remarks

In summary we have demonstrated long longitudinal relaxations times of up to 480 ms for shallow donors in ZnO. The measured T_1 is approximately three orders of magnitude longer than prior work in other direct band gap materials (GaAs, CdTe and InP [105]) and stems directly from ZnO's small spin-orbit coupling. Quantitatively we find good agreement of the experimental results with a single-phonon relaxation mechanism. The small longitudinal spin relaxation supports the promise of donors in direct band-gap II-VI semiconductors in which isotope purification is possible to enable long spin coherence times.

Chapter 5

OPTICAL LINEWIDTH CONTRIBUTIONS OF DONOR ENSEMBLES

Originally published as [97]: V. Niaouris, S. H. D'Ambrosia, C. Zimmermann, X. Wang, E. R. Hansen, M. Titze, E. S. Bielejec, and K.-M. C. Fu, "Contributions to the optical linewidth of shallow donor-bound excitonic transition in ZnO", Optica Quantum **2**, 7–13 (2024).

Essential optical parameters which impact the spin-photon interface include radiative lifetime, optical inhomogeneous and homogeneous linewidth and optical depth. In this chapter we study the donor-bound exciton optical linewidth properties of *in situ* Al, Ga, and In as well as implanted In donors. The ensemble photoluminescence linewidth ranges from 4-11 GHz, less than two orders of magnitude larger than the expected lifetime-limited linewidth. The ensemble linewidth remains narrow in absorption through samples with an estimated optical depth up to several hundred. The primary thermal relaxation mechanism is identified and found to have a negligible contribution to the total linewidth at 2 K. We find that inhomogeneous broadening due to the disordered isotopic environment in natural ZnO is significant, contributing 2 GHz. Two-laser spectral hole burning measurements, indicate the dominant mechanism, however, is homogeneous. Despite this broadening, the high homogeneity, large optical depth and potential for isotope purification indicate that the optical properties of the ZnO donor-bound exciton are promising for a wide range of quantum technologies and motivate a need to improve the isotope and chemical purity of ZnO for quantum technologies.

5.1 Introduction

In chapter 4 we experimentally investigate and theoretically model the longitudinal relaxation time of the D^0, where we showed that the D^0 has potential for long coherence times. For photon-based quantum network applications, we must also show that optical properties of the $D^0 \leftrightarrow D^0X$ are favorable. Two figures of merit for optically-active quantum defects are the oscillator strength, and the ratio of the optical transition linewidth to the Fourier-transform limited linewidth. High oscillator strengths are desirable since they are proportional to the photon emission rate of single photon sources and high optical depth is beneficial for optical quantum memories. In ZnO, the $D^0 \leftrightarrow D^0X$ is bright with a radiative lifetime of 0.86, 1.06 and 1.35 ns for Al, Ga, and In respectively [84]. A linewidth broader than the lifetime transform limit impacts photon indistinguishability and the strength of the photon-spin interaction, for both ensemble [58] and single defect applications [112].

Our goal is to elucidate the various sources - both homogeneous and inhomogeneous - that contribute to the $D^0 \leftrightarrow D^0X$ transition linewidth beyond this radiative limit. After describing the samples in Sec. 5.2, in Sec. 5.3.1 we show that the inhomogeneous ensemble optical linewidth of $D^0 \leftrightarrow D^0X$ at 1.8 K can be as low as 7 GHz, compared to the $\mathcal{O}$(100 MHz) Fourier-transformed lifetime linewidth. Transmission measurements also show a very high estimated optical depth of 25 to 300 for the Ga and Al ensembles, orders of magnitude greater than those in rare earth ion-doped (REI) crystals [113] and silicon radiation damage centers [114], and approaching that of cold atoms [115, 116]. By measuring the linewidth as a function of temperature in Sec. 5.3.2, we find that the dominant phonon contribution to the linewidth is via population relaxation between the D^0X excited states. This homogeneous broadening mechanism is negligible at 2 K. In Sec. 5.3.3, we calculate an intrinsic inhomogeneous broadening due to isotopic variation on the order of a few GHz. Finally, in Sec. 5.3.4, we probe the homogeneous linewidth via spectral anti-hole burning. We find surprisingly that the spectral anti-hole linewidth, which is measured on microseconds timescales, is the dominant contributor to the ensemble linewidth. We conclude with a discussion on how

these properties may impact donor qubit operation and how they may be further improved.

5.2 Samples

The two samples studied in this work are 300 µm-thick Tokyo Denpa single-crystal substrates from the same parent crystal. Sample A is untreated and Sample B has undergone indium implantation and annealing to form In donors at the surface (∼200 nm deep) [81]. Three donor species are studied: Al, Ga, and In substituting for Zn. The donor concentrations in the first two microns of sample B's surface were determined by secondary ion mass spectroscopy (SIMS) measurements as $1.2{\cdot}10^{15}\,\mathrm{cm}^{-3}$ for Al and $9.2{\cdot}10^{15}\,\mathrm{cm}^{-3}$ for Ga [81]. The bulk doping concentration for In was below the SIMS detection limit. We note that the PL intensity of the individual lines can vary by an order of magnitude across the sample. One possible cause would be non-uniform incorporation during growth.

5.3 Results

5.3.1 Ensemble Optical Linewidth

A photoluminescence (PL) spectrum showing emission from all three donors in sample B is shown in Fig. 5.1b. We observe six peaks between 3.355 eV and 3.363 eV. The transitions labelled Al, Ga, and In correspond to the transition between the 1s D^0 and the lowest energy D^0X state of the respective donor species ($D^0 \leftrightarrow D^0X$) [84]. The transitions Al*, Ga*, and In* correspond to transitions from an excited D^0X state, which we denote as D^0X^*. The D^0X^* intensity becomes brighter with increasing temperature. The energy differences between the D^0X^* and D^0X for Al, Ga, and In are 1.26 meV, 1.46 meV, and 2.05 meV respectively. As discussed in Sec. 5.3.2, the presence of these excited states contribute to a phonon-induced broadening of the D^0X transitions at elevated temperatures.

The linewidths in Fig. 5.1b are spectrometer resolution-limited (55 GHz). We thus utilize micro-photoluminescence excitation (PLE) spectroscopy to determine the ensemble linewidths. In PLE measurements, we scan a continuous-wave laser near the $D^0 \leftrightarrow D^0X$

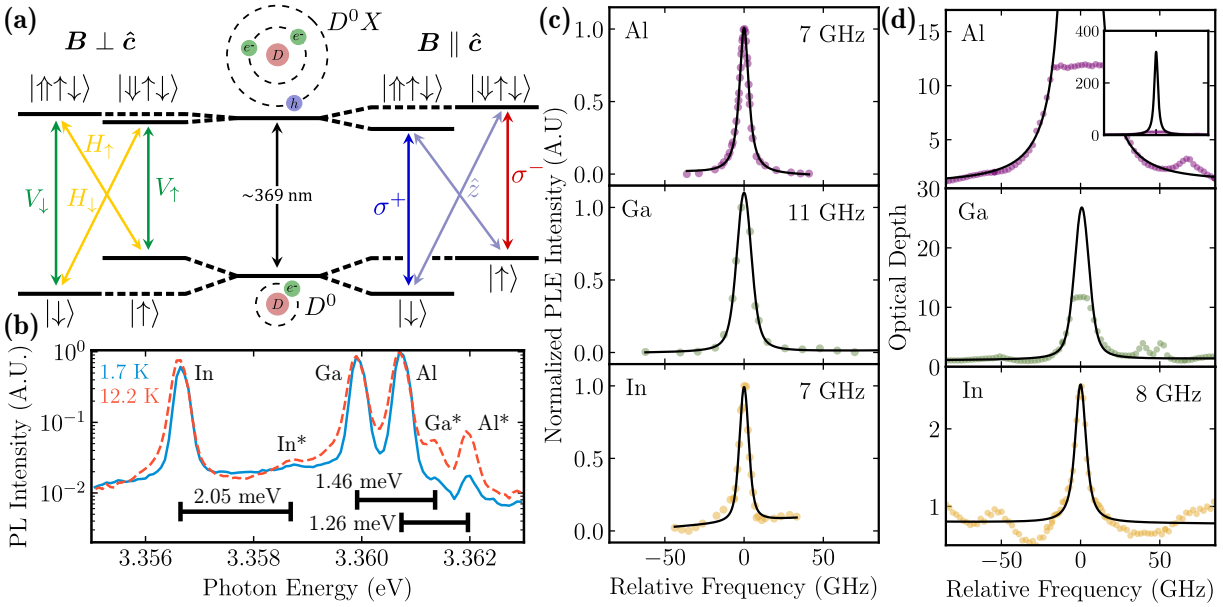

Figure 5.1: (a) Energy diagram and selection rules in Voigt (left) and Faraday (right) geometries. V_x and H_x denote vertically and horizontally polarized light with x denoting the D^0 ground electron-spin state. Circular polarizations are denoted as σ^+ and σ^+, while $\hat{z}$ corresponds to linear polarization parallel to the optical axis. (b) PL spectrum of Sample B. Al, Ga, and In (Al*, Ga* and In*) label the corresponding $D^0 \leftrightarrow D^0X$ ($D^0 \leftrightarrow D^0X^*$) transitions. Excitation energy is 3.44 eV, power is 30 nW and diameter is 600 nm. (c) PLE of the three donor species at 1.7 K for Sample A. Fits are to a Voigt profile and take into account incident power oscillations due to a beam-splitter (App. A.4). Excitation power is 200 nW for Al, 100 nW for Ga and 1.15 µW for In. The beam diameter is 600 nm. (d) Optical density for the three donor species at 1.7 K in Sample A. Fits are to a Voigt profile. For Al and Ga, we constrain the FWHM to the FWHM found in the PLE measurements in (c). The calculation of OD from transmission is given in App. A.3. Excitation power is 15 nW with a diameter of 380 µm. PL spectra in this experimental configuration are given in App. B.1.

resonance and sum over the collected side-band PL. The excitation laser is measured by a wavemeter with a resolution of 0.5 GHz. The side-band PL consists of the two electron satellite (TES) D^0 (2s or 2p) $\leftrightarrow D^0X^*$, first and second phonon replicas (1LO and 2LO) and first phonon replica of the TES (1LO-TES), as described in prior work [81, 95]. The measured PLE linewidths of the Al, Ga, and In D^0X transitions are 7.1 ± 0.1 GHz, 11.1 ± 0.3 GHz, and 7 ± 0.3 GHz, respectively.

The lifetime-limited linewidth Γ is given by $\Gamma = 1/(2\pi\tau)$, where τ is the lifetime measured in the literature [84]. The Al and Ga lifetimes contain a non-radiative component which is attributed to a non-radiative surface recombination mechanism [85] but could also be due to exciton dissociation. Using the faster component as the lifetime value, the lifetime-limited linewidths are 0.5 GHz for Al, 0.4 GHz for Ga, and 0.1 GHz for In. The PLE linewidth is almost two orders of magnitude larger than the expected lifetime limit. The observed broadening could be due to homogeneous factors that would affect a single center on the timescale of our measurements including phonon-broadening, spectral diffusion and hyperfine interactions. It could also be due to inhomogeneous factors such as static microscopic electric and strain fields and isotope disorder. While significantly broader than the lifetime limit, the PLE ensemble linewidth is still remarkably narrow and is less than 100 times the lifetime limit. In comparison, the best ratio of inhomogeneous:radiative linewidths for *in situ* doped nitrogen vacancy (NV) centers is 1000 [117]; this ratio is even larger for REIs [113].

This narrow linewidth persists in transmission measurements. Fig. 5.1d shows the optical depth (OD) αd through the $d = 300\,\mu\text{m}$ substrate, where α is the frequency-dependent absorption constant. The In D^0X absorption linewidth through the 300 µm-thick sample is only 10 % broader than the micro-PLE linewidth, suggesting that high optical homogeneity persists over large volumes. The Al and Ga D^0X transmission measurements saturate at 11.5 OD. This saturation occurs when the resonant PL intensity from the sample exceeds the transmitted laser power. Assuming that the linewidth does not significantly vary between micro-PLE and transmission measurements, a fit to the wings of the transmission spectra give a peak OD of 25 for Ga and more than 300 for Al. The area under each OD peak is proportional to the number of donors in the probed ensemble. We estimate the average donor density for each donor species; $N_{\text{Al}} = 7.5 \cdot 10^{15}\,\text{cm}^{-3}$, $N_{\text{Ga}} = 9.9 \cdot 10^{14}\,\text{cm}^{-3}$, and $N_{\text{In}} = 7.4 \cdot 10^{13}\,\text{cm}^{-3}$ (App. B.2). These values, measured for Sample A, are within an order of magnitude of the SIMS values measured for sample B. The relative concentrations are consistent with the PL spectra for this sample (App. B.1).

An optical depth $\alpha d \gg 1$ is a critical requirement for the development of efficient optical

quantum memories [58]. Warm atomic vapors [118] and cold atoms [119] can achieve optical depths from the tens up to a thousand in cm-scale devices. These high optical depths are more challenging to achieve in solid-state systems which typically have much lower oscillator strengths [113, 114] and large inhomogeneous broadening. In comparison, the ZnO donor-bound exciton system combines high oscillator strength, high homogeneity, and optical depth at residual donor densities.

5.3.2 Temperature-dependent phonon broadening

Defect-phonon interactions can be a dominant homogeneous optical dephasing mechanism, hence we need to confirm that we are performing our linewidth study below thermal broadening limit. Fig. 5.2a depicts the PLE linewidth dependence of the $D^0 \leftrightarrow D^0X$ transition for temperatures varying from 1.5 to 18 K for all three *in situ* doped donors in sample A. Implanted In (sample B) at low implantation doses follows a similar dependence, however a stronger temperature dependence is observed at higher doses (App. B.3).

The onset and rate of the temperature-dependent linewidth broadening is different for the different donor species. The observed temperature dependence can be modeled by a single phonon absorption process with rate $\Gamma(T)$ from the lowest-energy D^0X to an excited D^0X^* state. In ZnO, the primary interaction is likely the piezo-phonon interaction, as has been observed in longitudinal spin relaxation [95]. The precise phonon absorption rate is unclear due to the lack of a satisfactory model for D^0X^*, however, the rate of phonon absorption is proportional to the phonon number N_{ph} at energy ΔE, the energy splitting between the D^0X and D^0X^*states. N_{ph} will follow a Bose-Einstein distribution. This allows us to express the total linewidth as

$$\Delta\nu(T) = \Delta\nu_0 + aN_{ph}(T) = \Delta\nu_0 + a\left(e^{\Delta E/k_BT} - 1\right)^{-1}, \tag{5.1}$$

in which $\Delta\nu_0$ is the temperature-independent component of the linewidth, and $aN_{ph}(T)$ is the broadening due to excitation from D^0X to D^0X^*, and a is a scaling factor that is donor-dependent. While this model is valid for low temperatures, it will eventually break down

near 60 K, where the donor-bound exciton starts dissociating to a neutral donor and a free exciton [83].

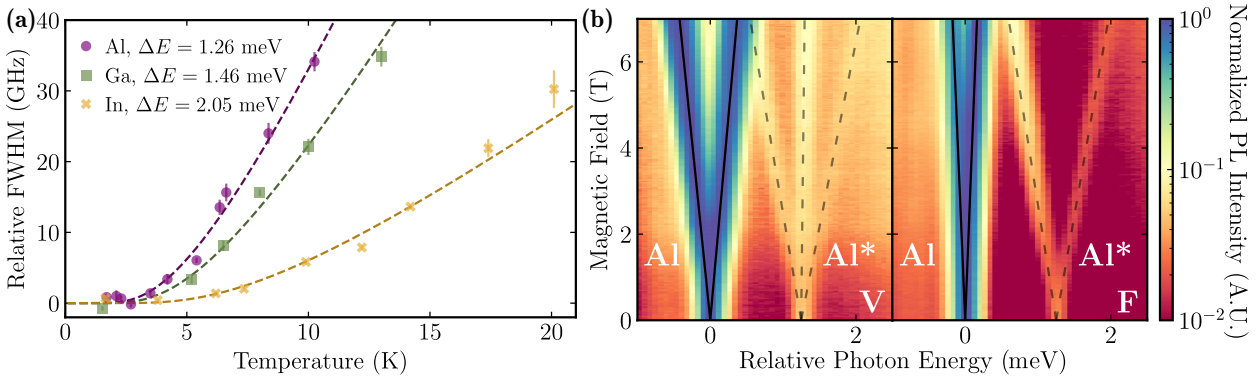

Figure 5.2: (a) PLE linewidth as a function of temperature for Al, Ga, and In. Each data-set is shown with the 0 K linewidth subtracted. All data-sets are fit to Eq. 5.1, with ΔE determined from Fig. 5.1b. $\Delta\nu_0 = 7.4 \pm 0.4$ GHz, 11.8 ± 0.8 GHz, and 6.5 ± 0.5 GHz and $a = 110 \pm 5$ GHz, 99 ± 6 GHz, and 59 ± 4 GHz, for Al, Ga, and In respectively. (b) Magneto-PL of Al donor in Sample A. (left) Voigt (T=7.4 K) (right) Faraday (T = 5.5 K). Excitation at 3.44 eV. In Voigt, the splitting of the (unresolved) doublets corresponds to $g_e = 1.95$, while the D^0X^* splitting corresponds to effective g-factors of 1.87 between observed transitions. In Faraday, the D^0X splitting corresponds to an exciton g-factor $g_{e-h} = 0.83$. The D^0X^* splitting corresponds to an effective g-factor of 3.39.

A fit to Eq. 5.1 using the experimentally measured ΔE (Fig.5.1a) shows good agreement to the model (Fig. 5.2a) at least up to 20 K. The presence of the excited state places a fundamental limit on the maximum temperature at which indistinguishable photons can be obtained from an emitter. In the absence of Purcell enhancement, the temperature at which the temperature component of the linewidth becomes equal to the radiative limit, i.e. $\Delta\nu_{\mathrm{T}} = \Delta\nu_{\mathrm{rad}}$ is $T = 2.7$, 3.1, 3.8 K for Al, Ga, and In respectively. We note that at the lowest temperatures in this study, T = 1.7 K, the phonon contribution to the linewidth is negligible, $\Delta\nu_{(\mathrm{T}=1.7\,\mathrm{K})} = 20$, 4.6, 0.05 MHz for Al, Ga, and In respectively. A difference in the scaling factor a is observed between donors. This difference may be due to the difference in the polarizability of the donors [95, 100], which inversely depends on state localization [120]. Polarizability will increase from In to Ga to Al, which is consistent with the observed increase

in a.

In order to gain insight into the nature of the D^0X^* state, we collected PL spectra as a function of magnetic field. Fig. 5.2b depicts the Al D^0X and D^0X^* field dependence. App. B.4 includes magneto-PL for all donors. In both geometries, the D^0X observed splittings are consistent with the reported g-factors for the electron and hole i.e. an electron g-factor of $g_e = 1.97$, and hole g-factors of $g_h^{\perp} = 0.34$ and $g_h^{\parallel} = -1.22$ for Voigt and Faraday geometries respectively [54, 95]. However we observe three transitions for D^0X^* in Voigt and a very large exciton splitting ($g_{\text{exciton}} = 3.39$) in Faraday. Our g-factor measurements differ from Ref. [121] in which it was reported that the g-factor of D^0X^* is the same as that of D^0X. We attribute this discrepancy to the high density of overlapping lines around the Ga and Al D^0X^* energies in Ref. [121] which could result in state misidentification. The origin of the three transitions (versus 2 or 4 observed for D^0X) and large g-factor is currently unknown. Interpretation of the excited states of the bound exciton is discussed further in App. B.5.

5.3.3 Inhomogeneous Broadening Due to Isotopic Composition

After thermal homogeneous broadening, inhomogeneous broadening is often another dominant broadening source. Inhomogeneous broadening of the $D^0 \leftrightarrow D^0X$ transition energy can be caused by extrinsic factors such as local variations in strain and electric fields due to point and extended defects. Intrinsic contributions to inhomogeneous broadening can occur due to nuclear spin or isotopic mass composition of the emitter's environment. The latter is a dominant inhomogeneous broadening mechanism in high quality natural silicon [122–124]. Here we estimate the effect of isotopic mass composition on the ZnO D^0X optical linewidth. The effect of the nuclear spin environment on the linewidth was also considered, however, with the exception of a large In donor hyperfine splitting [81], this was not found to have a significant effect (App. B.6).

The local isotopic mass environment can effect the $D^0 \leftrightarrow D^0X$ transition by local variation in the zinc and oxygen isotopes in the defect's environment, by or variation of the isotope of the impurity atom. The $D^0 \leftrightarrow D^0X$ transition closely follows the local band gap, which

is determined in part by the zero-point electron-phonon renormalization [125, 126]. This zero-point renormalization energy depends on the average mass of atoms present in the local environment [126]. To assess the effect of isotopic substitution on a specific state or set of states, the band gap variation must be decomposed into conduction band and valence band shifts [127, 128]. These have different temperature dependences, and thus different zero-point renormalization energies [126]. In ZnO, the valence band will shift by approximately 80% of the total band gap shift, while the conduction band exhibits a shift in the opposite direction of 20% [129].

To quantify the resulting shifts, we follow the method presented for silicon in Ref. [123], modified for ZnO. Here the carrier wavefunction is discretized on atomic sites $\vec{r}_i$. The model for the effective mass envelope functions of the D^0 electron and D^0X electrons and hole are given in App. A.1. In this model, the energy shift for a given carrier state due to perturbation of its isotopic environment is given by $\langle \Phi_{\mathrm{S,c}}(\vec{r}_i)|H_i^{\mathrm{iso}}|\Phi_{\mathrm{S,c}}(\vec{r}_{i'})\rangle = \delta_{i,i'}W_{i,c}$, where $|\Phi_{\mathrm{S,c}}(\vec{r}_i)\rangle$ refers to the Bloch function for state S (D^0 or D^0X), carrier c (e = electron or h = hole), the lattice site i at a distance $\vec{r}_i$ from the impurity, H_i^{iso} is the perturbation term, and $W_{i,c}$ is the energy shift due to the isotopic variation. The energy shift results from a shift in the top of the valence band or bottom of the conduction band, depending on if the carrier is a hole or an electron respectively. Shifts are relative to the lowest mass isotope. The values for these shifts are listed in Table B.2 in App. B.8.

The total shift $\Delta E_{S,c}^{iso}$ on each state S and carrier c is

$$\Delta E_{S,c}^{iso} = \Delta E_{S,c}^{imp} + \sum_{i \in \text{ lattice sites}} \langle \Psi_{S,c}(\vec{r}_i)|H_i^{iso}|\Psi_{S,c}(r_i)\rangle, \tag{5.2}$$

where Ψ refers to a carrier state with an effective mass envelope function as defined in App. A.1. $E_{S,c}^{imp}$ is the shift from substitution of the impurity atom isotope, which was found to have only a small effect, as discussed in App. B.8. The total shift of $D^0 \leftrightarrow D^0X$ is determined by the difference between the D^0 and the D^0X shifts. Since they inhabit the same isotopic environment, their shifts will be correlated (Fig. 5.3a). The total transition shift is given by $\Delta E_{iso} = (2\Delta E_{D^0X,e}^{iso} + \Delta E_{D^0X,h}^{iso}) - \Delta E_{D^0,e}^{iso}$, accounting for the two electrons

and hole in the D^0X state, and electron in the D^0 state.

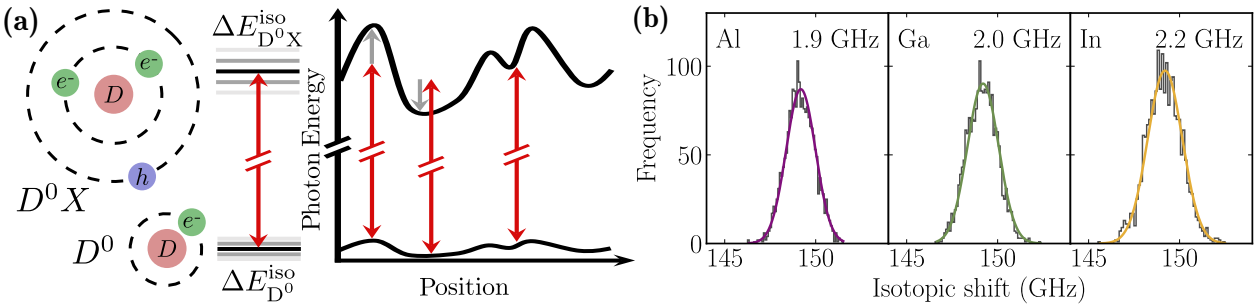

Figure 5.3: Isotopic broadening for each shallow donor type. Different local environments will shift the energies of the D^0 and D^0X by different but correlated amounts, with the D^0X shifting more due to the mobility of the valence band in ZnO. We calculate 1.9 GHz broadening for Al, 2.0 GHz for Ga, and 2.2 GHz for In.

The isotopic mass environment broadening is determined numerically using 2000 simulated environments for each D^0 and D^0X. As shown in Fig. 5.3b, the estimated total contribution of the isotopic mass environment to the inhomogeneous broadening is 1.9 GHz, 2.0 GHz, and 2.2 GHz for Al, Ga, and In respectively. Less localized states (*e.g.* Al) are affected by a larger number of environmental lattice sites, leading to smaller deviations in the local isotopic mass environment. Using this model for the phosphorus $D^0 \leftrightarrow D^0X$ transition in natural silicon, which is known to be isotopically broadened, yields an inhomogeneous linewidth that is in good agreement with observation (Sec. B.4) [124]. Thus in the current samples, while not negligible, the isotopic environment is not the dominant broadening mechanism in the ensemble linewidth.

5.3.4 Homogeneous Spectral Anti-Hole Linewidth

We thus probe the homogeneous linewidth of the Al donor with spectral anti-hole burning measurements to elucidate the nature of the dominant broadening mechanism. The anti-hole linewidth will not be affected by the static varying isotopic environment [124]. We perform these two-laser experiments in a pump-probe configuration to probe time-dependent mecha-

nisms such as spectral diffusion. We have also performed continuous-wave (cw) measurements which yield similar linewidths (App. B.9).

Setting a single probe laser resonant to the σ^- transition, as shown in Fig. 5.4a, we optically pump (OP) the sub-ensemble population from the $|\uparrow\rangle$ to the $|\downarrow\rangle$ spin state. Hence, when collecting the side-band emission, we observe a decrease in signal that is proportional to the population depletion of the $|\downarrow\rangle$ spin state (Fig. 5.4b). In the absence of a pump beam, the probe signal is small due to the small thermal population in the $|\uparrow\rangle$ state.

When we perform optical pumping as a function of probe laser wavelength, intensity at the start of the optical pumping curve varies as the laser is scanned over the resonance. If we integrate this signal in the first 2 microseconds and plot the intensity as a function of probe frequency, we observe a linewidth of $4.2 \pm 2.8\,\mathrm{GHz}$. This is comparable to the 7 GHz 0-field cw PLE linewidth. If instead we integrate the signal at the end of the optical pumping curve, *i.e.* when the system is in the optically-pumped state, a linewidth of $16.0 \pm 0.9\,\mathrm{GHz}$ is observed (Fig. 5.4d). The broader linewidth in the optically-pumped state is expected as efficient optical pumping on-resonance decreases the peak intensity. The similarity between the zero-field cw measurements and the time-dependent PLE in which the start of the optical-pumping curve is integrated is expected as optical pumping should not occur at zero-field.

We next introduce a second excitation laser resonant to the σ^+ transition ("Pump" laser in Fig. 5.4a). The pump laser initializes the sub-ensemble with which it is resonant from the $|\downarrow\rangle$ to the $|\uparrow\rangle$ spin state. After a wait time τ_w, the probe laser optically pumps the sub-ensemble $|\uparrow\rangle$ to the $|\downarrow\rangle$ spin state. In Fig. 5.4c an enhanced optical pumping signal is observed when the probe laser is applied after the pump. The amplitude of the optical pumping signal, plotted as a function of probe frequency, determines the linewidth of the resonantly pumped sub-ensemble and thus the homogeneous linewidth of the $\mathrm{D}^0 \leftrightarrow \mathrm{D}^0\mathrm{X}$ transition. As shown in Fig. 5.4d, we observe a linewidth of $3.9 \pm 0.5\,\mathrm{GHz}$. Varying the wait time does not affect initial amplitude of the OP curve (App. B.10). Thus the homogeneous linewidth appears to be the dominant component to the spectral anti-hole linewidth.

The observed spectral anti-hole linewidth can be attributed to the $\mathrm{D}^0\mathrm{X}$ state; two laser co-

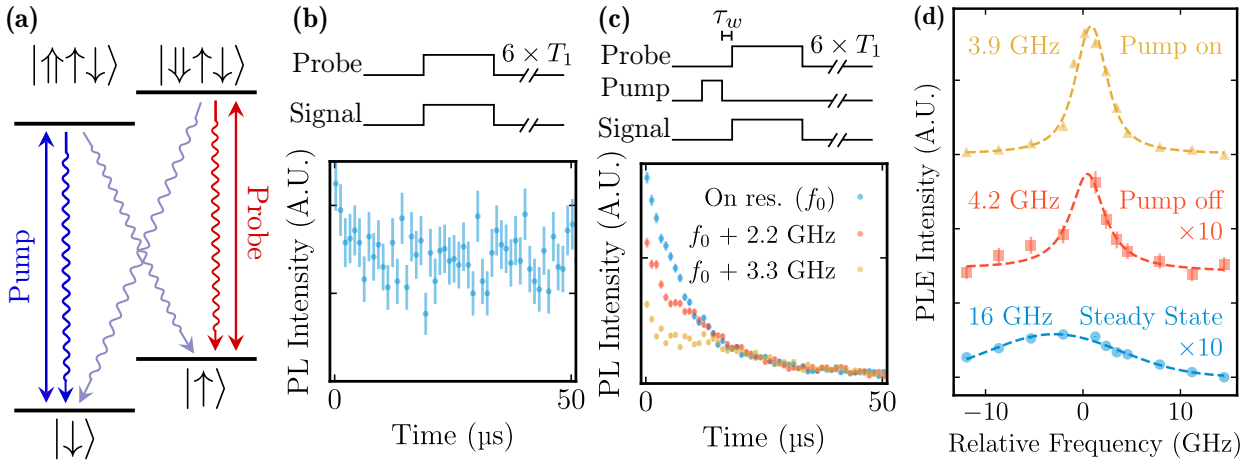

Figure 5.4: (a) An energy diagram for spectral hole burning experiment. (b) Single laser optical pumping (OP) curve with 230 nW probe laser power. (c) OP curves in pump-probe experiment with the 230 nW probe laser, 440 nW pump power and 100 µs pump pulse length. Three excitation frequencies are shown (on resonance, +2.2 GHz, and +3.3 GHz detuned). Both (b) and (c) contain a schematic of the pulse sequence. Between cycles, the wait time is 6× the 1.5 ms longitudinal spin relaxation time (T_1). (d) PLE curves for transient experiments. Fit is to a Voigt profile. For clarity, each spectrum has been offset vertically, and the steady state and single laser initial state curves are scaled ×10. Faraday geometry at 7 T and 1.8 K.

herent population trapping experiments, which probe the D^0 coherence report a two-photon spin linewidth in the tens of MHz for Al [81]. The time dynamics of the optical pumping curve (Fig. 5.4c) suggest a laser-induced diffusion process is occurring. In contrast to single laser experiments, in which the optical pumping curve can be characterized by a single exponential [54], complex temporal dynamics of the curve are observed following the pump pulse. As both the intensity and frequency of the probe pulse are fixed, this temporal dynamics suggest a time-dependent change in the transition frequency/lineshape of the probed donors. We expect spectral diffusion is also occurring during the pump pulse, *i.e.* as D^0X population is depleted at the resonant pump frequency, near-in-frequency D^0X population diffuse into this depletion region. Future studies are required to elucidate the origin of the spectral diffusion process. Potential sources include changes in the microscopic charge environment due

to nearby impurities and defects, and instantaneous spectral diffusion (ISD) [130], in which excited D^0X within the ensemble interact electromagnetically. This is a well-documented phenomenon in REIs where the interaction is dipolar. In the D^0 case, the effect may be more severe. The D^0 and D^0X effective mass states are significantly extended as compared to REI's with a significant difference between the single electron D^0 and three-carrier D^0X wavefunctions (App. A.1).

5.4 Discussion and Outlook

Further studies are required to confirm the origin of the homogeneous linewidth. If it is due to ISD, there are two immediate impacts on quantum information technologies. First, for single quantum defect applications, lower donor densities are required. In REI's, this can be achieved by burning a large spectral hole from which a narrow, low-density anti-hole can be established [131]. This strategy is only feasible when the homogeneous linewidth is much narrower than the inhomogeneous linewidth, a condition not satisfied in our samples. Thus lower donor dopant densities will be required. On the flip side, a large ISD linewidth indicates a large D^0X-D^0X interaction which long-term could provide a mechanism for D^0-D^0 gates [132].

The total lineshape will be a convolution of the inhomogeneous and homogeneous lineshapes. In the simple model in which we take the homogeneous lineshape to be Lorentzian with FWHM $\Delta\nu_L$ and the inhomogeneous lineshape to be Gaussian with FWHM $\Delta\nu_G$, the ensemble linewidth can be approximated by $\Delta\nu_L/2 + \sqrt{\Delta\nu_L^2/4 + \Delta\nu_G^2}$ [98]. For Al, the narrowest measured homogeneous linewidth is 3.9 GHz with an ensemble linewidth ranging from 4.2-7 GHz, resulting in an inhomogeneous linewidth ranging from 1.1 to 4.6 GHz. This range is consistent with the 1.9 GHz inhomogeneous broadening estimated due to isotope disorder and suggests isotope broadening is the dominant inhomogeneous broadening mechanism.

Both chemical and isotope purification will thus be key to the development of optical quantum technologies with ZnO. Isotope purification, already required to improve the D^0 spin coherence by removing non-zero spin nuclear isotopes [54], will be further advan-

tageous to reduce broadening from mass disorder. Chemical purity will improve the homogeneous linewidth, either by eliminating impurities/defects that contribute to spectral diffusion and/or lowering the inter-donor spacing to reduce instantaneous spectral diffusion. Even without these materials improvements, the current linewidth properties are sufficient for several applications if donors can be integrated into photonic devices. A Purcell enhancement of less than 100 can enable the generation of indistinguishable photons. Detuned Raman excitation schemes can also mitigate against excited state dephasing [49, 133]. Finally, if single donors can be isolated, theoretical schemes to entangle donors with trapped ions [134] should be possible with the current optical properties.

Chapter 6

ISOLATION OF SINGLE DONORS

Originally published as [94]: E. R. Hansen, V. Niaouris, B. E. Matthews, C. Zimmermann, X. Wang, R. Kolodka, L. Vines, S. R. Spurgeon, and K.-M. C. Fu, *Isolation of Single Donors in ZnO*, 2024, arXiv:2310.05806 [cond-mat.mes-hall]

In this chapter, single indium donors are isolated in a commercial ZnO substrate using plasma focused ion beam (PFIB) milling. Quantum emitters are identified optically by spatial and frequency filtering. The indium donor assignment is based on the optical bound exciton transition energy and magnetic dependence. The single donor emission's stability in intensity and frequency, alongside a transition linewidth less than twice the lifetime limit, highlighting the suitability of single In donors as optically accessible spin qubits. Moreover, the optical stability of single donors post-FIB fabrication is promising for optical device integration required for scalable quantum technologies based on single donors in direct band gap semiconductors.

6.1 Introduction

In chapter 4 and chapter 5 we have shown ensemble optical and spin properties favorable for photon-based quantum network applications. However, most of these applications require individually addressable qubits. The low chemical purity of commercially available ZnO substrates [81, 135] compared to host materials like silicon and diamond is a challenge for isolating single donors in ZnO. This difficulty is compounded by the ease of forming single atom substitutional point defects compared to defect complexes such as the nitrogen-vacancy and silicon-vacancy center in diamond [136] and radiation damage centers in silicon [137]. Commercially available ZnO crystals, with total donor concentrations exceeding $10^{16}\,\mathrm{cm}^{-3}$,

render optical isolation of single donors unattainable through optical confocal imaging. While single fluorine donors [138, 139] and nitrogen acceptors [140] have been isolated in the direct band gap semiconductor ZnSe using very narrow quantum wells, there exists a high-level of inhomogeneity induced by the inherently fluctuating quantum-well potential. This results in observed linewidths of ∼54 GHz, which is 65 times greater than the expected lifetime-limited linewidth [139]. Here, we aim to isolate single donors in ZnO while maintaining the bulk donor and donor-bound exciton properties by reducing the material volume and focusing on lower abundance In donors.

Focused ion beam (FIB) milling has been extensively used to extract and shape materials at the nanoscale [141–144], enabling the fabrication efficient photon extraction devices [145–147] for quantum defects [148]. FIB fabrication, however, results in a damaged layer of material [149, 150] which can degrade the optical and spin properties of some quantum defects [151, 152]. Given that ZnO is a radiation resilient material [51], FIB milling may be a viable method for isolating single In donors without diminishing their favorable spin and optical properties.

We isolate single In donors in ZnO via Xe^+ plasma FIB (PFIB) milling and perform an optical characterization, revealing stable and narrow emissions well suited for use as single spin qubits. Following PFIB processing, the optical properties of the ZnO are severely degraded; however, a 1-hour oxygen anneal recovers sharp donor-bound exciton (D^0X) to donor-bound electron (D^0) photoluminescence (PL) lines. Single In donor candidates are optically isolated with spectral and spatial filtering. Verification of emitters corresponding to In donors is achieved via collection of the two-electron satellite transition under resonant excitation and magneto-photoluminescence. Lifetime measurements reveal a ten-fold lifetime reduction relative to bulk ZnO, indicative of non-radiative channels. Measured linewidths, however, are less than a factor of two broader than the measured lifetime-limit. Further materials and fabrication improvements, combined with device integration for Purcell enhancement, could be used to enhance the radiative efficiency.

6.2 Sample and fabrication process

For this work, a 360 µm-thick Tokyo Denpa ZnO crystal is used as the parent substrate, with the crystal axis $\hat{c}$ perpendicular to the substrate surface, the same sample used in chapter 4. We observe Al, Ga, and In donor-bound exciton (Al^0X, Ga^0X, and In^0X) in the substrate. The donor concentrations, measured on the back surface, were determined by secondary ion mass spectrometry (SIMS) measurements as $5.3 \cdot 10^{14}\,cm^{-3}$ for Al and $4.4 \cdot 10^{15}\,cm^{-3}$ for Ga (App. C.1). The In concentration was below the SIMS detection limit. Since the donor concentration can vary across the substrate, these values provide an order of magnitude estimate.

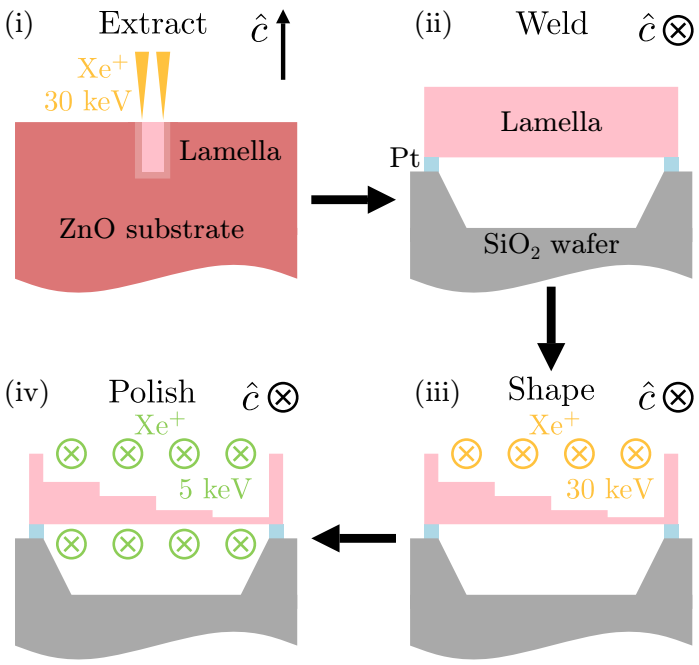

Figure 6.1: Lamella preparation process: (i) lamella extraction from ZnO substrate, (ii) lamella welded on SiO_2 wafer, (iii) PFIB milling of lamella, (iv) removal of high energy PFIB-related damage with low energy PFIB.

Traditionally, FIB technologies use Ga^+ beams [143] which could unintentionally introduce a high-density of Ga donors in ZnO, thus we utilize a PFIB with an inert ion gas

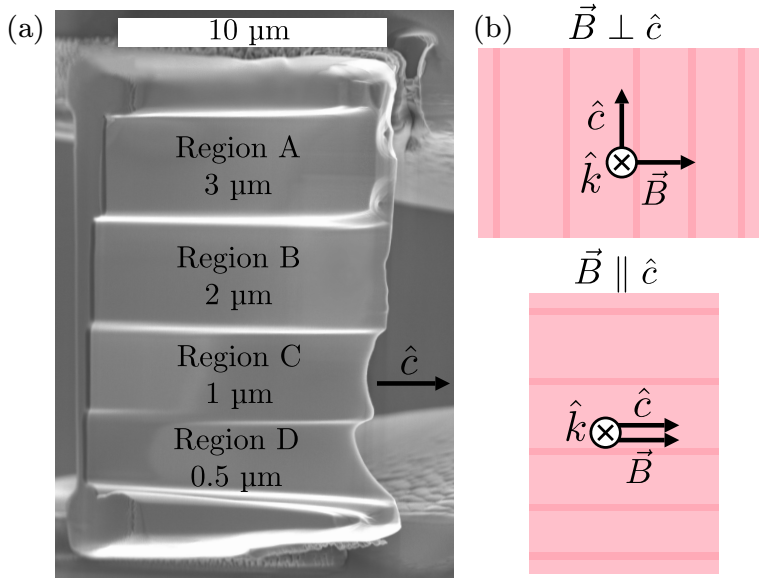

Figure 6.2: (a) Scanning electron microscopy image of lamella. (b) Orientation of crystal ($\hat{c}$) and optical ($\hat{k}$) axes with respect to the magnetic field $\vec{B}$.

source, Xe^+, to cut a 5 µm-thick cross-section (lamella) from the ZnO parent substrate. Using standard lift-out techniques, a micro-manipulator needle removed the lamella (Fig. 6.1i) and laid it over a PFIB-milled trench on a SiO_2 wafer (Fig. 6.1ii). The edges of the lamella were secured with Pt deposited by cracking a metal organic gas (flowed in using a standard gas injection system) with the Xe^+-beam (Fig. 6.1ii). Tiered steps of thicknesses ranging from 0.5 µm to 3 µm were milled using a 30 keV beam, with the crystal $\hat{c}$ axis parallel to the step edges (Fig. 6.1iii). The lamella was then polished with a 5 keV beam on both sides to remove re-sputtered material and amorphous damage that often occurs during the higher energy milling processes (Fig. 6.1iv). The lamella (Fig. 6.2a) was annealed at 700 °C for 1 hour under O_2 flow to reduce remaining milling damage [81].

All measurements were conducted with a confocal microscope that images the lamella inside a helium immersion cryostat with a superconducting magnet (App. C.2). The magnetic field $\vec{B}$ is always parallel to the lamella plane. We access two magnetic field orientations, $\vec{B} \parallel \hat{c}$ and $\vec{B} \perp \hat{c}$, by rotating the lamella (Fig. 6.2b).

6.3 *Annealing effect on photoluminescence*

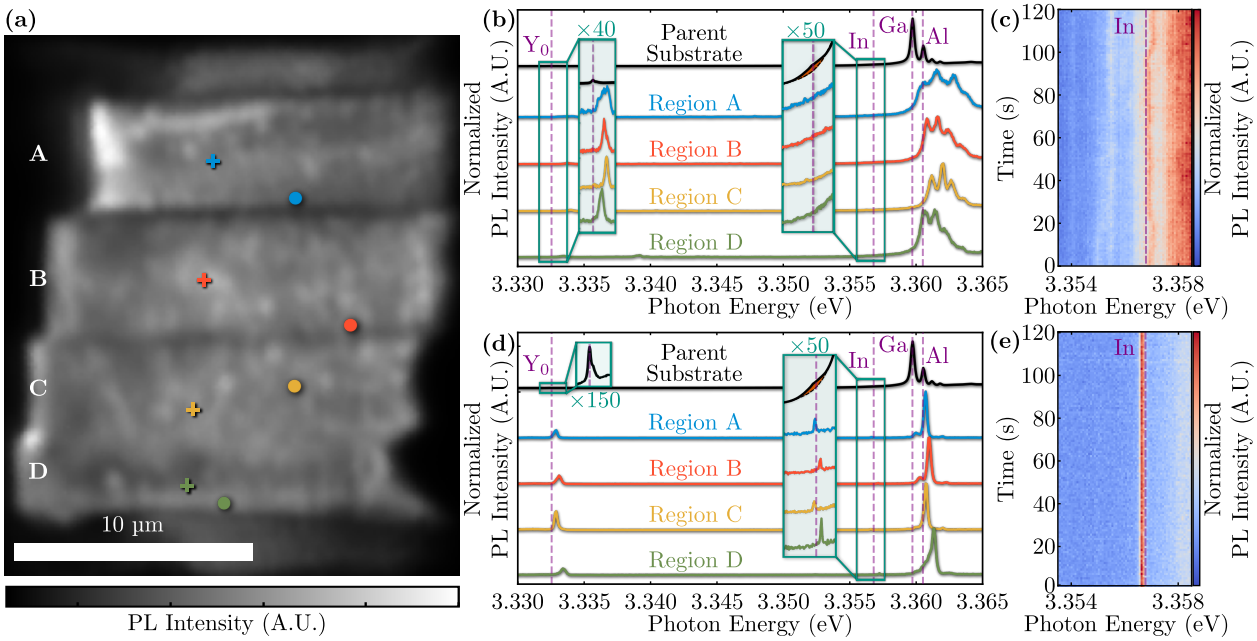

Figure 6.3: Continuous-wave excitation at 3.44 eV, T = 5.2 K. (a) Confocal PL image of lamella post-anneal. Cross (circle) markers indicate the locations for spectra in Fig. 6.3b (Fig. 6.3d). (b) and (d) PL spectra of pre- and post-annealed lamella respectively, normalized to maximum intensity. Dashed lines mark the D^0X transition for different donors [84]. Insets depict expanded views near the Y_0 (left) and In^0X (right) lines. (c) and (e) PL kinetic series from region C of the pre- and post-annealed lamella, respectively.

Fig. 6.3a displays a confocal PL image of the lamella post-annealing. PL spectra from the substrate and each region of the pre-annealed lamella are shown in Fig. 6.3b. The substrate spectrum shows a small shoulder at the In^0X transition [84] with a peak intensity roughly $3 \cdot 10^{-4}$ times that of the Ga^0X peak. Based on the measured Ga density and assuming that the relative peak intensity and donor concentration are proportional, we estimate 10^{12} In donors/cm^3. With an excitation spot diameter of ∼450 nm, a ∼5 µm thick slice of the substrate would yield one In donor per excitation spot, with smaller concentrations for the $0.5 - 3$ µm thick steps of the lamella.

A weak Y_0 line, related to excitons bound to structural defects [84], is observed in the

substrate PL. After PFIB fabrication, an increase in the Y_0 PL intensity relative to the Ga^0X and Al^0X lines is observed, which we ascribe to the creation of structural defects during fabrication (Fig. 6.3b). Additionally, an overall PL shift varying across the lamella is observed, consistent with differential strain environments. Within a single excitation spot, the Ga^0X and Al^0X lines also show splitting and broadening which we attribute to microscopic strain (Fig. 6.3b).

We monitored the PL spectra as a function of time in kinetic series measurements; Fig. 6.3c shows a series from region C. Multiple weak features are observed, with a stronger line at the In^0X transition. Similar features are observed at multiple locations in the lamella (App. C.3). These stronger emitters at the In^0X transition exhibit discrete spectral jumps, a behavior characteristic of isolated single emitters in an unstable environment [153–155].

After annealing, the broad Ga^0X and Al^0X lines become single, sharp transitions, suggesting that annealing removed a majority of the milling-induced damage (Fig. 6.3d). A small overall PL shift persists after annealing. Interestingly, the intensity of the Ga^0X line relative to the Al^0X line is greatly diminished when compared to the substrate PL. The cause of this reduction is unknown.

Near the In^0X line we now observe spots with strong, spectrometer-resolution limited emission (Fig. 6.3d right inset). A representative PL kinetic series is shown in Fig. 6.3e (more available in App. C.3). Compared to the pre-annealed PL spectrum, the PL emission at the In^0X transition becomes stronger and spectrally stable. Additionally, the weaker features around the In^0X region are no longer observed, suggesting that they may have been surface-related shallow defects which were eliminated via annealing [156].

6.4 Observation of localized In donor emitters

To spatially resolve single In donors, we perform confocal PL scans while spectrally filtering the In^0X emission; the resulting image is shown in Fig. 6.4a. Localized emission with spectrometer-resolution limited linewidths at In^0X are observed (Fig. 6.4b). The highest density of emitters is found in regions B and C rather than the thicker region A. We note

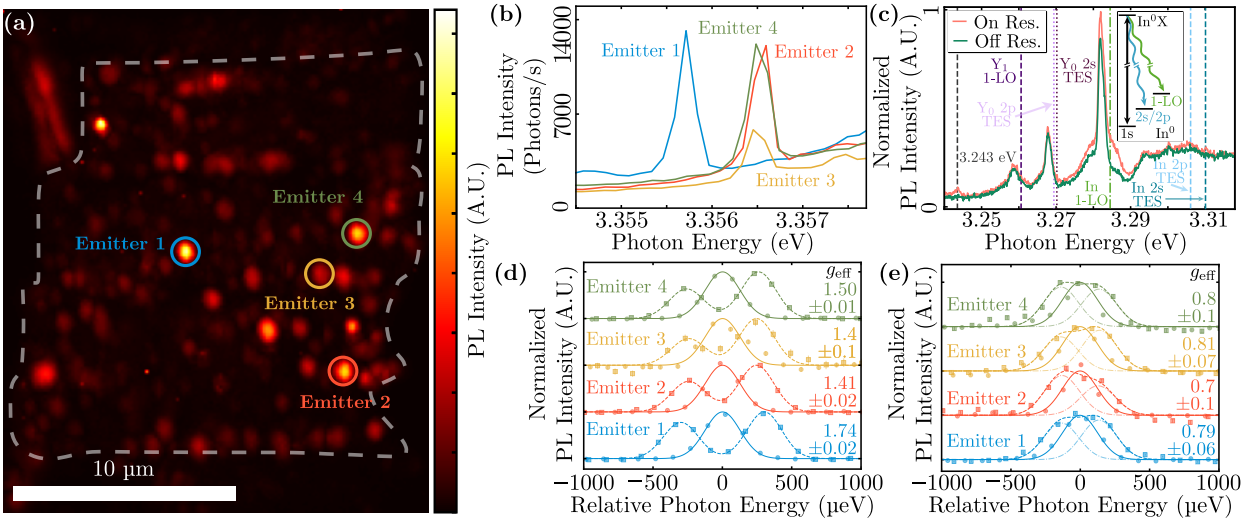

Figure 6.4: Continuous-wave excitation at 3.44 eV. (a) Confocal PL image collecting 3.354 − 3.357 eV. T = 5.2 K. (b) PL spectra of four emitters at 5.2 K. Spectra are shifted to adjust for strain-induced energy offsets. (c) Sideband PL of emitter 2 under resonant excitation at 3.355948 eV, T = 5.2 K, normalized to the peak of the on-resonance spectrum. Dashed lines mark reported transitions [81, 84]. Inset depicts energy diagram of resonant excitation, sideband PL collection scheme. (d) and (e) PL spectra with $\vec{B} \perp \hat{c}$ (T = 8.2 K) and $\vec{B} \parallel \hat{c}$ (T = 6.6 K), respectively, at 0 T (circles) and 6 T (squares), with Gaussian fits. The Al/Ga background emission is subtracted. Spectra are normalized to their maximum value.

that the the total PL intensity is also brighter in these regions (Fig. 6.3a) and suspect that the PL intensity may be dominated by surface-related non-radiative recombination. While 5 keV PFIB polishing was performed across the entire sample, different regions were polished by different amounts which could account for the variation in PL intensity.

For the remainder of the paper, we focus on four emitters whose positions are labelled in Fig. 6.4a. The PL spectra corresponding to each emitter is shown in Fig. 6.4b, where the spectra has been shifted utilizing the location of the Al^0X and Y_0 lines to adjust for relative energy offsets induced by strain (App. C.4).

To verify these emitters as In donors, we resonantly excite the transition between the $In^0(1s)$ state to the In^0X state and collect the PL sideband consisting of the 1-LO phonon-replica and the two-electron satellites (TES) transitions. The TES transitions correspond to

relaxation from the lowest In^0X state to the excited $2s$ and $2p$ states of In^0 (Fig. 6.4c inset). Fig. 6.4c displays the sideband PL for emitter 2 with both on- and off-resonant excitation (see App. C.5 for emitters 3 and 4). For emitters 2–4, resonant PL enhancement is observed at the In 1-LO, 2s and 2p TES transitions [84], as well as an unidentified In-related transition at 3.243 eV that has been observed on a similar ZnO substrate implanted with In (App. C.5). We observe a large background in the In sideband PL. We believe that this is sideband PL from the tails of the much brighter Al^0X and Ga^0X zero-phonon transitions upon which the In^0X transition resides. In contrast with the In-assigned sideband PL, the sideband PL background shifts with laser excitation energy. Resonant sideband enhancement is not observed for emitter 1.

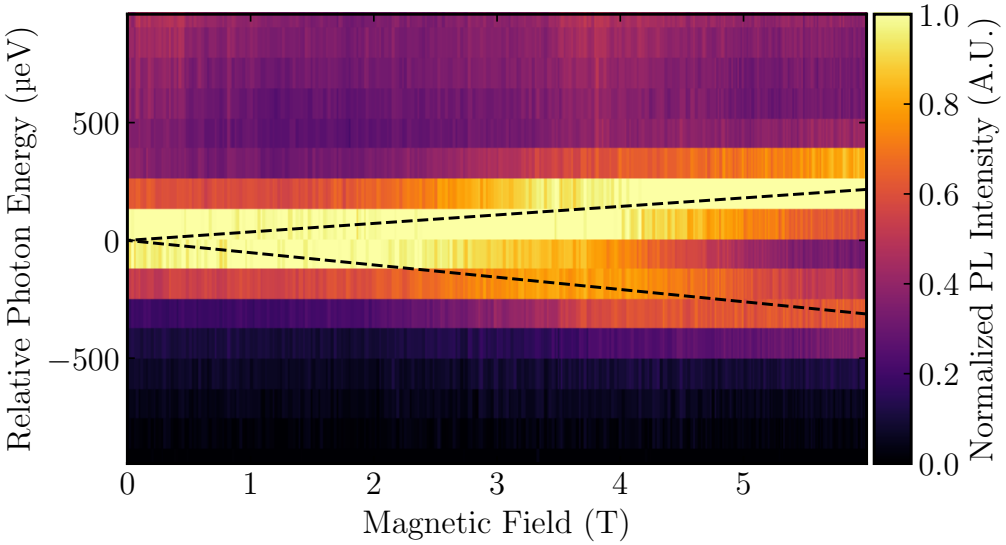

Figure 6.5: PL spectra as a function of magnetic field on emitter 4 in $\vec{B} \perp \hat{c}$ orientation. Each PL spectrum (single vertical line) is normalized to the maximum PL counts in the depicted energy region after subtracting the minimum PL counts in the same region. The dashed lines correspond to a linear fit of the centers of two Gaussian functions, yielding $g_{\text{eff}} = 1.52 \pm 0.01$.

We perform magneto-photoluminescence (magneto-PL) measurements with both $\vec{B} \perp \hat{c}$ and $\vec{B} \parallel \hat{c}$ to verify that the observed Zeeman splittings are consistent with emission from

neutral donors. Fig. 6.4d (Fig. 6.4e) shows the PL of each emitter at 0 T and 6 T with $\vec{B} \perp \hat{c}$ ($\vec{B} \parallel \hat{c}$). In both orientations, we only collect linearly polarized emission perpendicular to the crystal axis $\hat{c}$, which is expected to be 50 times larger than linearly polarized emission parallel to $\hat{c}$ (App. C.6 and Refs. [53, 74, 93]). This strong polarization dependence is also experimentally observed (App. C.6). The effective g factor (g_{eff}) for each orientation is calculated according to $g_{\text{eff}} = \Delta E / (\mu_B B)$, where ΔE denotes the energy splitting of bound exciton transitions and μ_B denotes the Bohr magneton. This splitting results from the hole Zeeman splitting of D^0X and the electron Zeeman splitting of D^0. The hole g factor ($g_h^{\parallel/\perp}$) is then calculated according to $g_h^{\perp} = g_{\text{eff}}^{\perp} - g_e^{\perp}$ ($g_h^{\parallel} = g_e^{\parallel} - g_{\text{eff}}^{\parallel}$), where $g_e^{\perp} \simeq g_e^{\parallel} = 1.95$ [81, 96].

In both orientations, the emission of all emitters splits into two peaks linearly dependent on field as shown in Fig. 6.5, consistent with a donor. If a donor electron is not present, as is the case for an ionized donor-bound exciton, electron-hole coupling yields a non-linear dependence [96]. Measured hole $|g|$ factors are consistent with ensemble measurements[53, 54, 96]. With $\vec{B} \parallel \hat{c}$, we find $g_h^{\parallel}$ to range between -1.14 and -1.2 for all emitters. With $\vec{B} \perp \hat{c}$, we find $g_h^{\perp} = 0.22$ for emitter 1, and between 0.46 and 0.54 for emitters 2–4, which qualitatively follows the literature where reported $g_h^{\perp}$ values vary between 0.1 and 0.34.

6.5 Emission linewidth and lifetime

We utilize photoluminescence excitation (PLE) spectroscopy to determine the linewidth and spectral stability of emitters 2–4. In PLE measurements, we resonantly scan a continuous-wave laser over the $In^0 \leftrightarrow In^0X$ transition and collect sideband PL (Fig. 6.4c). The spectral stability under resonant excitation, with energy less than the ZnO band gap, supports that the donors remain in the neutral charge state in the absence of semiconductor carrier generation. This could be an advantage compared to deep-level defects such as the nitrogen-vacancy center in diamond which undergo two-photon ionization under resonant excitation [157] and require a charge re-pump laser [153, 154].

As shown in Fig. 6.6a, the high resolution PLE spectroscopy enables us to determine the absorption linewidth and also resolve multiple emitters. For example, for emitter 2 we

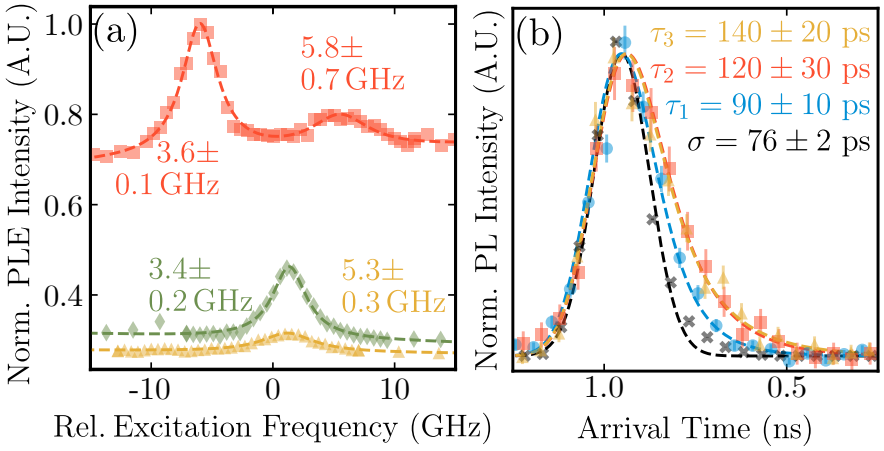

Figure 6.6: T = 5.2 K. (a) PLE spectra of emitters 2–4 normalized to the maximum counts of the emitter 2 spectra. Detector dark counts are insignificant. Exposure time at each excitation frequency varies between 20 − 60 s, based on emitter intensity. Peaks are fit to Lorenzians and labelled with the fit full-width-at-half-maximum. (b) Time-resolved PL of emitters 1–3 under pulsed excitation (2 ps width, 12.5 ns repetition rate) at 3.44 eV. Response function measured with a direct laser reflection and fit to a Gaussian. Time-resolved PL is fit with two exponential-Gaussian convolution profiles to account for the In emitter and the Al/Ga background (App. C.7). Fits are labelled with the In lifetime.

observe a weak second peak corresponding to a second emitter. The emitter linewidths range between 3.4 GHz and 5.8 GHz.

The expected linewidth of a lifetime-limited emitter at 5.2 K is estimated by adding three different contributions. First, the line is split by 0.5 GHz due to the zero-field hyperfine interaction between the donor electron spin-$\frac{1}{2}$ and the In nuclear spin-$\frac{9}{2}$ ($A_{\mathrm{In}} = 100$ MHz) [91, 92]). At 0 K, the two hyperfine lines would have a lifetime-limited linewidth of 120–150 MHz, given by the reported In ensemble lifetime [84, 85]. Each line is further broadened by 0.65 GHz due to a phonon-assisted thermal population relaxation between D^0X states at 5.2 K (Sec. 5.3.2). Under these effects, the two lines are not resolvable, with a total effective linewidth of 1.2 GHz; 3 times smaller than the observed values. Additionally, the disparity between the expected and measured linewidths could be a result of a shortened lifetime compared to the literature value.

We performed time-resolved PL measurements using pulsed laser excitation to probe the emitter lifetime. As shown in Fig. 6.6b, we observe excited state lifetimes between 90 ps and 140 ps, one order of magnitude smaller than ensemble lifetimes [85]. We attribute the shortened lifetime to non-radiative surface recombination which has been suggested to explain the fast decay component in studies on ensemble lifetimes in ZnO [85]. The intensity of the emission does not increase when lowering the temperature to 2 K (Fig. 6.7), suggesting that the recombination mechanism is not thermally activated. Accounting for the diminished lifetimes, we estimate a radiative efficiency of $\sim$10 % and lifetime-limited linewidths ranging from $1.1 - 1.8$ GHz, depending on the emitter. The total homogeneous linewidth increases to $2.0 - 2.6$ GHz once contributions due to phonons and the hyperfine interaction are included. The measured linewidths, while only $1.3 - 3$ times larger than the lifetime-limited linewidth, has an additional unidentified broadening component of 1 GHz. To realize spin-selective excitation, the non-radiative relaxation and this additional broadening mechanism need to be understood and eliminated.

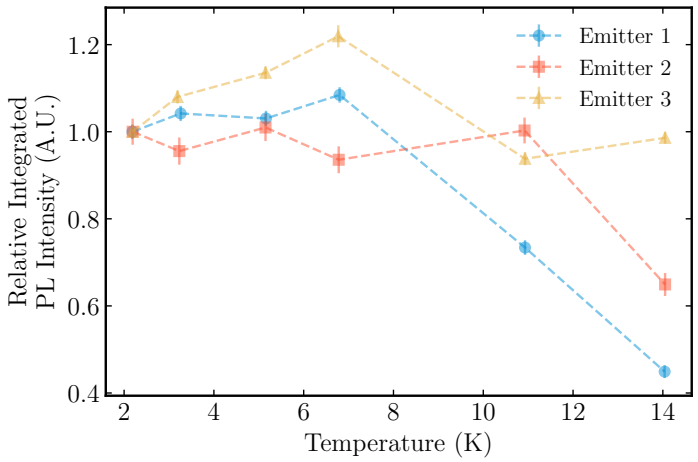

Figure 6.7: Temperature dependence of the integrated PL intensity for emitters 1, 2, and 3. For each emitter we normalize all data to their lowest temperature values. Excitation is 3.44 eV.

6.6 Conclusion

In summary, we have isolated and characterized single In donors in ZnO, revealing charge-stable emission with near lifetime-limited linewidths which underscore the potential for single In donor spin qubits. Through resonant excitation and magneto-PL, we identify three emitters as In donors. The isolated donors exhibit near lifetime-limited linewidths with charge-stable emission. The estimated 10 % radiative efficiency motivates future dedicated studies on surface damage and understanding of surface effects on near-surface quantum emitters in ZnO. However, ZnO is a fairly new quantum defect host and the relative ease of single donor isolation and observed signal recovery after one annealing step is promising. Additionally, the FIB-robust optical signal suggests FIB is appropriate for optical device fabrication in ZnO, an important requirement due to the monolithic nature of ZnO and the need for features small/comparable to the 369 nm transition wavelength. Finally, we note that this work further motivates the need for high purity ZnO material to reduce the band-edge luminescence from unintentional dopants.

Chapter 7

PROGRESS TOWARDS FREQUENCY TUNING OF DONOR ENSEMBLES

7.1 Introduction

To realize heralded entanglement of single spin qubits via photons as described in Sec. 1.1.1, indistinguishable photons are required. In bulk samples, as we saw in Chapter 5, the inhomogeneous broadening is in the order of a few GHz, similar to the homogeneous broadening. Moreover, as we saw in Chapter 6 where we were able to isolate single emitters via FIB milling, varying local strain environments – a result related to the fabrication process – lead to large inhomogeneous broadening with central frequency deviations as far as 100 GHz, much larger than the single emitter linewidth of 3-6 GHz. This inhomogeneity challenge is prevalent in most optically active solid state qubits, including color centers, quantum dots, and rare earth doped solids [158–161]. Two common solutions of tuning the emission frequency include electric field tuning via the Stark effect and strain field tuning via electro-mechanical coupling [162, 163]. Color centers in diamond and divacancies in SiC have demonstrated Stark tuning range of $\mathcal{O}(10)$ GHz, while InAs/InP quantum dots have demonstrated tuning ranges up to 1.2 THz [163–167]. The symmetric effective mass wavefunction of the donor and the donor bound exciton in ZnO means that this defect will primarily be affected by the electric field to second order in the applied electric field. Despite this, the large size of the donor bound exciton wavefunction may allow for shifts on the order of 100 GHz.

Here, we attempt to employ the Stark effect to frequency tune implanted In ensembles by fabricating interdigitated electrodes on a bulk ZnO substrate. In Sec. 7.2 we present a theoretical model to estimate a frequency tuning range of 100 GHz. Section 7.3 describes the device design and fabrication challenges. Section 7.4 details the fabrication process

that resulted in the first generation of Stark tuning devices. In Sec. 7.5, we present device measurements indicating that the observed shift and line broadening is due to heating and not the electric field. Finally, Sec. 7.6 concludes with a discussion on current challenges and future steps towards frequency tuning shallow donors in ZnO.

7.2 Stark effect on the donor – donor-bound exciton transition

Since both the D^0 and the D^0X states can be approximately described as effective mass wavefunctions, we can estimate the effect of an applied DC electric field on these states by drawing parallels with the DC Stark effect in hydrogen. In the presence of electric field $\mathcal{E}$, the 1s state of the hydrogen-like state will not be affected in the first order of $\mathcal{E}$ because the state is spherically symmetric. Instead, the field will induce a dipole moment on the state, which will be affected by the electric field in the second order. This perturbation on charge q under the electric field potential $V = q\mathcal{E}z$, with the electric field parallel to the z axis, yields an energy shift of

$$\Delta E_s = -\frac{\alpha_s \mathcal{E}^2}{2}, \tag{7.1}$$

where α_s is the state polarizability and is given by [110]

$$\alpha_s = -4\pi\epsilon_0 \times 2q^2\epsilon \sum_{k\neq 1s} \frac{\left|\langle \psi_k \left| z \right| \psi_{1s} \rangle\right|^2}{E_{1s} - E_k} = 4\pi\epsilon\epsilon_0 \times 2Ca_s^3, \tag{7.2}$$

where ϵ_0 and ϵ have their usual meaning, a_s is the Bohr radius, $|\psi_k\rangle$ the kth eigenstate's wavefunction with energy E_k, and $|\psi_{1s}\rangle$ the ground state wavefunction with energy E_{1s} and C a constant related to the sum. A hydrogen-like system that does not account for short-range chemical potential of the impurity is described by a radial wavefunction given by

$$\psi_{\mathrm{EM},e}(r) = \frac{2}{a_{\mathrm{EM}}^{3/2}} e^{-\frac{r}{a_{\mathrm{EM}}}}. \tag{7.3}$$

For this wavefunction, the summation constant C is found analytically (using only the 1s orbital state) to be $C_{\mathrm{EM,anal}} = 9/4$ [168]. However, the D^0 and D^0X-e radial wavefunctions that take into account the short-range chemical potential of the impurity and the D^0X-h

radial wavefunction that is approximated by the Kratzer potential, discussed in detail in App. A.1, take the form

$$\psi_s(r) = \sqrt{\frac{2^{2Q_s+1}}{\Gamma\left(2Q_s+1\right)a_s^{2Q_s+1}}} r^{Q_s-1} e^{-\frac{r}{a_s}}, \tag{7.4}$$

where Q_s is a unitless correction factor. There is no straightforward analytical expression for the polarizability. We can instead approximate the hydrogen polarizability using a classical uniform charge distribution of radius R_s around the nucleus, yielding $\alpha_s \approx R_s^3$ [169], and choose R_s as the RMS radius

$$R_s = \sqrt{\langle \psi_{1s} | r_s^2 | \psi_{1s} \rangle} \overset{\text{Eq. 7.3}}{=\!=} \sqrt{3a_s^2}, \tag{7.5}$$

to get

$$\alpha_{s,\text{EM}} \approx R_s^3 = 4\pi\epsilon\epsilon_0 \times 3^{3/2} a_s^3 = 4\pi\epsilon\epsilon_0 \times 5.196 a_s^3 \tag{7.6}$$

or $C_{\text{EM,approx}} = \sqrt{3}^3/2$. Therefore, this approximation yields a C value slightly higher than the analytical solution by a factor of $C_{\text{EM,anal}}/C_{\text{EM,approx}} = \sqrt{3}/2$. Using Eq. 7.4 in Eq. 7.5 and correcting for the factor mismatch of the approximation, we find from the effective mass wavefunction, we obtain an approximate polarizability of

$$\alpha_s \approx 4\pi\epsilon\epsilon_0 \times 2 \left(\frac{\sqrt{3}}{4} \sqrt{(1+Q_s)(1+2Q_s)/2}^3 \right) a_s^3. \tag{7.7}$$

Therefore, we can estimate the energy shift for all three individual states (D^0, D^0X-e, and D^0X-h) using Eq. 7.7 in Eq. 7.1. The overall $D^0 \leftrightarrow D^0X$ transition shift will be given by difference between the total D^0X energy shift and the D^0 energy shift, or

$$\Delta E_{\text{tot}} = \Delta E_{D^0\text{X-h}} + 2 \times \Delta E_{D^0\text{X-e}} - \Delta E_{D^0}. \tag{7.8}$$

As shown in Figure 7.1, the largest contribution to the frequency shift comes from the D^0X hole, which is expected since the hole wavefunction is much larger than the electron wavefunctions (Fig. A.1). We must also note that the D^0X-h model is also the most questionable, because it does not take into account interactions between e-e nor e-h. Despite this,

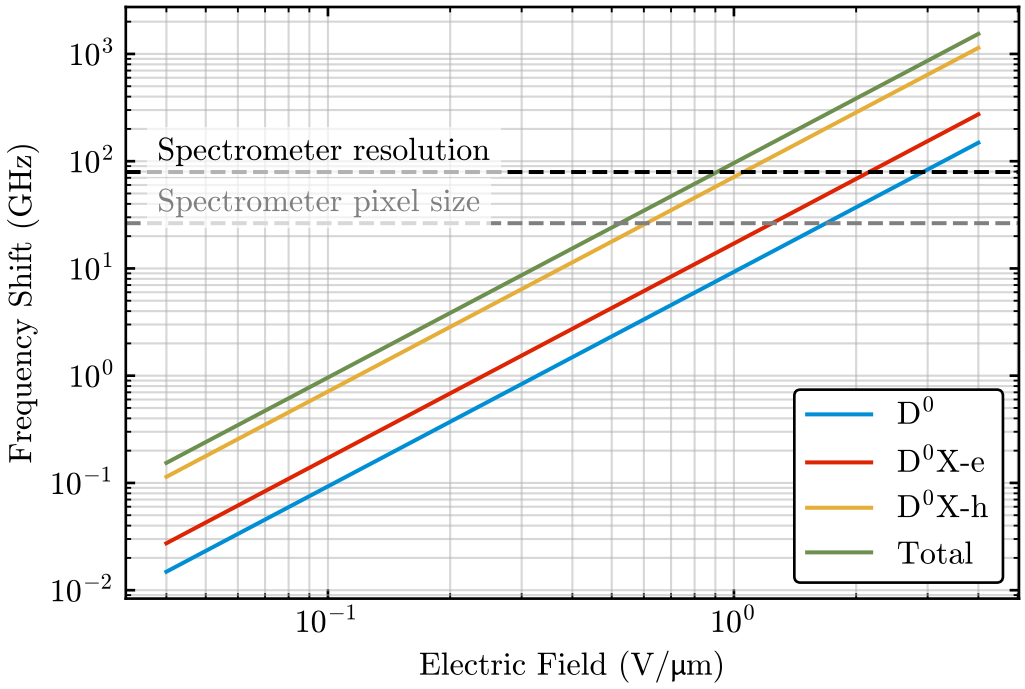

Figure 7.1: Frequency shifts of In^0, In^0X-e, and In^0X-h states and the overall $In^0 \leftrightarrow In^0X$ transition shift as a function of electric field amplitude present on the In defect site. Horizontal lines mark the spectrometer resolution of 80 GHz and the spectrometer pixel size of 26 GHz.

based on results in Chapter 5, this model successfully predicts the $D^0 \leftrightarrow D^0X$ inhomogeneous broadening within less than an order of magnitude. Therefore, in this approximation, we expect the $In^0 \leftrightarrow In^0X$ transition shift range to be in 100s GHz near a field of 1 V/μm. These fields are achievable, with ZnO breakdown electric fields ranging between 1 V/μm and 20 V/μm depending on the crystal quality and growth method [170, 171]. Experimentally, we expect the shifts to be resolvable in PL spectra near the 0.5 V/μm - 1 V/μm limit, while 1 GHz shifts – resolvable in PLE spectra – are expected near 0.1 V/μm. Therefore, PLE is a better measurement for this experiment.

Since ZnO is a good piezoelectric material, the applied electric field will also result in strain that can further tune the frequency. This theoretical approximation does not take

into account any strain effects.

We also note that in Sec. 4.4 we estimated the longitudinal spin relaxation rate using the non-corrected hydrogen-like polarizability. If we take into account the correction from Eq. 7.7, we find that the rate constant a in $\Gamma_{\downarrow\uparrow} = aB^5$ for Ga reduces from $0.080\,\mathrm{s}^{-1}\,\mathrm{T}^{-5}$ to $0.070\,\mathrm{s}^{-1}\,\mathrm{T}^{-5}$ in the Faraday geometry. Similarly, for In in the Faraday geometry, it reduces from $0.040\,\mathrm{s}^{-1}\,\mathrm{T}^{-5}$ to $0.032\,\mathrm{s}^{-1}\,\mathrm{T}^{-5}$.

7.3 Device design

For this application, we fabricate on-chip planar interdigitated capacitors, where the electric field is perpendicular to adjacent digits (strips) within the x-y plane (Fig. 7.2 and Fig. 7.3). This geometry allows for a straightforward fabrication process on a single substrate surface. An optical image of three fabricated devices is shown in Fig. 7.2. A potential difference is applied at two opposing pads. PL spectra are measured between the digits as illustrated in Fig. 7.2.

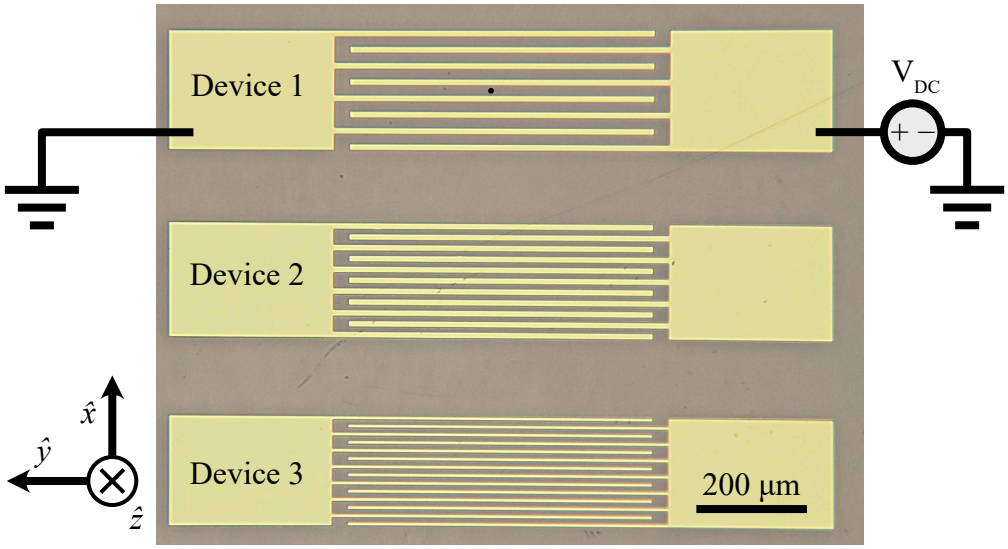

Figure 7.2: Optical image of fabricated devices with three different sets of design parameters, alongside the electric circuit used for the experiments. A black dot near the center of Device 1 marks an example location that was probed optically.

Resistive contacts may result in significant reduction of the applied electric field within the substrate. However, fabrication of non-resistive Schottky contacts on ZnO has been historically challenging [172, 173]. Commonly used methods such as gold evaporation are only partially successful, often leading to resistive ohmic contacts [174] while exhibiting low adhesion even with the use of adhesive metal layers such as titanium. Recent efforts showcase low resistivity contacts by sputtering iridium in the presence of oxygen-argon plasma [175]. While this method is highly successful, it may damage the surface of the sample. Due to the limited supply of high quality ZnO, such methods become prohibitive. Instead, we cover the

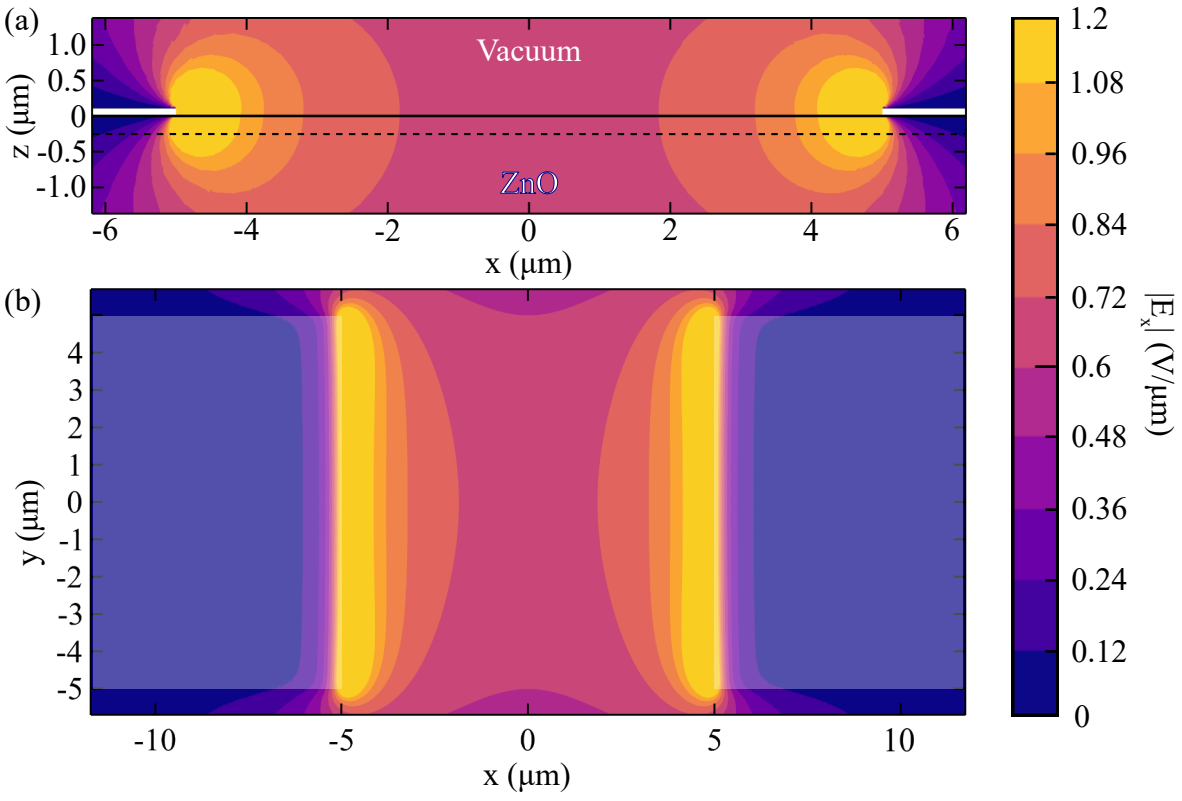

Figure 7.3: COMSOL electrostatics simulation results. Applied voltage differential is 10 V. (a) Electric field amplitude parallel to the $\hat{x}$ axis in the $y = 0\,\mu\text{m}$ slice. The white boxes denote the metal contacts. The dotted line denoted the target implantation depth. (b) Electric field amplitude parallel to the $\hat{x}$ axis in the $z = -0.25\,\mu\text{m}$ slice. The semi-transparent white boxes denote the metal contacts on the sample surface.

sample with a 10 nm layer of SiO_2 which (1) acts as a protective layer for the ZnO substrate, (2) acts as an insulating layer between the substrate and the metal contacts, (3) enables the use of metal evaporation using e.g., chromium (adhesive) and gold (conductive).

We perform an electrostatic simulation for the proposed design using COMSOL, where ZnO and SiO_2 are assumed to be a perfect dielectrics, while the effects of impurity charges and screening are ignored. Fig. 7.3 shows electric field amplitude for an electrode distance of 10 µm and an applied voltage differential of 10 V. We expect that the electric field scales linearly with the applied voltage and inversely linearly with the electrode distance. For these design parameters, we expect the electric field in between the two strips at a depth of 250 nm to be 0.6 V/ µm, which is well within electric fields that theoretically yield 100 GHz tuning.

7.4 Fabrication Process

Prior to fabrication, we implant In defects via ion implantation. The target implantation fluence is $1 \cdot 10^{11}\,\mathrm{cm}^{-2}$ and the expected mean implantation depth is ~ 250 nm. We anneal the sample at 700 °C in an O_2 atmosphere for 1 hour to heal the ion impact damage and to incorporate the implanted defects in Zn sites [81]. To fabricate the Stark-tuning devices, we first remove any contaminants from the surface. We start with a sequence of 5-minute ultrasonic baths in acetone and then IPA, followed by drying with nitrogen gas. Next, we

Device	Strip width (µm)		Distance (µm)	
	Designed	Fabricated	Designed	Fabricated
1	10	11	20	19
2	10	11	10	9
3	5	6.7	10	8.3

Table 7.1: Designed and fabricated dimensions for each device. The inter-strip distance (strip width) is consistently smaller (larger) for all fabricated devices because the sample was overdeveloped.

etch the sample with a ∼0.028% dilute hydrocholoric acid (HCl) solution (pH ≈ 1.5–2) for 30 seconds. With a clean surface, we deposit 10 nm of silicon dioxide (SiO_2). The sample is then spin-coated with a bi-layer of PMMA electron beam resist and a coat of aquaSAVE. The PMMA bi-layer with different polymer masses helps prevent sticky sides during lift-off, while aquaSAVE creates a conductive layer for excess charges to escape during the electron-beam write. After successful spin-coating, we write the pattern with e-beam lithography (beam width of 120 nm as per the device parameters), and develop in an IPA/water mixture for 2.5 minutes. Metals are deposited with an electron beam evaporator: a 10-nm adhesion layer of titanium, and then a 100-nm conductive and non-oxidizing layer of gold. Lastly, we lift-off the remaining resist with a 12 hour acetone bath. Table 7.1 shows the device parameters corresponding to the fabricated devices in Fig. 7.2.

7.5 Results

We characterize the behavior of the $In^0 \leftrightarrow In^0X$ in the presence of an applied voltage via PLE measurements using a DC source measurement unit (Keithley SMU 2450). Fig. 7.4a shows PLE measurements using Device 2 in a liquid helium immersion environment at 1.8 K. We observe a central frequency shift up to 30 GHz, much smaller than the theoretically expected 300 GHz, line broadening, and an overall intensity drop. In addition, increasing applied voltage results in very high leakage current, up to 7 mA at 30 V (Fig. 7.4b), and increase of the superfluid helium bath temperature in which the sample is immersed from 1.8 K to 2 K. The temperature is measured 3 inches above the sample. Higher voltages could not be reached as the devices breaks down. Frequency shift, line broadening, and intensity decreases are all behaviors that can be attributed to a significant temperature increase. This temperature increase could be the result of Joule heating due to the large leakage currents.

To determine whether the observed behavior is related to temperature, we (1) measured emitted PL under CW above-band excitation as a function of applied voltage and (2) compared the linewidth as a function of frequency shift between voltage dependent measurements and temperature dependent measurements on implanted In ensemble from chapter 5. As we

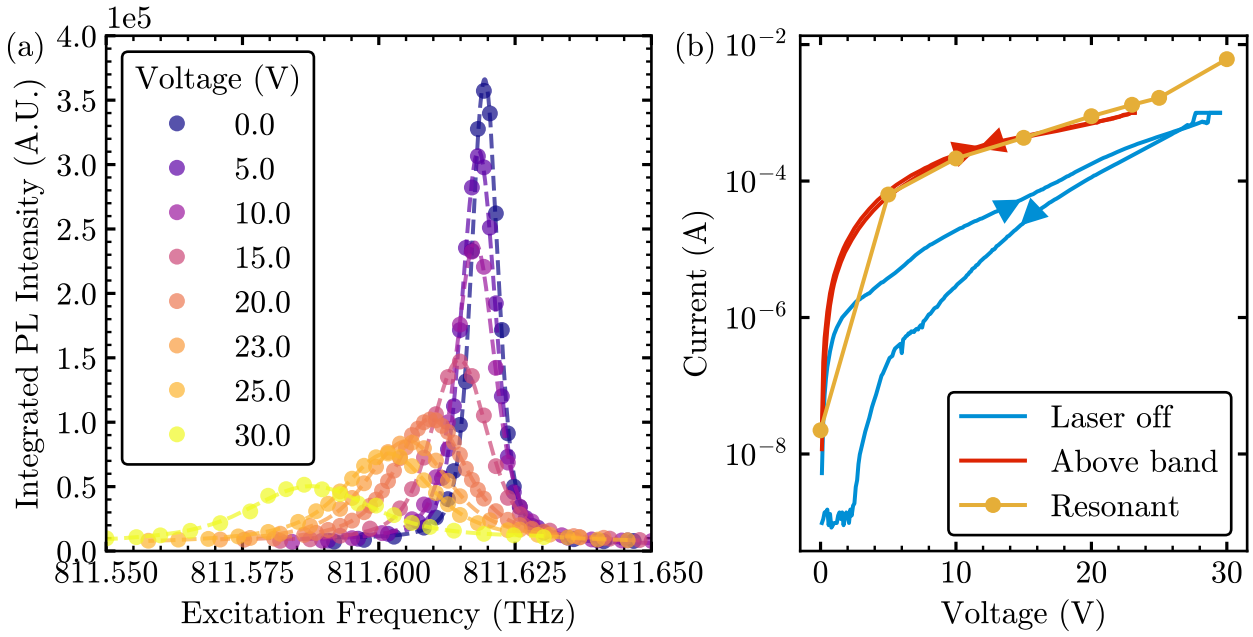

Figure 7.4: (a) PLE of implanted In ensemble as a function of applied voltage under CW excitation with 150 nW of power on Device 2. (b) Current - Voltage (IV) measurement of Device 2. The blue line depicts the device behaviour without illumination. The red line depicts the device behavior under above band CW excitation at 360.5 nm and 1 µW. During these measurements the voltage was changed by 0.1 V every 0.1 s. The arrows indicate the voltage change direction. The yellow line with circles depicts the mean device behavior under resonant CW excitation with 150 nW for each applied voltage used in (a). For both plots, the sample is immersed in liquid helium bath with base temperature of $T = 1.8$ K.

see in chapter 5, an increase in temperature also results in the increase of $D^0 \leftrightarrow D^0X^*$ luminescence. Figure 7.5 shows PL spectra for a range of voltages where a significant increase in $D^0 \leftrightarrow D^0X^*$ PL for all In, Ga, and Al donors is observed. This behaviour could be attributed to either a change in the transition oscillation strength in the presence of electric field or a temperature increase on the sample. Figure 7.6 depicts the frequency shift as a function of additional linewidth broadening for voltage variation measurements with Devices 1 and 2, as well as temperature variation measurements performed with implanted In ensembles at a depth of 200 nm from Fig. B.2 for three different implantation fluences (0.8, 1.3 and $1.9{\cdot}10^{11}$ cm^{-2}). The temperature varying experiment suggests that increasing implan-

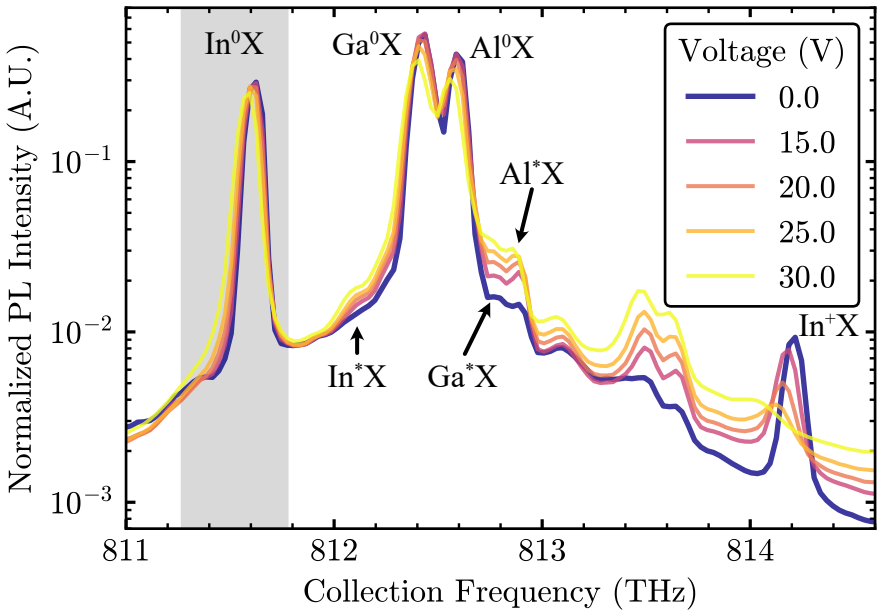

Figure 7.5: PL spectra with varying applied voltage under CW aboveband excitation with 1 µW of power. The intensity is normalized to the total counts of the In peak (within the light gray area). $T = 1.8\,\mathrm{K}$, immersed in superfluid helium bath.

tation fluence results in increasing linewidth broadening. The voltage variation data follow a behavior similar to the temperature variation data for the lower implantation fluences of $0.8{\cdot}10^{11}\,\mathrm{cm}^{-2}$ and $1.3{\cdot}10^{11}\,\mathrm{cm}^{-2}$, which is similar to the target implantation fluence for these devices. This comparison, albeit indirect, also indicates that the observed behaviour may be thermal in nature.

7.6 Discussion

The first Stark tuning device results suggest that the large leakage current results in large increase in temperature. Moreover, the observed frequency shift is comparable to frequency shifts related to a change in the band gap due to temperature. Therefore, there is no convincing evidence that the observed tuning is related to the Stark effect, but instead may be a result of Joule heating. These results indicate the applied electric field is screened by free carriers [176], the contact resistance of the electrodes is too high to allow a large

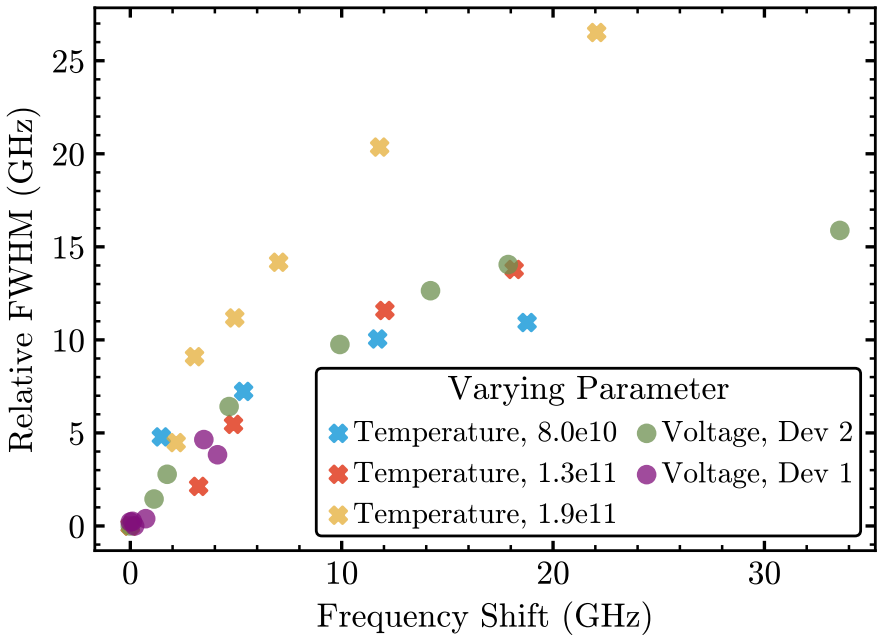

Figure 7.6: Full width at half maximum (FWHM) of PLE measurements relative to the lowest measured FWHM in each dataset as a function of the central transition frequency for two types of experiments: (1) with varying the applied voltage at 1.8 K and (2) with varying temperature with no applied voltage. The voltage dependent data are taken on Device 1 and Device 2. The temperature dependent data are taken from the temperature dependence measurements performed as part of Ch. 5 on implanted indium ensembles at a depth of 200 nm at three different fluences: $0.8{\cdot}10^{11}\,\mathrm{cm}^{-2}$, $1.3{\cdot}10^{11}\,\mathrm{cm}^{-2}$, and $1.9{\cdot}10^{11}\,\mathrm{cm}^{-2}$.

voltage drop within the substrate, and/or that the applied electric field may not affect the D^0 and D^0X states as expected. Future endeavors towards realizing frequency tuning of donor bound excitonic transitions in ZnO will focus on determining whether screening or some other physical effect prevents the electric field from reaching 250 nm in the substrate. Additionally, thicker dielectric layers between the electrodes and ZnO substrate could be used to suppress leakage current. If this limitation cannot be surpassed with a different device geometry, strain tuning could be another viable option moving forward.

Chapter 8

SUMMARY AND OUTLOOK

An initial study of the shallow donor ensembles in ZnO in the context of quantum networks highlighted the promising spin properties of this defect by demonstrating all optical coherent spin control via the donor-bound exciton as well as long longitudinal spin relaxation times T_1 up to 100 ms at high magnetic fields (2-7 T) [54]. It was revealed that the spin-echo coherence time T_2 of 50 µs was limited by either instantaneous diffusion or ^{67}Zn nuclear spin diffusion. Therefore, isotopic and chemical purification, alongside microwave coherent spin control and single qubit isolation, are key challenges to enable optical quantum networks with this platform.

This result motivated us to further understand the interactions of the donor spins with their environment. We performed an extensive experimental study on the longitudinal spin relaxation time T_1 via optical manipulation of the donor spin state as a function of magnetic field, temperature, excitation photon energy, donor density, and donor species. We showed that our observations can be primarily explained by the combined effect of spin-orbit and electron-phonon couplings under an effective mass approximation of the donor envelop wavefunction. Small discrepancies between the experimental data and the theoretical prediction can be partially explained by the experimentally observed donor density dependence, whose physical mechanism is still elusive. The longest observed T_1 is 480 ms at 1.75 T and 1.5 K, and even longer values can be achieved at smaller magnetic fields. Due to the large electron g factor resulting in an electron spin energy splitting of $\sim 27h$ GHz/T, working at lower magnetic fields ($\sim$0.3 T) will also enable the use of widely available microwave equipment for coherent microwave spin control at the frequency range of 5-10 GHz (instead of the much more technologically niche range of 25-100 GHz we need for magnetic fields between 1 T and

3 T). However, high fidelity optical spin initialization at lower magnetic fields is challenging because (1) increased overlap of the lines at low fields (near 20 GHz) and leakage of excitation beam retroreflection reduce the optical pumping contrast, and (2) the overall collected sideband PL is low, resulting in low contrast between the signal and the background. In future endeavors, increasing the overall collected PL can be achieved by using side-excitation as described in Sec. 4.9 to collect the ZPL instead of the sideband PL with bulk optics. Eventually, using photonic integrated circuits will allow for efficient excitation and collection on the ZPL while minimizing leakage of the excitation beam into the collection path.

After advancing our understanding of the spin properties, we studied the donor ensemble optical properties, and more specifically the optical linewidth and optical depth. Our in-depth investigation of the PL linewidth from emitters near the Zn-face reveals a homogeneous linewidth of 4 GHz, and similar inhomogeneous broadening, only one to two orders of magnitude larger than the Fourier lifetime limit. We found that the dominant inhomogeneous broadening mechanism is related to the disordered isotopic environment of the defect due to the Zn and O isotope mass variation. The large homogeneous linewidth may be caused by either instantaneous spectral diffusion due to D^0X-D^0X interactions or environmental charge variation due to nearby impurities. This further highlights the importance of isotopic and chemical purification of ZnO samples. Moreover, we found that ensembles with donor concentrations of $\mathcal{O}\,(10^{15}\,\mathrm{cm}^{-3})$ in a 300 µm-thick sample can yield optical depths of $\mathcal{O}\,(100)$ without significant additional linewidth broadening. However, they also reveal large background absorption with an imaginary refractive index of $\sim 10^{-4}$ due to the proximity of the absorption line to the band edge. While such large optical depths can enable solid-state optical quantum memories with this platform, the large background absorption may limit the efficiency with which stored information is retrieved. In addition, the high absorption limits the quality factor of donors integrated in photonic cavities to $Q = 1.7 \cdot 10^4$. For using this platform in optical quantum communication protocols as-is, indistinguishable photons can be generated with a modest Purcell factor of 100. Such Purcell factors would require small mode volumes, achievable with photonic crystal cavities [148]. Alternatively, defect

emission from ZnO could be coupled to photonic devices fabricated with a large band gap material to ensure low transmission losses at 369 nm. Traditional photonic device fabrication on the surface of bulk ZnO substrates will be similarly limited by transmission losses due to direct contact with the ZnO host, while the large refractive index of ZnO near the band edge (2.7-2.9) severely limits the material choices. However, with further advancements in ZnO material and defect engineering, defect emission from ZnO nanostructures could be coupled to low-loss photonic devices while minimally interacting with the ZnO host. This can be achieved, for example, by using donors in ZnO nanoparticles that are evanescently coupled to a cavity fabricated from a low-loss material, or by utilizing tapered ZnO nanobeams that waveguide the defect emission to a low-loss material [177–179].

Having established the favorable spin and optical properties of donor ensembles, we focused on the isolation of single donors. Even in the best commercially available ZnO substrates, the high *in situ* donor concentrations severely limit our ability to isolate single emitters in bulk substrates. Instead, we milled a thin slice of ZnO out of the bulk substrate using a focused ion beam. We were able to spatially and spectrally isolate single emitters that are intensity and frequency stable. We identified these emitters as In donors via magneto-PL and resonant excitation. The emission frequency was inhomogeneously broadened by 100 GHz, which was attributed to strain variation across the sample. Moreover, the sideband PL emission was riddled with background PL emission from other *in situ* dopants. The emitter linewidth of 3-6 GHz is comparable to the homogeneous linewidth of bulk emitters and is less than two times larger than the lifetime-limited linewidth. However, the 10-fold reduction in emitter lifetime indicated a low radiative efficiency and is attributed to non-radiative recombination to surface defects. Despite this, the optical properties of the donors were mostly recovered after an invasive FIB process, indicating a promising step toward optical quantum network applications with single spin qubits in ZnO integrated with FIB-milled photonic devices. Finally, this study underscores some of the challenges that lie ahead: (1) understanding and eliminating surface effects that reduce the radiative lifetime, (2) understanding and eliminating the effects that persistently broaden the linewidth both in bulk and single

emitters, and (3) chemically purifying the substrate to reduce background PL from of other dopants.

Finally, to address the observed inhomogeneity of single emitters, we reported on progress toward frequency tuning via the Stark effect. We theoretically predicted that the tuning range could reach 100 GHz. The first fabricated Stark tuning device on ZnO indicates that large leakage currents result in thermal tuning of the emission, which is not desirable due to the degradation of the spin and optical properties at higher temperatures. There was no clear evidence of additional electric field tuning, which was attributed to field screening from moving charges. Albeit unsuccessful, these insights are useful for future research endeavors, where we might gain a better understanding of the electric field behavior in the material.

Overall, we demonstrated favorable spin and optical properties for both ensemble and single donors in ZnO for optical quantum network applications. We described some of the mechanisms behind the interactions of the donors with their environment, and gathered data that may eventually lead to discoveries of additional phenomena that govern this platform. Additionally, we identified the key areas of focus for future exploration with this platform:

1. Isotopic and chemical purification are the most prevalent challenges. Isotopic purification of the host lattice is expected to lead to longer spin coherence times, and narrower inhomogeneous broadening. Chemical purification is expected to result in longer longitudinal spin relaxation times, longer spin echo times and narrower homogeneous linewidth. It may also enable new methods of introducing single defects in bulk substrates (e.g., via implantation) and higher fidelity control of single qubits. While research efforts on ultra high purity bulk ZnO growth have stalled in the last decade, the development of ultra high purity of MBE ZnO layers, an active area of research, may lead to ultra high purity and isotopically uniform substrates.

2. Photonic device integration of donors can help combat low PL collection that originates from (i) collecting the 10 % sideband emission instead of the 90 % ZPL, and (ii) the large refractive index of 2.7 that only allows 3 % of the total emitted PL to escape the

sample. Photonic integration can enable concurrent excitation and collection at the ZPL wavelength while collecting up to 50 % of the emitted PL (e.g., via nanopillars or grating couplers).

3. Non-radiative recombinations to surface defects result in even lower PL collection. While photonic integration enables enhanced PL collection, the defects will be much closer to surface. Therefore, identifying and eliminating this mechanism is paramount to efficient spin initialization and read-out.

4. The strain-induced inhomogeneity remains a challenge in micrometer or submicrometer sized devices. A robust method of tuning the transition frequency with a tuning range of 100 GHz is important for future implementation of entanglement protocols via photons. While our attempt in electric field tuning was unsuccessful, future devices utilizing thicker dielectric layers may be more successful. Alternatively, strain tuning may be another viable option.

5. FIB milling enables the in the successful isolation of single emitters but it difficult to scale. Alternative routes include isolation via low fluence implantation in purified samples, or growth of nanostructures such as nanoparticles and nanorods.

6. While all optical coherent spin control of prior works was instrumental in motivating this thesis, microwave coherent spin control is an essential to obtaining higher fidelity control over larger rotation angles.

Advances in the above areas will significantly increase the performance of this platform and eventually enable the entanglement of single donor spin qubits in ZnO. This may also enable the realization of heterogeneous quantum networks between donors in ZnO and trapped $^{171}Yb^{+}$ due to their similar emission frequencies and radiative lifetime [134]. Altogether, the insights gained from this research offer valuable directions for continued exploration of the ZnO-based shallow donor spin qubit in the field of quantum information science.

Appendix A

THEORETICAL DERIVATIONS

A.1 Envelope wavefunctions through the effective mass approximation

Originally published in part in the Supplemental Material of [97]: V. Niaouris, S. H. D'Ambrosia, C. Zimmermann, X. Wang, E. R. Hansen, M. Titze, E. S. Bielejec, and K.-M. C. Fu, "Contributions to the optical linewidth of shallow donor-bound excitonic transition in ZnO", Optica Quantum **2**, 7–13 (2024).

A.1.1 Donor electron

Following Ref. [180], the radial part of the electron wavefunction in a hydrogen-like system is given by

$$R_{\mathrm{EM},e}(r) = \frac{2}{a_{\mathrm{EM}}^{3/2}} e^{-\frac{r}{a_{\mathrm{EM}}}}, \tag{A.1}$$

where a_{EM} is the effective mass (hydrogenic) Bohr radius. However, to account for the short-range chemical potential of each impurity, we can utilize the central-cell corrected radial envelope wavefunction, namely

$$R_{\mathrm{D}^0,e}(r) = \sqrt{\frac{2^{2Q_{\mathrm{D}}+1}}{\Gamma\left(2Q_{\mathrm{D}}+1\right) a_{\mathrm{D}}^{2Q_{\mathrm{D}}+1}}} r^{Q_{\mathrm{D}}-1} e^{-\frac{r}{a_{\mathrm{D}}}}, \tag{A.2}$$

where a_{D} is the nominal donor Bohr radius, Q_{D} is related to the ratio of the effective mass binding energy ($E_{b,\mathrm{EM}}$) to the donor binding energy ($E_{b,\mathrm{D}}$), and Γ is the gamma function. These are given by

$$a_{\mathrm{D}} = \sqrt{\frac{\hbar^2}{2m_e^* E_{b,\mathrm{D}}}}, \qquad Q_{\mathrm{D}} = \sqrt{\frac{E_{b,\mathrm{EM}}}{E_{b,\mathrm{D}}}}, \quad \text{and} \quad E_{b,\mathrm{EM}} = \frac{m_e^*}{m_e}\frac{\epsilon_0^2}{\epsilon_{\mathrm{ZnO}}^2} R_y \left(1 + 0.72\gamma^2\right), \tag{A.3}$$

where R_y is the Rydberg energy, m_e (m_e^*) is the free (effective) electron mass, ϵ_0 (ϵ_{ZnO}) is the static dielectric permittivity in vacuum (ZnO), and γ is a small parameter related to crystal anisotropy [76]. The donor binding energy can be calculated by experimentally determining the transition energies for the transitions $\mathrm{D}^0(2\mathrm{s}) \leftrightarrow \mathrm{D}^0\mathrm{X}$ and $\mathrm{D}^0(2\mathrm{p}) \leftrightarrow \mathrm{D}^0\mathrm{X}$ [76], and are listed in Table 2.4. It must be noted that we have modified the wavefunction pre-factor taken from Ref. [180] so that Eq. A.2 is properly normalized to 1 when integrated in all space.

For a purely effective mass impurity, the expected electron radius is given by

$$\langle r_{\mathrm{EM}} \rangle = 3a_{\mathrm{EM}}/2. \tag{A.4}$$

However, the center-cell corrected wavefunction yields an expected electron radius given by

$$\langle r_{\mathrm{D}} \rangle = \frac{3}{2}\tilde{a}_{\mathrm{D}} = (\frac{1}{2} + Q_{\mathrm{D}})a_{\mathrm{D}}, \tag{A.5}$$

which results in an effective D^0 electron Bohr radius of

$$\tilde{a}_{\mathrm{D}} = \frac{2Q_{\mathrm{D}} + 1}{3}a_{\mathrm{D}}. \tag{A.6}$$

The new effective Bohr radius, similar to the hydrogen Bohr radius, is an indicator of how the central cell correction modifies the wavefunction. Another metric for the modification is the radius at which the probability density is maximized, namely

$$r_{\mathrm{D}}^{\mathrm{max}} = Q_{\mathrm{D}}a_{\mathrm{D}}, \tag{A.7}$$

with the radial probability density given by

$$P_r(r) = \int |R(r)|^2 \, r^2 dr. \tag{A.8}$$

We can see that for the effective mass impurity, where $Q_{\mathrm{D}} = 1$, the effective and maximum Bohr radii are the same. However, for $Q_{\mathrm{D}} < 1$, the effective radius will take larger values than the maximum radius, while $Q_{\mathrm{D}} > 1$ the effective radius will take values smaller than the maximum radius. This means that the wavefunction keeps its mean value closer the effective

mass equivalent than the maximum value and is skewed more the further Q_{D} is from 1. The nominal, effective and maximum donor Bohr radii are listed in Table A.1. Figs. A.1a shows the probability density in the ZnO crystal lattice for the pure effective mass donor, while Fig. A.1d shows the probability density of different donor species. From these figures it becomes apparent that the D^0 electron wavefunction occupies thousands of lattice sites, while the deeper the donor is in the band gap, the smaller its Bohr radius will be.

A.1.2 Donor-bound exciton

According to Ref. [181], the donor-bound exciton wavefunction can be approximated as a product of individual one-particle states; electron-electron and electron-hole interactions are neglected. In this picture, the two electrons are in 1s hydrogenic-orbitals (Eq. A.2) with modified Bohr radii and reside close to the the positively-charged impurity, while the positive hole binds to the net negative system. To determine the $\mathrm{D}^0\mathrm{X}$ wavefunction we need to determine $\mathrm{D}^0\mathrm{X}$-electron Bohr radius a_{2e} as well as the wavefunction of the $\mathrm{D}^0\mathrm{X}$-hole.

To find the $\mathrm{D}^0\mathrm{X}$-hole wavefunction, we need to start with the potential binding the hole, which is given by

$$V(r_h) = -\frac{e_c^2}{4\pi\epsilon_{ZnO} r_h}[1 - 2e^{-2r_h/a_{2e}}(1 + r_h/a_{2e})], \tag{A.9}$$

where r_h is the radial position of the hole and e_c is the elementary electric charge. The resulting hole potential is not easily solvable, but it can be approximated by the Kratzer potential,

$$V(r_h) \simeq -2D\left(\frac{b}{r_h} - \frac{b^2}{2r_h^2}\right), \tag{A.10}$$

with $D = se_c^2/8\pi\epsilon_{ZnO}a_{2e}$, and $b = ta_{2e}$. Here, t and s are fitting parameters for optimizing the mapping of the Kratzer potential (Eq. A.10) onto the original hole binding potential (Eq. A.9) near the potential minima, taking the values $t = 1.337$ and $s = 1.0136$ [181]. The normalized ground state solution to the Schrondiger's equation with the Kratzer potential [182, 183] is given by

$$R_{\mathrm{D}^0\mathrm{X},h,n_h=0,l_h=0}(r_h) = \sqrt{\frac{2^{2\Lambda_{00}+1}}{\Gamma\left(2\Lambda_{00}+1\right)a_h^{2\Lambda_{00}+1}}} r_h^{\Lambda_{00}-1} e^{-\frac{r_h}{a_h}}, \tag{A.11}$$

with a nominal D^0X-hole Bohr radius of

$$a_h = \sqrt{\frac{\hbar^2}{2m_h E_{h,00}}}. \tag{A.12}$$

Here, m_h is the hole effective mass in the crystal, n_h and l_h represent the radial and rotational quantum numbers of the hole, respectively, while the hole energy, $E_{h,n_h l_h}$, and $\Lambda_{n_h l_h}$ factor are defined as

$$E_{h,n_h l_h} = \frac{2m_h}{\hbar^2}\left(\frac{Db}{\Lambda_{n_h l_h}}\right)^2, \quad \Lambda_{n_h l_h} = n_h + \frac{1}{2} + \sqrt{\left(l_h + \frac{1}{2}\right)^2 + \frac{2m_h D b^2}{\hbar^2}}. \tag{A.13}$$

By rewriting the above in terms of the donor binding energy and nominal donor Bohr radius,

$$E_{h,n_h l_h} = \left(\frac{st}{\Lambda_{n_h l_h}}\right)^2 \frac{m_h}{m_e^*} E_{b,\mathrm{D}}, \quad \Lambda_{n_h l_h} = n_h + \frac{1}{2} + \sqrt{\left(l_h + \frac{1}{2}\right)^2 + st^2 \frac{m_h}{m_e^*}\frac{a_{2e}}{a_\mathrm{D}}}, \tag{A.14}$$

we see that we still need to calculate a_{2e} to define the hole wavefunction.

To find the D^0X-electron Bohr radius a_{2e}, we can write the total energy of the bound exciton $E_{\mathrm{D^0X}}$ as function of a_{2e} and minimize the total energy with respect to a_{2e}. The total D^0X energywith respect to the top of the valence band [181] for when the hole mass is isotropic [75] is given by

$$\begin{aligned} E_{\mathrm{D^0X},n_h l_h}(a_{2e}) = 2E_\mathrm{gap} + 2E_{b,\mathrm{D}}\left[\left(\frac{a_\mathrm{D}}{a_{2e}}\right)^2 - \frac{11}{8}\frac{a_\mathrm{D}}{a_{2e}}\right] \\ -2E_{b,\mathrm{D}}\left[\frac{s^2t^2}{2}\frac{m_h}{m_e^*}\left(n_h + \frac{1}{2} + \sqrt{\left(l_h + \frac{1}{2}\right)^2 + st^2\frac{m_h}{m_e^*}\frac{a_{2e}}{a_\mathrm{D}}}\right)^{-2}\right], \end{aligned} \tag{A.15}$$

where E_gap is the band gap energy. Although there is an analytic solution to minimizing Eq. A.15, it is too long to display here. Substituting for all known parameters, the resulting D^0X-electron Bohr radius is

$$a_{2e} = 1.2255 a_\mathrm{D}. \tag{A.16}$$

With this, we can now calculate the D^0X-electron wavefunction by substituting a_D for a_{2e} in Eq. A.2. Figure A.1b depicts the D^0X-electron probability density of the EM donor.

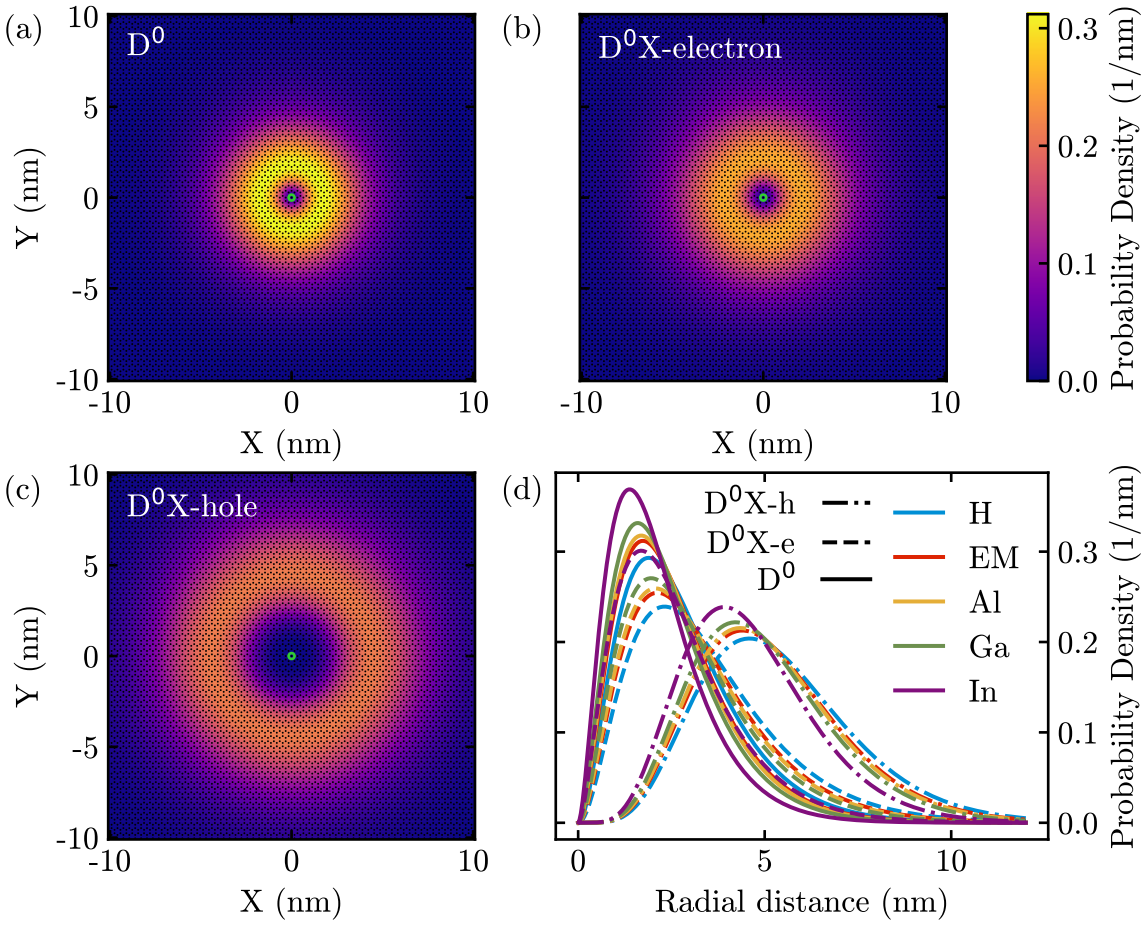

Figure A.1: (a), (b), (c) The calculated probability density of the effective mass impurity (EM) for the 1s state of the D^0, D^0X-electron and D^0X-hole, respectively. All figures share the same colorbar (top right). The green circle in the middle draws attention to the donor site. (d) The calculated probability density for H_i, EM, Al^0, Ga^0, and $In^0$for the 1s state of the D^0 (solid line), D^0X-electron (dashed line) and D^0X-hole (dash-dotted line), respectively.

Additionally, we can calculate the effective D^0X-electron Bohr radius $\tilde{a}_{2e}$ in the same manner as in Eq. A.6, or more simply, use the known donor Bohr radius,

$$\tilde{a}_{2e} = 1.2255\tilde{a}_D = 1.2255\frac{2Q_{\mathrm{D}}+1}{3}a_{\mathrm{D}}. \tag{A.17}$$

Similarly, the radial distance at which the probability density is maximized is given by

$$r_{2\mathrm{e}}^{\max} = Q_{\mathrm{D}}a_{2\mathrm{e}} = 1.2255Q_{\mathrm{D}}a_{\mathrm{D}} \tag{A.18}$$

To calculate the hole wavefunction, we can use Eq. A.11, with $\Lambda_{00} = 2.8342$ and $a_h = 0.8945a_{\mathrm{D}}$ (which were calculated by substituting all known parameters in Eq. A.14 and Eq. A.12, respectively). Figure A.1c depicts the D^0X-hole probability density of the EM donor. The resulting effective D^0X-hole Bohr radius is given by

$$\tilde{a}_h = \frac{2\Lambda_{00} + 1}{3} a_h = 2.2228 a_h = 1.9883 a_{\mathrm{D}}. \tag{A.19}$$

Similarly, the radial distance at which the probability density is maximized is given by

$$r_h^{\max} = \Lambda_{00} a_h = 2.5352 a_{\mathrm{D}} \tag{A.20}$$

The resulting D^0X-electron and D^0X-hole radii are listed in Table A.1.

Bohr Radii \ Species	$H_i(I_4)$	EM	$Al^0(I_6)$	$Ga^0(I_8)$	$In^0(I_9)$
Nominal, Donor (nm)	1.81	1.74	1.71	1.66	1.55
Effective, Donor (nm)	1.86	1.74	1.70	1.62	1.43
Maximum, Donor (nm)	1.89	1.74	1.69	1.60	1.38
Nominal, D^0X-electron (nm)	2.22	2.13	2.10	2.04	1.90
Effective, D^0X-electron (nm)	2.28	2.13	2.08	1.98	1.76
Maximum, D^0X-electron (nm)	2.32	2.13	2.07	1.96	1.69
Nominal, D^0X-hole (nm)	1.62	1.56	1.53	1.49	1.38
Effective, D^0X-hole (nm)	3.60	3.45	3.41	3.31	3.08
Maximum, D^0X-hole (nm)	4.59	4.40	4.34	4.22	3.92

Table A.1: Characteristic Bohr radii for different donor species including the pure effective mass donor. The effective mass donor is not observed, but the values are listed for comparison between the observed donors and the ideal hydrogen-like impurity. "Nominal" values correspond to the radius-related value in the exponential term of the wavefunction, "effective" values correspond to the radius related to the mean radius of the probability density compared to the effective mass mean, and "maximum" values correspond to the radius where the radial probability density takes its maximum value.

A.2 Oscillator strength and dipole moment

Originally published in part in the Supplemental Material of [94]: E. R. Hansen, V. Niaouris, B. E. Matthews, C. Zimmermann, X. Wang, R. Kolodka, L. Vines, S. R. Spurgeon, and K.-M. C. Fu, *Isolation of Single Donors in ZnO*, 2024, arXiv:2310.05806 [cond-mat.mes-hall]

Following Refs. [184, 185], we calculate the oscillator strength of the $D^0 \rightarrow D^0X$ transition from the $D^0X \rightarrow D^0$ emission lifetime in the zero-phonon line (ZPL) $\tau_{\mathrm{D,ZPL}}$. Specifically,

$$f_{ab} = \left(\frac{\mathcal{E}_0}{\mathcal{E}_{eff}}\right)^2 \frac{g_b}{g_a} \frac{2\pi\epsilon_0 m_e^* c^3}{n(\omega_{ba}) e^2 \omega_{ba}^2 \tau_{D,\mathrm{ZPL}}}, \tag{A.21}$$

where $\frac{\mathcal{E}_{eff}}{\mathcal{E}_0}$ refers to the effective field ratio that induces the transition, a and b correspond to the D^0 and D^0X states respectively, g_{i} is the degeneracy of the i state (2 for the D^0electron and 4 for the D^0X electron spin singlet and hole), ϵ_0 is the vacuum electric permittivity, m_e^* is the effective electron mass in ZnO, c is the speed of light in vacuum, $n(\omega_{ba})$ is the refractive index at the $D^0X \rightarrow D^0$ transition angular frequency, and ω_{ba} is the $D^0X \rightarrow D^0$ transition angular frequency. A good approximation for large-wavefunction emitters would be to set the effective field ratio equal to unity [184, Sec. 4c], which is valid for shallow donors in ZnO (see Sec. A.1). The emission lifetime to the ZPL can be estimated by taking into account the 1-LO and TES emission fractions ($C_{\mathrm{1LO}} = 1 - e^{-S}$ and $C_{\mathrm{TES}} = R_{\mathrm{TES/1LO}} C_{\mathrm{1LO}}$, where $R_{\mathrm{TES/1LO}}$ is measured experimentally from Fig. A.2), as well as the total radiative emitter lifetimes (see Table 2.4),

$$\tau_{\mathrm{D,ZPL}} = \frac{\tau_{\mathrm{rad}}}{C_{\mathrm{ZPL}}} = \frac{\tau_{\mathrm{rad}}}{1 - C_{\mathrm{1LO}} - C_{\mathrm{TES}}} = \frac{\tau_{\mathrm{rad}}}{1 - (1 + R_{\mathrm{TES/1LO}})(1 - e^{-S})} \tag{A.22}$$

This approximation does not take into account any other phonon replicas since they do not significantly contribute to the non-ZPL emission fraction. The corresponding emission fractions, ZPL lifetime, and oscillator strengths are listed in Table A.2.

Similarly, following Ref. [185], we can estimate the dipole moment via

$$\mu_{ba}^2 = \frac{3\epsilon_0 h c^3}{2\omega_{ba}^3 \tau_{\mathrm{D,ZPL}}}, \tag{A.23}$$

where h is the Planck constant. The resulting dipole moments are listed in Table A.2.

See App. A.3 for how the refractive index is measured.

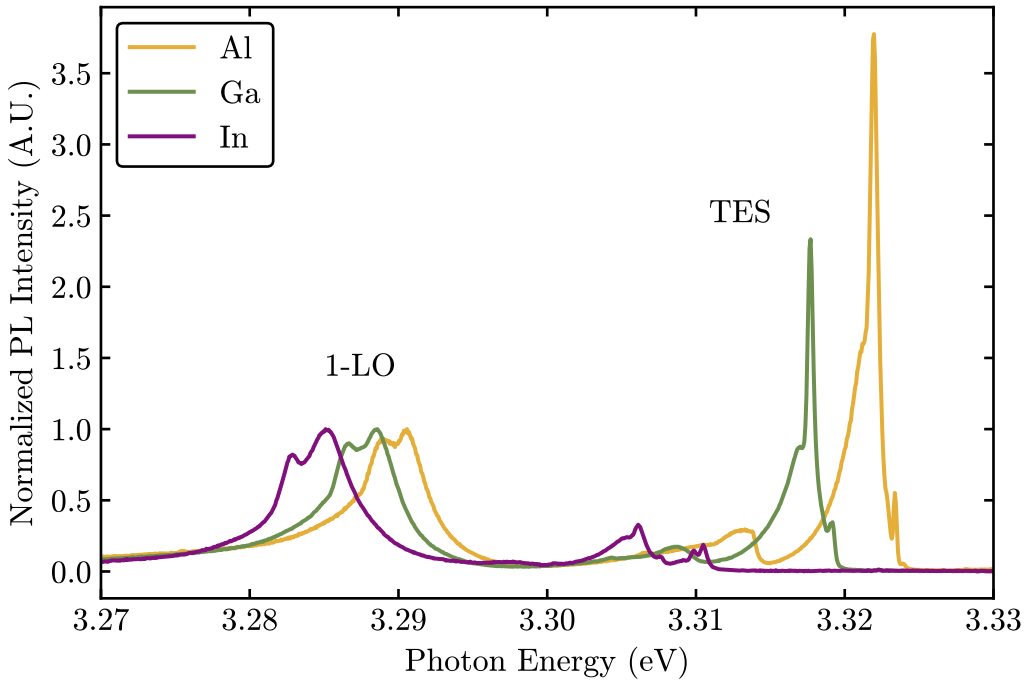

Figure A.2: PL spectra of the sideband TES and 1-LO lines for Al, Ga, and In under resonant CW excitation. The data are normalized to the maximum value of the 1-LO transition.

Transition	$Al^0 \leftrightarrow Al^0X$	$Ga^0 \leftrightarrow Ga^0X$	$In^0 \leftrightarrow In^0X$
TES/1-LO Intensity Ratio	0.95	0.59	0.21
Total Radiative Lifetime (ps)	750 – 860	800 – 1060	1050 – 1350
ZPL Radiative Lifetime (ps)	840 – 970	880 – 1170	1140 – 1470
Oscillator Strength	0.37 – 0.42	0.30 – 0.40	0.26 – 0.34
Dipole Moment (D)	12.9 – 13.8	11.7 – 13.5	10.5 – 11.9

Table A.2: Calculated oscillator strength and dipole moments for $Al^0 \leftrightarrow Al^0X$, $Ga^0 \leftrightarrow Ga^0X$, and $In^0 \leftrightarrow In^0X$.

A.3 Determination of optical depth and refractive index from transmission and reflection

Following Ref. [186], the optical depth αd, where α is the absorption coefficient and d is the sample depth, is given by

$$\alpha d = \ln\left(\frac{R_F T}{R - R_F}\right), \tag{A.24}$$

where R and T are the experimentally measured reflectance and transmittance, respectively and R_F is the surface reflectance, given by

$$R_F = \frac{K - \sqrt{K^2 - 4R\,(2 - R)}}{2\,(2 - R)}, \tag{A.25}$$

with $K = 2 + T^2 - (1 - R)^2$.

For small transmittance values, we can expand the surface reflectance as a Taylor series to the second order of transmittance as

$$R_F \simeq R\left[1 - \frac{T^2}{(1 - R)^2}\right]. \tag{A.26}$$

After some algebraic manipulations, the optical depth can be approximated by

$$\alpha d = \ln\left(\frac{(1 - R)^2}{T}\right). \tag{A.27}$$

Assuming that the sample thickness is known, we can easily calculate the imaginary refractive index from

$$\kappa = \frac{\lambda \alpha}{4\pi}, \tag{A.28}$$

where λ is the index of refraction. Following Ref. [186], we can calculate the index of refraction from

$$n = \frac{1 + R_F}{1 - R_F} + \sqrt{\frac{4R_F}{(1 - R_F)^2} - \kappa^2}. \tag{A.29}$$

For small κ, is simplified to

$$n \simeq \frac{2}{1 - \sqrt{R_F}} - 1 \tag{A.30}$$

Experimentally, we have determined that the reflection near the Al and Ga emission is approximately constant and equal to $R = 0.24 \pm 0.02$ (see Fig. A.3). From the transmission

measurements presented in Chapter 5, we estimate the real and imaginary refractive index of our samples near Al, Ga, and In resonances, presented in Table A.3.

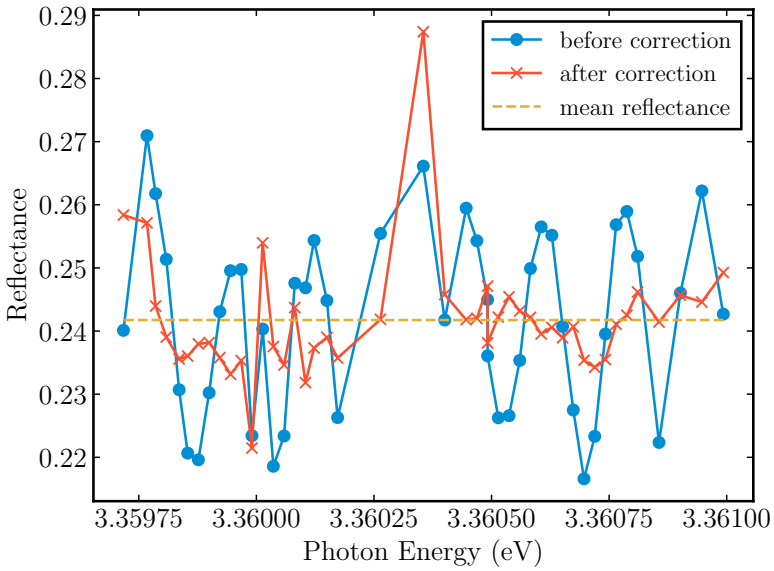

Figure A.3: Reflectance measurements as a function of excitation photon energy near the $Al^0 \leftrightarrow Al^0X$ and $Ga^0 \leftrightarrow Ga^0X$ transitions. An oscillatory pattern is observed which is attributed to the beam splitter with which the input power is monitored (see also App. A.4).

Transition	$Al^0 \leftrightarrow Al^0X$	$Ga^0 \leftrightarrow Ga^0X$	$In^0 \leftrightarrow In^0X$
Real refractive index (n)	2.9	2.9	2.7
Imaginary refractive index (k)	1.4×10^{-5}	1.3×10^{-4}	8×10^{-5}

Table A.3: Baseline refractive index for Al, Ga, and In bound excitonic transitions.

A.4 Excitation power correction

Originally published in the Supplemental Material of [97]: V. Niaouris, S. H. D'Ambrosia, C. Zimmermann, X. Wang, E. R. Hansen, M. Titze, E. S.

Bielejec, and K.-M. C. Fu, "Contributions to the optical linewidth of shallow donor-bound excitonic transition in ZnO", Optica Quantum **2**, 7–13 (2024).

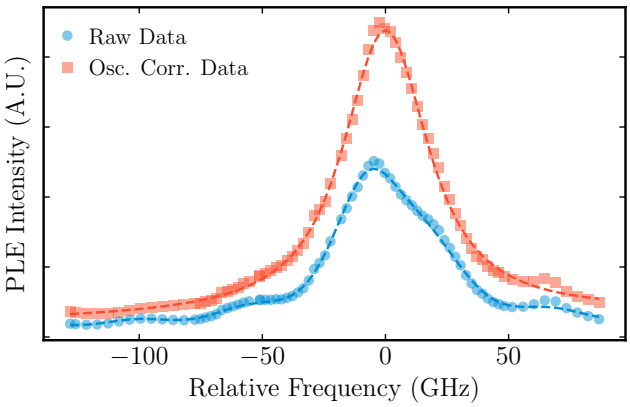

Figure A.4: PLE of Al at 10.25 K, sample A. In the raw PLE counts, an oscillation is observed due to an oscillation in the excitation power. The oscillation-corrected-data is obtained by dividing the raw data with $f(E, \phi)$ given in Eq. A.31.

An energy dependent modulation of the transmittance, reflectance, and PLE signals is observed. This modulation is an artifact caused by a beamsplitter (BS) in the excitation path of our experimental setup. Reflection from this BS, P_R, is incident on the sample. Either transmission through the BS, P_T, or the power before the BS, P_{tot} is measured to monitor the power in each experiment. We find that the ratio f of reflected power divided by the transmitted power fits the following relation,

$$f\,(E, \phi) = P_R/P_T = c + A \sin\left(2\pi v E + \phi\right) \tag{A.31}$$

with $A = 0.07$, $v \simeq (0.18\ \text{meV})^{-1}$, $c = 0.58$ and a phase ϕ which varies between experiments. By normalizing the data by f, we are able to remove the oscillations. Example of PLE data before and after the oscillation correction is shown in Fig. A.4. This method, while effective, may sometimes not completely eliminate the observed oscillations. An example of this correction imperfection is the indium optical depth measurement depicted in Fig. 5.1d.

Appendix B

CONTRIBUTIONS TO THE OPTICAL LINEWIDTH OF SHALLOW DONOR – BOUND EXCITONIC TRANSITION IN ZNO: SUPPLEMENT

Originally published in the Supplemental Material of [97]: V. Niaouris, S. H. D'Ambrosia, C. Zimmermann, X. Wang, E. R. Hansen, M. Titze, E. S. Bielejec, and K.-M. C. Fu, "Contributions to the optical linewidth of shallow donor-bound excitonic transition in ZnO", Optica Quantum **2**, 7–13 (2024).

B.1 PL of Sample A in the transmission setup

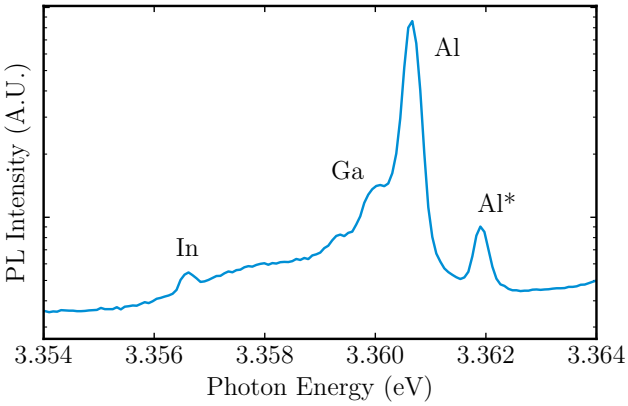

Figure B.1: PL spectrum of sample A. Excitation energy of 3.44 eV, power of 2.6 µW, and spot diameter of 380 µm. $T = 6.9$ K, $B = 0$ T.

The PL spectrum that corresponds to the transmission experiments in Fig. 1d is shown

on Fig. B.1. In addition to being a different sample than that for the spectrum in Fig. 1b, the excitation spot diameter is almost three orders of magnitude larger. In Fig. B.1, the Al emission is $\approx \mathcal{O}(10)$ stronger than Ga emission which is consistent with the measured OD.

B.2 Donor Density Estimation

The area under each optical depth (OD) peak in Fig. 1d is proportional to the number of donors in the probed ensemble, and thus can be used to estimate the average donor density. The donor density of donor N_x (x = Al, Ga, In) can be estimated from [185]

$$N_x = 8\pi \frac{g_{D^0}}{g_{D^0X}} \left(\frac{n}{\lambda_x}\right)^2 \tau_{x,\mathrm{rad}} \int \alpha(\nu) d\nu, \tag{B.1}$$

where g_i is the degeneracy of state i, n is the index of refraction, λ_x is the vacuum transition wavelength, $\tau_{x,\mathrm{rad}}$ is the zero-phonon-line radiative lifetime. We estimate the ZPL radiative lifetime as the total radiative lifetime determined by the slow decay component of the experimental lifetime, divided by the fraction of emission into the ZPL. This fraction is determined by the Huang-Rhys parameter [84] and the ratio of the two-electron satellite transitions to the phonon-assisted transitions. We obtain $\tau_{x,rad} = 0.95\,\mathrm{ns}$, $1.18\,\mathrm{ns}$, and $1.52\,\mathrm{ns}$ for x = Al, Ga, and In, respectively. Using Eq. B.1, we find $N_{\mathrm{Al}} = 7.5 \cdot 10^{15}\,\mathrm{cm}^{-3}$, $N_{\mathrm{Ga}} = 9.9 \cdot 10^{14}\,\mathrm{cm}^{-3}$, and $N_{\mathrm{In}} = 7.4 \cdot 10^{13}\,\mathrm{cm}^{-3}$. These values, measured for Sample A, are within an order of magnitude of the SIMS values measured for sample B. The relative concentrations are consistent with the PL spectra for this sample (App. B.1).

B.3 Temperature dependence of implanted In PLE linewidth

Sample B provided an opportunity to measure the PLE linewidth as a function of temperature for different In implantation fluences (Fig. B.2). At the lowest studied fluences ($< 1.3 \cdot 10^{11}\,\mathrm{cm}^{-2}$) the dependence of linewidth on temperature closely matches the *in-situ*-doped In in sample A. This lowest implantation density is estimated to be ∼50 times higher than the in situ-doped density estimated in Sec. 5.3.1. This similarity supports that the temperature dependence described in Sec. 5.3.2 is intrinsic to the donor, and independent

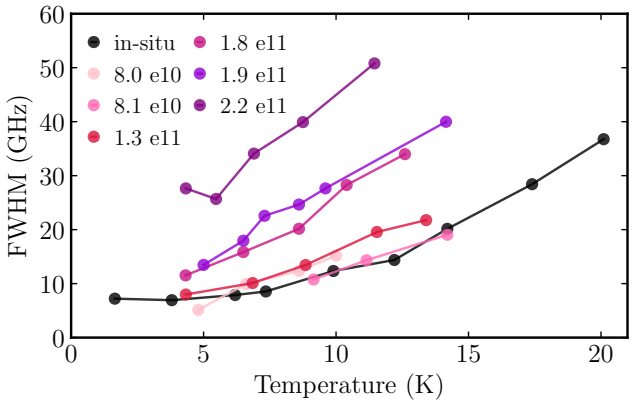

Figure B.2: Temperature-dependent linewidth of the In D^0X transition in Sample B for different implantation fluences. The legend provides the fluences in units of cm^{-2}.

of environmental damage or defect density. As implantation dose increases further, however, both a broader linewidth and a steeper dependence of the linewidth on temperature is observed. The mechanism for the steeper dependence is unknown, but could be due to relaxation from the D^0X state to defect-states created during the implantation process.

B.4 D^0X^* Magneto-PL for Al, Ga, and In

The magneto-PL spectra for all three donors is shown in Fig. B.4. Unlike sample A, sample B has a substantial density of In, which facilitates the study of the weak In D^0X^* line. The Al D^0X^* magnetic field dependence is identical in Sample A and B. The In D^0X^* has a similar magnetic field dependence to Al, splitting into three lines in Voigt and into two lines in Faraday geometry. Unfortunately, the Al D^0X emission obscures the Ga D^0X^* dependence on magnetic field. However, we can observe that the Ga D^0X^* splits in two lines in the Faraday geometry, while the transition that is independent of the magnetic field is clearly visible in the Voigt geometry.

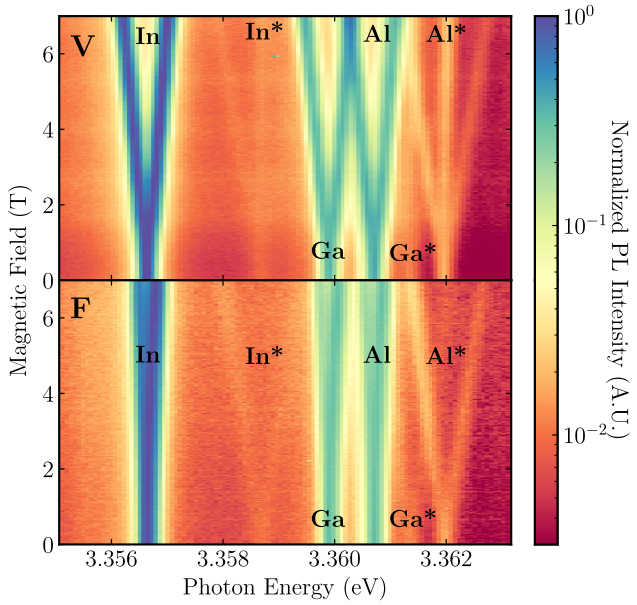

Figure B.3: Magnetic field dependence of D^0X transitions for all donors in sample B, at 7.2 K, with excitation energy 3.44 eV and power 200 nW.

B.5 Discussion of D^0X^* States

A model is proposed by Meyer *et al.* in Ref. [76, 121] to explain the excited states of the bound exciton, including those discussed in Sec. 5.3.2. They introduce two components to this model, one for the lower energy excited states near 2 meV from the ground state, and another for the series of excited states found above 6 meV. Ref. [121] explains the excited states found around and above 6 meV by electronic excited states of the hole, given by increasing n_h and l_h in Eq. A.15 and minimizing with respect to a_e. The values for these excited states obtained from our model in App. A.1 agree well with experimental values presented in Ref. [121, Table III].

Ref. [121] attributes the set of energies found at around 2 meV to rotational-vibrational states of the bound exciton. Ref. [121] evaluates these energies using the Kratzer potential, as given in Eq. A.10, arriving at the following equation for the rotational-vibrational energies

$E(\nu, J)$.

$$E(\nu, J) = -\frac{(2mb^2/\hbar^2)D^2}{\left[\left(\nu+\frac{1}{2}\right)+\sqrt{\left(J+\frac{1}{2}\right)^2+\left(\frac{2mb^2}{\hbar^2}\right)D}\right]^2} \tag{B.2}$$

In analogy to rotational-vibrational states of diatomic molecules (*i.e.* as in Ref. [187]), Ref. [121] interprets D as the bound exciton localization energy, m as the effective mass of the hole, and a as the distance between the hole and impurity. While Meyer *et al.*'s interpretation of a and D yield excited states matching those observed around 2 meV, to determine b, Ref. [121] introduces a *pseudo-acceptor* model approximation for the donor bound exciton, in which the electrons are tightly bound to the impurity and the hole orbits the resulting negatively charged center at a distance equal to the approximate effective Bohr radius of the acceptor in ZnO, 0.8 nm. The bound exciton model in App. A.1 assumes the electrons are nearer to the impurity than the hole similarly to our approach in App. A.1. However, the energy of the system Eq. A.15 is minimized when $b \simeq$ 2.3-2.8 nm, far from 0.8 nm, implying that the *pseudo-acceptor* approximation is inappropriate. Meyer *et al.*'s interpretation also deviates from the original source of this equation [188], where D is the minimum of the Kratzer potential binding the hole and a is the radial position of this minimum. Following the source interpretation of Eq. B.2, Eq. B.2 is equal to the final term of Eq. A.15, and both predict excited states above 6 meV. Eq. B.2 and Eq. A.15 are only distinguished by the accuracy of their prediction of these states, with Eq. A.15's improved accuracy due to its inclusion of changes in a_e between excited states of the hole. The interpretation by Meyer *et al.* in analogy to rotational-vibrational states of diatomic molecules also assumes the g-factor of these excited states is equal to that of the main line, which is contradicted by our results in Sec. 5.3.2 and App. B.4.

B.6 Effect of the Nuclear-Spin Environment

The nuclear-spin environment primarily affects the D^0 levels in the $D^0 \leftrightarrow D^0X$ transition via the electron-nuclear contact hyperfine interaction. The strength of the contact hyperfine interaction for D^0X will be much smaller as the two electrons form a spin-0 singlet state

and the hole is predominantly p-type [189]. The D^0-bound electron interacts with both the lattice nuclear-spins and the donor's nucleus.

The broadening due to the non-zero ^{67}Zn lattice spins is given by a Gaussian distribution of the hyperfine field, $\exp\left(-B^2/\Delta^2_{B,Zn}\right)$, and has a dispersion [54, 102]

$$\Delta_{B,Zn} = \frac{\mu_0 \mu_{\mathrm{Zn}}}{g_e}\sqrt{\frac{32}{27}}\sqrt{\frac{I_{\mathrm{Zn}}+1}{I_{\mathrm{Zn}}}}|u_{\mathrm{Zn}}|^2\sqrt{f\sum_i |\Psi(\vec{R}_i)|^4},$$

in which g_e is the electron g-factor, μ_0 is the vacuum permeability, $I_{\mathrm{Zn}} = 5/2$ is the ^{67}Zn nuclear spin, $\mu_{\mathrm{Zn}} = 0.874\,\mu_N$ is the ^{67}Zn nuclear magnetic moment in terms of the nuclear magneton μ_N, $f = 4.1\%$ is the natural abundance of ^{67}Zn, $\Psi(\vec{R}_i)$ is the effective mass wavefunction at the ith Zn lattice site, and $|u_{\mathrm{Zn}}|^2$ is the ratio of the Bloch function density at the Zn site to the average Bloch function density. Ref. [54] uses a pure hydrogenic effective mass wavefunction for $\Psi(R)$ with Bohr radius of 1.7 Å to estimate a 22 MHz linewidth. Using a slightly modified $\Psi(R)$ which accounts for the central cell correction due to the three different types of donor (App. A.1), we obtain ^{67}Zn nuclear-spin broadened lines of 22, 24 and 29 MHz for Al, Ga and In, respectively. These values are only slightly larger than the reported optically-detected magnetic resonance linewidths for Ga and In of 19 and 22 MHz respectively [91].

The hyperfine splitting due to the donor nuclear spin of spin I depends on the ratio of the Zeeman splitting $g\mu_B B$ to the hyperfine constant A [190]. At 0-field, the $2(2I+1)$ states split into two sublevels separated by $A\sqrt{\frac{1}{4}+I(I+1)}$. At high magnetic field, $g_e\mu_B B \gg A$, each electron Zeeman level splits into (2I + 1) lines with a splitting of $A/2$ between hyperfine levels. $A_{\mathrm{Al}} = 1.45$ MHz [90], $A_{\mathrm{Ga}} = 11.5$ MHz [91], and $A_{\mathrm{In}} = 100$ MHz [91, 92] with $I_{\mathrm{Al}} = 5/2$, $I_{\mathrm{Ga}} = 3/2$ and $I_{\mathrm{In}} = 9/2$.

The nuclear-spin environment contributes to the inhomogeneous broadening of the $D^0 \leftrightarrow D^0X$ transition linewidth. However, any experiment conducted over timescales longer than the relaxation time of the nuclear-spin states will be affected by this broadening. Comparing to the several GHz linewidths observed in Fig. 4d, the nuclear-spin contribution is negligible. However, it is the main source of donor ground-state dephasing [54], and sig-

nificantly affects the two-laser linewidth in coherent population trapping experiments [81, 135]. For In, the hyperfine splitting is comparable to the lifetime-limited linewidth and could theoretically be optically resolved.

B.7 Impurity Isotope Effect

The shift $\Delta E_{S,c}^{don}$ for state S and carrier c due to substitution of the donor atom isotope is given by Heine and Henry in Ref. [180] as

$$\Delta E_{S,c}^{don} = \frac{2\hbar\omega_D}{5}\left(\frac{M_0}{M}\right)^{1/2}\frac{\Delta M}{M}\frac{\gamma_c}{\gamma}\left(-\frac{dE_g}{dkT}\right)_{HT}P_{S,c} \tag{B.3}$$

in which ω_D is the Debye frequency of ZnO, M_0 is the average substituted atom (Zn) mass, M is the mass of the lightest donor isotope, ΔM is the difference between the mass of the heavier and lightest donor isotope, and $\left({}^{dE_g}/_{dkT}\right)_{HT}$ is the temperature dependence of the band gap at high temperature. These values are provided in Table B.1 in App. B.8. γ_c is the fractional oscillator force constant reduction due the presence of a carrier c, $\gamma = \gamma_e + \gamma_h$, is the sum of the force reduction for holes and electrons, with $\gamma_h = 3\gamma_e$ [180], and $P_{S,c}$ is the average volume per atom multiplied by the average amplitude squared within a sphere encompassing the donor and its nearest neighbors (0.2 nm in ZnO).

Constant	Value
$\hbar\omega_d$ (meV)	35.8 (T_D = 416 K) [191]
Ga: M_0, M, ΔM (amu)	69, 71, 2 [192]
In: M_0, M, ΔM (amu)	113, 115, 2 [192]
$\left({}^{dE_g}/_{dkT}\right)_{\mathrm{HT}}$ (meV/K)	3.24 at HT 400 K [191]

Table B.1: ZnO donor atom isotopic substitution constants

The shift from impurity atom isotopic substitution is determined by Eq. B.3 with constants given in Table B.1. Both aluminum and phosphorus have only one commonly occurring isotope and are thus not included in Table B.1. Impurity isotope substitution shifts the

$D^0 \leftrightarrow D^0X$ transition energy by only 16 MHz between Ga^{69} and Ga^{71} and 13 MHz between In^{113} and In^{115}, implying that variation in Zn and O isotopes in the defect environment are the dominant isotopic broadening effect.

B.8 Isotopic Environment Simulation

Energy, $W_{i,c}$	Atom/Isotope	Rel. Abundance
Valence Band, $W_{i,h}$		
0 meV	^{64}Zn	48.6 %
0.66 meV	^{66}Zn	27.9 %
0.98 meV	^{67}Zn	4.1 %
1.31 meV	^{68}Zn	18.8 %
1.97 meV	^{70}Zn	0.6 %
0 meV	^{16}O	99.75 %
2.50 meV	^{17}O	0.05 %
5.00 meV	^{18}O	0.2 %
Conduction Band, $W_{i,e}$		
0 meV	^{64}Zn	48.6 %
0.16 meV	^{66}Zn	27.9 %
0.25 meV	^{67}Zn	4.1 %
0.33 meV	^{68}Zn	18.8 %
0.49 meV	^{70}Zn	0.6 %
0 meV	^{16}O	99.75 %
0.65 meV	^{17}O	0.05 %
1.25 meV	^{18}O	0.2 %

Table B.2: Isotopic perturbation energies in ZnO. Isotopic abundances are obtained from [192].

For Al, Ga, and In defects in ZnO, the isotopic environment is simulated up to 10 nm from the defect, which is sufficient to include the D^0 and D^0X states. The shifts $W_{i,c}$ from environmental zinc and oxygen are calculated using the dependence of the donor lines on isotopic substitution, which is measured in Ref. [125] to be $dE_{D^0X}/dM_{Zn} = 0.41 \pm 0.05\,\text{meV/amu}$ for zinc, and $dE_{D^0X}/dM_O = 3.12 \pm 0.05\,\text{meV/amu}$ for oxygen. Adopting our 80% valence and 20% conduction band shift assumption [129], we obtain

$$W_{i,c} = S_c \Delta M \left(\frac{dE_{D^0X}}{dM} \right). \tag{B.4}$$

Here S_c is the fraction of the total band gap shift due to the valence band or conduction band; if the carrier in question is a hole, the energy shift will be due to the shift in the valence band, if it is an electron, the shift will be due to the shift in the conduction band ($S_h = 0.8$, $S_e = 0.2$). ΔM is the difference between the lightest isotope and a given environmental isotope in amu, and dE_{D^0X}/dM_{elem} is the environmental mass dependence of the D^0X transition energy for element *elem*. The values for environmental isotopic perturbation in ZnO as obtained from Eq. B.4 are given in Table B.2.

Energy, $W_{a,b}$	Atom/Isotope	Rel. Abundance
Valence Band, $W_{i,h}$		
0 meV	^{28}Si	92.2 %
0.76 meV	^{29}Si	4.7 %
1.52 meV	^{30}Si	3.1 %
Conduction Band, $W_{i,e}$		
0 meV	^{28}Si	92.2 %
0.26 meV	^{29}Si	4.7 %
0.52 meV	^{30}Si	3.1 %

Table B.3: Isotopic perturbation energies in Si. Isotopic bundances are obtained from [192].

For the phosphorus defect in Si, the isotopic environment is simulated up to 12 nm (as it is

slightly shallower). The breakdown of the band gap shift between the conduction and valence band shifts is noted in [123] as 75% valence band and 25% conduction band. dE_{D^0X}/dM_{Si} = 1.02 meV, which is obtained from [192]. From Eq. B.4, we find the isotopic perturbation energies shown in Table B.3.

The isotopic environment's contribution to the linewidth of the phosphorus shallow donors in Si's bound exciton transition has been measured in high quality natural silicon [124] as 1.1 GHz. To verify our model we simulated this transition, yielding a broadening of 0.9 GHz (see Fig. B.4), in good agreement with the experimentally observed value. The primary source of discrepancy is likely found in the simplified D^0X state model. Given the difficulty in obtaining an accurate model of the donor bound exciton state, such discrepancies are expected. Despite the uncertainty regarding the D^0X state model, the agreement between the model and the experimental data supports the validity of our approach.

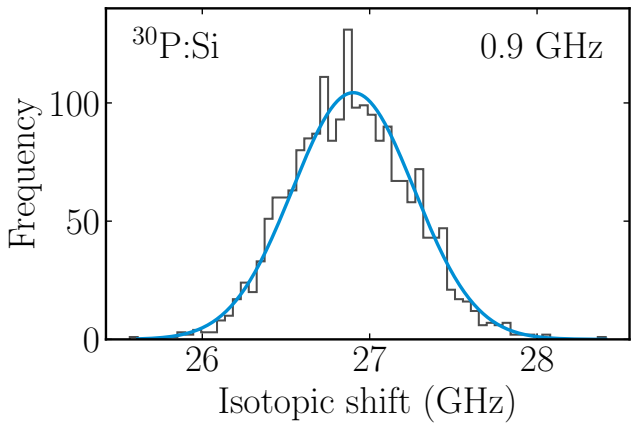

Figure B.4: Inhomogeneous broadening simulation for Silicon at 2000 simulated environments. The resulting inhomogeneous broadening is 0.9 GHz. This compares well to the measured isotopic inhomogeneous broadening of 1.1 GHz [124].

B.9 Investigating power broadening of spectral anti-hole burning

We additionally performed continuous-wave spectral anti-hole burning experiments as a function of pump pulse power. These measurements are performed in the Voigt geometry at 6 T

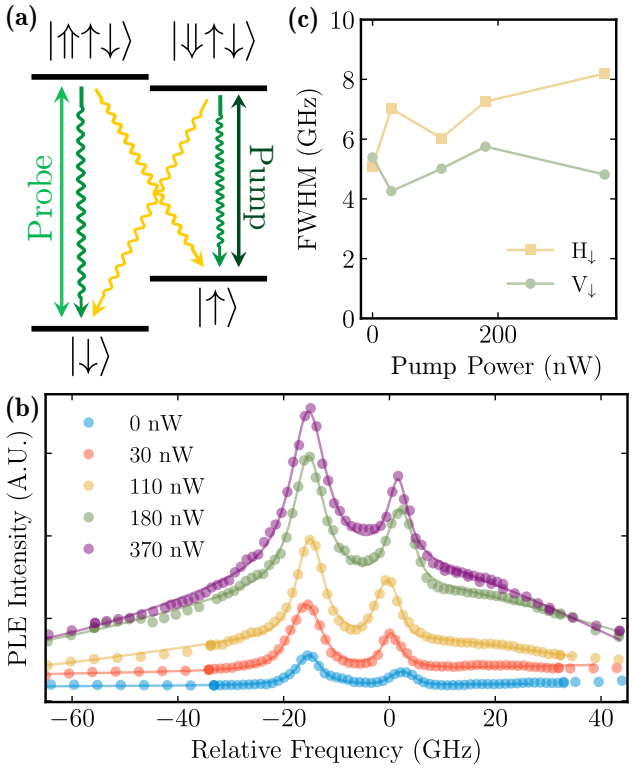

Figure B.5: (a) Energy diagram for a pump-probe experiment in Voigt geometry. (b) PLE spectra of Al D^0X at 1.8 K and 7 T of different pump powers. The probe power is held constant at 290 nW. (c) The anti-hole linewidth for the $V_\downarrow$ and $H_\downarrow$ transitions as a function of pump power.

and 1.8 K. The pump laser is resonant on the $V_\uparrow$ transition, while the probe laser is scanned near the $V_\downarrow$ and $H_\downarrow$ transitions as shown in Fig. B.5a. In this geometry, two anti-holes are observed, split by the hole Zeeman factor (Fig B.5b). As shown in Fig B.5c, the anti-hole linewidth does not depend on pump power. These results indicate the anti-hole linewidth is already maximally broadened by the lowest probe intensities in these steady-state experiments and/or is dominated by the 290 nW probe laser.

B.10 Delay dependence of two-laser transient spectroscopy

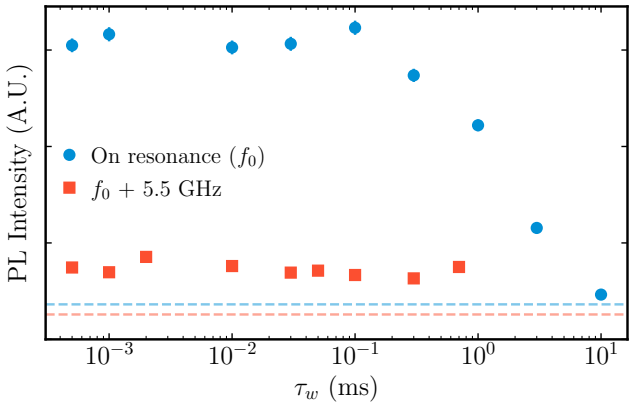

Figure B.6: PL intensity at the start of the probe pulse during pump-probe experiment, as a function of wait time between lasers τ_w at 1.7 K and 7 T. The 170 nW pump laser was on for 100 µs, and the 230 nW probe laser was on for 1 ms. The semi-transparent dashed lines correspond to the optically-pumped intensity at the end of the 1 ms probe pulse. f_0 denotes the center frequency of the Al D^0X emission.

We performed additional transient pump-probe experiments as a function of wait time τ_w between the pump and probe lasers, for two different probe excitation energies, on-resonance with the Al D^0X peak, and +5.5 GHz off-resonance. Fig. B.6 depicts the PL intensity integrated over the first two microseconds of the probe pulse. We observe the same PL intensity for wait times smaller than 0.1 ms, while, After 0.1 ms, the population of the $|\downarrow\rangle$ state starts to deplete due to the longitudinal spin relaxation ($T_1 = 1.5$ ms), as described in [95]. The near-constant PL intensity over wait times shorter than T_1 indicates that the process governing the homogeneous broadening does not occur while the probe laser is off, but occur under optical excitation.

Appendix C

ISOLATION OF SINGLE DONORS: SUPPLEMENT

Originally published in the Supplemental Material of [94]: E. R. Hansen, V. Niaouris, B. E. Matthews, C. Zimmermann, X. Wang, R. Kolodka, L. Vines, S. R. Spurgeon, and K.-M. C. Fu, *Isolation of Single Donors in ZnO*, 2024, arXiv:2310.05806 [cond-mat.mes-hall]

C.1 SIMS measurement of Al and Ga concentration in ZnO substrate

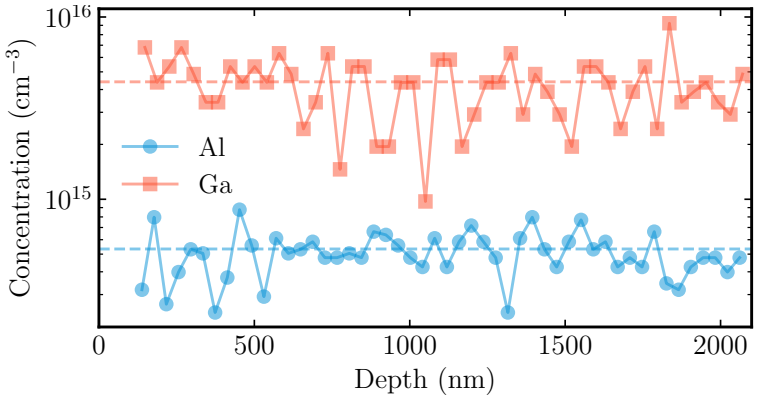

Figure C.1: Donor concentration as a function of depth for the first two micrometers of the back surface of the parent substrate.

The Al and Ga donor concentration in the parent substrate was measured via secondary ion mass spectrometry (SIMS) measurements on the back surface of the substrate. As depicted in Fig. C.1, a relatively uniform donor density is observed through the two-micron measurement depth with an average density of $5.3 \cdot 10^{14}\,\mathrm{cm}^{-3}$ for Al and $4.4 \cdot 10^{15}\,\mathrm{cm}^{-3}$ for Ga.

C.2 Experimental Setup and Equipment

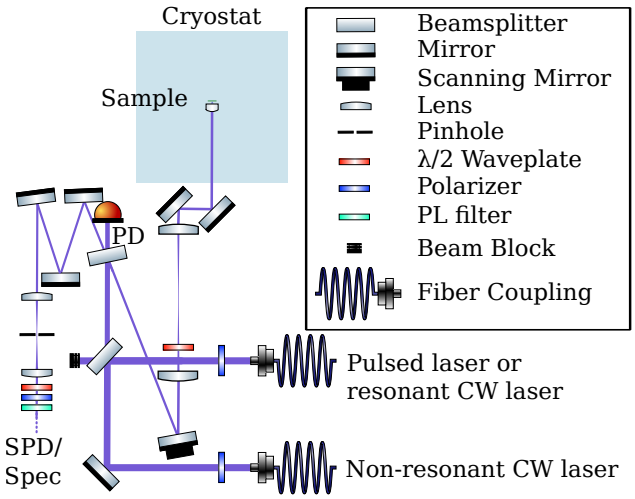

Figure C.2: Optical path for the micro-PL/PLE experiments. A reference to the incident laser power is picked-off by a photodiode (PD). This experiment utilizes an aspheric 3.1 mm-focus 0.62 NA lens inside the sample space for PL collection. The emitted PL is detected with either a single photon detector (SPD) or a spectrometer (Spec).

Fig. C.2 depicts the optical path of the experiments described in the main text.

Due to the high refractive index of ZnO at the In-donor emission wavelength relative to the superfluid He and He gas environment ($n_{ZnO}(\lambda_{In}) = 2.7 > n_{He}(\lambda_{In}) = 1$), only $\sim 1\,\%$ of emitted photons are collected by the first 0.62 NA aspheric lens. The downstream microscope efficiency is $3\,\%$ including the $35\,\%$ detection efficiency, resulting in an overall system efficiency of $\sim 0.03\,\%$. With this $\sim 0.03\,\%$ efficiency, we estimate an overall PL emission rate of $\sim 5 \times 10^7$ photons/second assuming a collection rate of 14,000 photons/second (see 6.4b), which was measured below the saturation limit.

C.3 Spectral kinetic series PL measurements before and after annealing

Fig. C.3a shows kinetic series from the pre-annealed lamella at a location in region B (i) and region C (ii). Similar to Fig. 6.3c in the main text, we observe several weak peaks in the $In^0 \leftrightarrow In^0X$ region which spectrally diffuse over time.

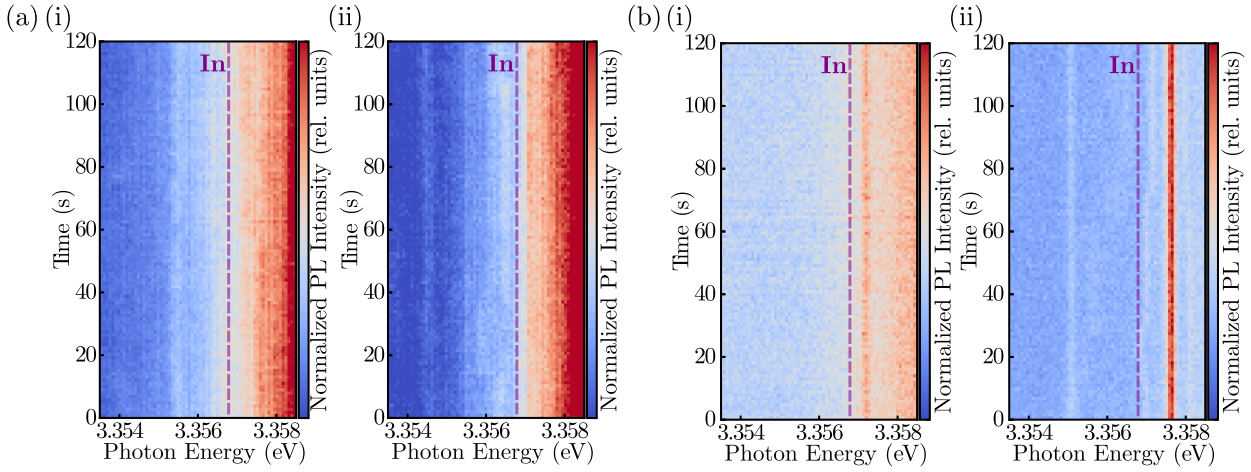

Figure C.3: PL spectra collected with a 1 second exposure time. Excitation is 3.44 eV. (a) Spectra collected from the pre-annealed lamella within region B (i) and region C (ii). (b) Spectra collected from the annealed lamella within region C (i) and region D (ii).

Fig. C.3b shows kinetic series at a location in region C (i) and region D (ii) after annealing. Similar to Fig. 6.3e in the main text, stronger lines near the $In^0 \leftrightarrow In^0X$ energy are observed that are spectrally stable in time. While the luminescence is dramatically improved with annealing, as shown in Fig. C.3b-ii, at some locations weak emission and spectral diffusion can still be observed.

C.4 Single Emitter PL spectrum, uncorrected

In Fig. 6.4b of the main text, each single emitter PL spectra is shifted utilizing the location of the Al^0X and Y_0 lines to adjust for relative energy offsets due to strain. As a result of the correction, the three emitters identified as In donors (emitters $2-4$) lie at the same energy within the spectrometer resolution, however emitter 1 still has exhibits a lower transition energy. For completion, Fig. C.4 shows the uncorrected PL spectra.

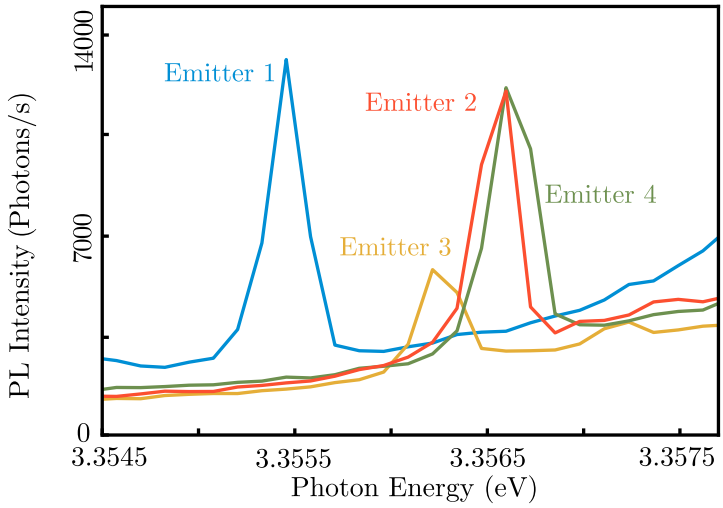

Figure C.4: PL spectra of emitters 1–4 at 5.2 K. Excitation is 3.44 eV.

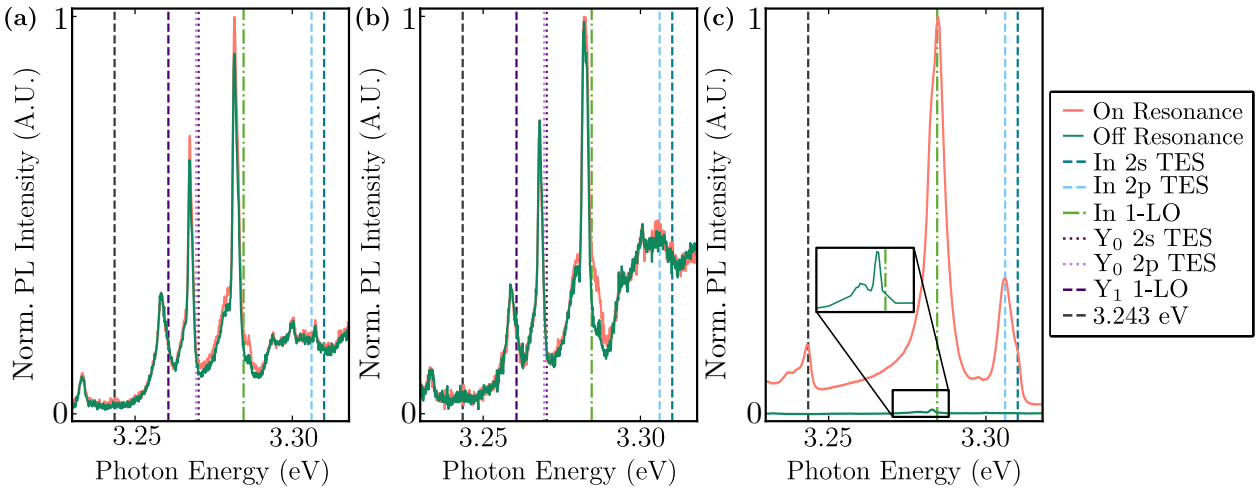

Figure C.5: Sideband PL with resonant and off-resonant excitation, normalized to the on-resonance spectrum. Reported transitions [84] are marked with vertical dashed lines. (a) Emitter 3 sideband PL with 3.356462 eV resonant and 3.56417 eV off-resonant excitation. (b) Emitter 4 sideband PL with 3.356706 eV resonant and 3.356681 eV off-resonant excitation. (c) Sideband PL for implanted In sample with 3.357244 eV resonant and 3.356944 eV off-resonant excitation [81].

C.5 Resonant sideband emission

Fig. 6.4c in the main text depicts the sideband PL of emitter 2 under resonant $In^0 \leftrightarrow In^0X$ excitation. For completeness, Fig. C.5a and Fig. C.5b shows the observed sideband PL for emitters 3 and 4, respectively. Fig. C.5c shows PL sideband from a similar ZnO substrate implanted with In donors [81], correlating the 3.243 eV sideband feature observed in Fig. 6.4c in the main text and Figs. C.5a and C.5b with an In transition. Additionally, under off-resonant excitation, the background near the In 1-LO peak in this In-implanted sample (Fig. C.5c inset) is similar to the background observed on the sideband spectra of emitters 2, 3, and 4.

C.6 Polarization selection rules

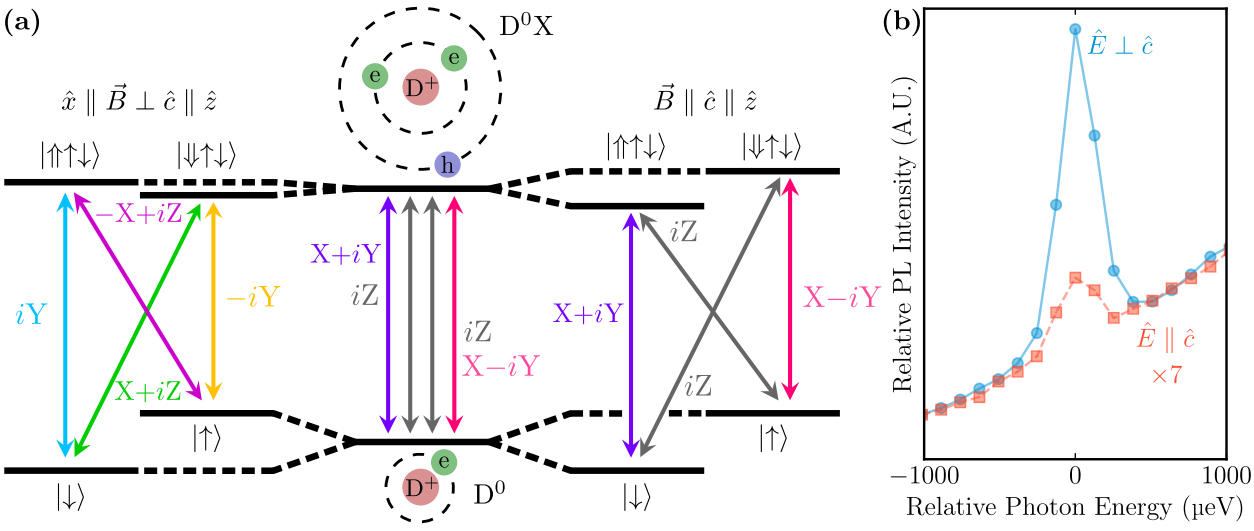

Figure C.6: (a) Polarization selection rules with $\vec{B} \parallel \hat{x}$ (left), $B = 0$ (middle) and $\vec{B} \parallel \hat{z}$ (right) in the sample reference frame ($\hat{c} \parallel \hat{z}$). Here, $|\uparrow\rangle$ and $|\downarrow\rangle$ ($|\Uparrow\rangle$ and $|\Downarrow\rangle$) denote the electron (hole) spin up and down states. $X = \frac{a}{\sqrt{2}}\hat{x}$, $Y = \frac{a}{\sqrt{2}}\hat{y}$, and $Z = b\hat{z}$ [93], where $a = 0.995$ and $b = 0.0999$ [74]. (b) O-field PL of emitter 2, collecting polarization parallel and perpendicular to the $\hat{c}$ axis.

PL emission polarization depends on the applied magnetic field orientation in relation

to the crystal axis $\hat{c}$. Following Ref. [53, 74, 93], Fig. C.6a shows the expected photon polarization selection rules for the different transitions and magnetic field geometries, when $\hat{c} \parallel \hat{z}$.

In our experimental setup, the optical axis is always parallel to the $\hat{y}$ axis. Hence, we cannot detect transitions with polarization components parallel to $\hat{y}$ (where $\hat{y} \perp \hat{c}$). Therefore, we expect the PL emission polarized perpendicular to the crystal axis ($\hat{E} \parallel \hat{x} \perp \hat{c}$) to be $\sim 50\times$ brighter than emission polarized parallel to the crystal axis ($\hat{E} \parallel \hat{z} \parallel \hat{c}$). Fig. C.6b shows the emission at the two different polarizations at 0 T for emitter 2. We are able to observe the weak $\hat{E} \parallel \hat{c}$ emission, and find that $\mathrm{In}^0 \leftrightarrow \mathrm{In}^0\mathrm{X}$ $\hat{E} \perp \hat{c}$ emission is $\sim 28\times$ brighter than $\hat{E} \parallel \hat{c}$, which is close to the theoretical 50. Fig. C.6a also depicts the polarization selection rules for $\vec{B} \parallel \hat{c}$. In this geometry, we were unable to detect the weak $\hat{E} \parallel \hat{c}$ peaks.

C.7 Lifetime measurement background

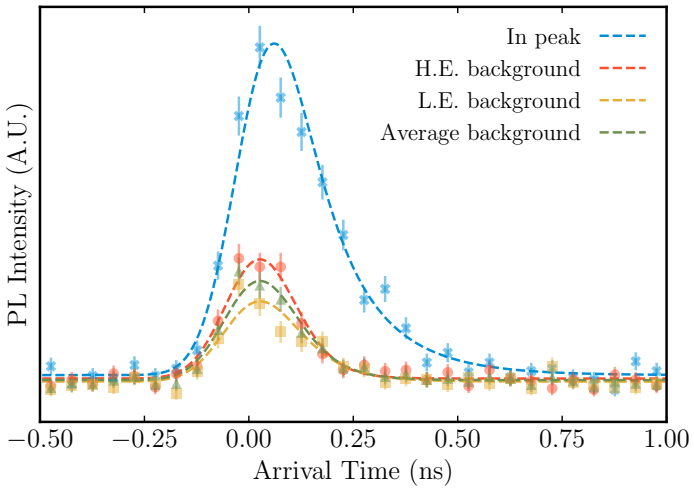

Figure C.7: Example lifetime measurement on emitter 3, depicting the measured lifetime on the emitter peak, the Al background on the higher (H.E.) and lower (L.E.) energy tails ($\sim \pm 60$ GHz), and the averaged of the two background contributions.

When performing time-resolved measurements on the In emitter, part of the collected

photoluminescence to corresponds to background emission; the single In emitters lie on the tail of the Al/Ga emission. To estimate the background contribution, we perform lifetime measurements collecting PL from the high and low energy edges ($\sim \pm 60\,\mathrm{GHz}$) of the In emission. Assuming the background contribution is nearly linear, we average the two lifetime background data and fit to an exponential-Gaussian convolution profile. We use the fitted background parameters as fixed parameters to the double exponential-Gaussian profile fitted to the In emitter lifetime data (Fig. C.7). For the data presented in Fig. C.7, the background lifetime is $110 \pm 20\,\mathrm{ps}$.

BIBLIOGRAPHY

[1]D. E. Deutsch and R. Penrose, "Quantum computational networks", Proceedings of the Royal Society of London. A. Mathematical and Physical Sciences **425**, 73–90 (1989).

[2]A. Steane, "Quantum computing", Reports on Progress in Physics **61**, 117 (1998).

[3]T. D. Ladd, F. Jelezko, R. Laflamme, Y. Nakamura, C. Monroe, and J. L. O'Brien, "Quantum computers", Nature **464**, 45–53 (2010).

[4]S. S. Gill, O. Cetinkaya, S. Marrone, D. Claudino, D. Haunschild, L. Schlote, H. Wu, C. Ottaviani, X. Liu, S. P. Machupalli, K. Kaur, P. Arora, J. Liu, A. Farouk, H. H. Song, S. Uhlig, and K. Ramamohanarao, *Quantum computing: vision and challenges*, 2024, arXiv:2403.02240 [cs.DC].

[5]C. Helstrom, J. Liu, and J. Gordon, "Quantum-mechanical communication theory", Proceedings of the IEEE **58**, 1578–1598 (1970).

[6]S. Pirandola, U. L. Andersen, L. Banchi, M. Berta, D. Bunandar, R. Colbeck, D. Englund, T. Gehring, C. Lupo, C. Ottaviani, J. L. Pereira, M. Razavi, J. S. Shaari, M. Tomamichel, V. C. Usenko, G. Vallone, P. Villoresi, and P. Wallden, "Advances in quantum cryptography", Adv. Opt. Photon. **12**, 1012–1236 (2020).

[7]J. S. Sidhu, S. K. Joshi, M. Gündoğan, T. Brougham, D. Lowndes, L. Mazzarella, M. Krutzik, S. Mohapatra, D. Dequal, G. Vallone, P. Villoresi, A. Ling, T. Jennewein, M. Mohageg, J. G. Rarity, I. Fuentes, S. Pirandola, and D. K. L. Oi, "Advances in space quantum communications", IET Quantum Communication **2**, 182–217 (2021).

[8]S. Pirandola, "Satellite quantum communications: fundamental bounds and practical security", Phys. Rev. Res. **3**, 023130 (2021).

[9]S.-H. Wei, B. Jing, X.-Y. Zhang, J.-Y. Liao, C.-Z. Yuan, B.-Y. Fan, C. Lyu, D.-L. Zhou, Y. Wang, G.-W. Deng, H.-Z. Song, D. Oblak, G.-C. Guo, and Q. Zhou, "Towards real-world quantum networks: a review", Laser & Photonics Reviews **16**, 2100219 (2022).

[10]D. Budker and M. Romalis, "Optical magnetometry", Nature Physics **3**, 227–234 (2007).

[11]C. L. Degen, F. Reinhard, and P. Cappellaro, "Quantum sensing", Rev. Mod. Phys. **89**, 035002 (2017).

[12]V. Giovannetti, S. Lloyd, and L. Maccone, "Quantum-enhanced measurements: beating the standard quantum limit", Science **306**, 1330–1336 (2004).

[13]V. Giovannetti, S. Lloyd, and L. Maccone, "Advances in quantum metrology", Nature Photonics **5**, 222–229 (2011).

[14]E. Polino, M. Valeri, N. Spagnolo, and F. Sciarrino, "Photonic quantum metrology", AVS Quantum Science **2**, 024703 (2020).

[15]R. P. Feynman, "Simulating physics with computers", International Journal of Theoretical Physics **21**, 467–488 (1982).

[16]P. Shor, "Algorithms for quantum computation: discrete logarithms and factoring", in Proceedings 35th annual symposium on foundations of computer science (1994), pp. 124–134.

[17]L. K. Grover, "A fast quantum mechanical algorithm for database search", in Proceedings of the twenty-eighth annual acm symposium on theory of computing, STOC '96 (1996), pp. 212–219.

[18]A. J. Daley, I. Bloch, C. Kokail, S. Flannigan, N. Pearson, M. Troyer, and P. Zoller, "Practical quantum advantage in quantum simulation", Nature **607**, 667–676 (2022).

[19]F. Arute, K. Arya, R. Babbush, D. Bacon, J. C. Bardin, R. Barends, R. Biswas, S. Boixo, F. G. S. L. Brandao, D. A. Buell, B. Burkett, Y. Chen, Z. Chen, B. Chiaro, R. Collins, W. Courtney, A. Dunsworth, E. Farhi, B. Foxen, A. Fowler, C. Gidney, M. Giustina, R. Graff, K. Guerin, S. Habegger, M. P. Harrigan, M. J. Hartmann, A. Ho, M. Hoffmann, T. Huang, T. S. Humble, S. V. Isakov, E. Jeffrey, Z. Jiang, D. Kafri, K. Kechedzhi, J. Kelly, P. V. Klimov, S. Knysh, A. Korotkov, F. Kostritsa, D. Landhuis, M. Lindmark, E. Lucero, D. Lyakh, S. Mandrà, J. R. McClean, M. McEwen, A. Megrant, X. Mi, K. Michielsen, M. Mohseni, J. Mutus, O. Naaman, M. Neeley, C. Neill, M. Y. Niu, E. Ostby, A. Petukhov, J. C. Platt, C. Quintana, E. G. Rieffel, P. Roushan, N. C. Rubin, D. Sank, K. J. Satzinger, V. Smelyanskiy, K. J. Sung, M. D. Trevithick, A. Vainsencher, B. Villalonga, T. White, Z. J. Yao, P. Yeh, A. Zalcman, H. Neven, and J. M. Martinis, "Quantum supremacy using a programmable superconducting processor", Nature **574**, 505–510 (2019).

[20]F. Pan, K. Chen, and P. Zhang, "Solving the sampling problem of the sycamore quantum circuits", Phys. Rev. Lett. **129**, 090502 (2022).

[21]H. J. Kimble, "The quantum internet", Nature **453**, 1023–1030 (2008).

[22]K. Azuma, S. E. Economou, D. Elkouss, P. Hilaire, L. Jiang, H.-K. Lo, and I. Tzitrin, "Quantum repeaters: from quantum networks to the quantum internet", Rev. Mod. Phys. **95**, 045006 (2023).

[23]C. H. Bennett and G. Brassard, "Quantum cryptography: public key distribution and coin tossing", Theoretical Computer Science **560**, Theoretical Aspects of Quantum Cryptography – celebrating 30 years of BB84, 7–11 (2014).

[24]N. H. Nickerson, J. F. Fitzsimons, and S. C. Benjamin, "Freely scalable quantum technologies using cells of 5-to-50 qubits with very lossy and noisy photonic links", Phys. Rev. X **4**, 041041 (2014).

[25]Z. Zhang and Q. Zhuang, "Distributed quantum sensing", Quantum Science and Technology **6**, 043001 (2021).

[26]P. Kómár, E. M. Kessler, M. Bishof, L. Jiang, A. S. Sørensen, J. Ye, and M. D. Lukin, "A quantum network of clocks", Nature Physics **10**, 582–587 (2014).

[27]B. Schumacher, "Quantum coding", Phys. Rev. A **51**, 2738–2747 (1995).

[28]D. P. DiVincenzo, "The physical implementation of quantum computation", Fortschritte der Physik **48**, 771–783 (2000).

[29]N. P. de Leon, K. M. Itoh, D. Kim, K. K. Mehta, T. E. Northup, H. Paik, B. S. Palmer, N. Samarth, S. Sangtawesin, and D. W. Steuerman, "Materials challenges and opportunities for quantum computing hardware", Science **372**, eabb2823 (2021).

[30]A. Reiserer, "Colloquium: Cavity-enhanced quantum network nodes", Rev. Mod. Phys. **94**, 041003 (2022).

[31]D. Loss and D. P. DiVincenzo, "Quantum computation with quantum dots", Phys. Rev. A **57**, 120–126 (1998).

[32]M. Veldhorst, C. H. Yang, J. C. C. Hwang, W. Huang, J. P. Dehollain, J. T. Muhonen, S. Simmons, A. Laucht, F. E. Hudson, K. M. Itoh, A. Morello, and A. S. Dzurak, "A two-qubit logic gate in silicon", Nature **526**, 410–414 (2015).

[33]Y. Xu, J. Chu, J. Yuan, J. Qiu, Y. Zhou, L. Zhang, X. Tan, Y. Yu, S. Liu, J. Li, F. Yan, and D. Yu, "High-fidelity, high-scalability two-qubit gate scheme for superconducting qubits", Phys. Rev. Lett. **125**, 240503 (2020).

[34]C. Zhang, F. Pokorny, W. Li, G. Higgins, A. Pöschl, I. Lesanovsky, and M. Hennrich, "Submicrosecond entangling gate between trapped ions via rydberg interaction", Nature **580**, 345–349 (2020).

[35]S. Takeda and A. Furusawa, "Toward large-scale fault-tolerant universal photonic quantum computing", APL Photonics **4**, 060902 (2019).

[36]C. S. Adams, J. D. Pritchard, and J. P. Shaffer, "Rydberg atom quantum technologies", Journal of Physics B: Atomic, Molecular and Optical Physics **53**, 012002 (2019).

[37]C. D. Bruzewicz, J. Chiaverini, R. McConnell, and J. M. Sage, "Trapped-ion quantum computing: Progress and challenges", Applied Physics Reviews **6**, 021314 (2019).

[38]K. K. Mehta, C. Zhang, M. Malinowski, T.-L. Nguyen, M. Stadler, and J. P. Home, "Integrated optical multi-ion quantum logic", Nature **586**, 533–537 (2020).

[39]M. Kjaergaard, M. E. Schwartz, J. Braumüller, P. Krantz, J. I.-J. Wang, S. Gustavsson, and W. D. Oliver, "Superconducting qubits: current state of play", Annual Review of Condensed Matter Physics **11**, 369–395 (2020).

[40]K. Saeedi, S. Simmons, J. Z. Salvail, P. Dluhy, H. Riemann, N. V. Abrosimov, P. Becker, H.-J. Pohl, J. J. L. Morton, and M. L. W. Thewalt, "Room-temperature quantum bit storage exceeding 39 minutes using ionized donors in silicon-28", Science **342**, 830–833 (2013).

[41]T. F. Watson, B. Weber, Y.-L. Hsueh, L. C. L. Hollenberg, R. Rahman, and M. Y. Simmons, "Atomically engineered electron spin lifetimes of 30 s in silicon", Science Advances **3**, e1602811 (2017).

[42]J. T. Muhonen, A. Laucht, S. Simmons, J. P. Dehollain, R. Kalra, F. E. Hudson, S. Freer, K. M. Itoh, D. N. Jamieson, J. C. McCallum, A. S. Dzurak, and A. Morello, "Quantifying the quantum gate fidelity of single-atom spin qubits in silicon by randomized benchmarking", Journal of Physics: Condensed Matter **27**, 154205 (2015).

[43]A. M. Tyryshkin, S. Tojo, J. J. L. Morton, H. Riemann, N. V. Abrosimov, P. Becker, H.-J. Pohl, T. Schenkel, M. L. W. Thewalt, K. M. Itoh, and S. A. Lyon, "Electron spin coherence exceeding seconds in high-purity silicon", Nature Materials **11**, 143–147 (2012).

[44]S. Benjamin, B. Lovett, and J. Smith, "Prospects for measurement-based quantum computing with solid state spins", Laser & Photonics Reviews **3**, 556–574 (2009).

[45]G. Tosi, F. A. Mohiyaddin, V. Schmitt, S. Tenberg, R. Rahman, G. Klimeck, and A. Morello, "Silicon quantum processor with robust long-distance qubit couplings", Nature Communications **8**, 450 (2017).

[46]K.-M. C. Fu, W. Yeo, S. Clark, C. Santori, C. Stanley, M. C. Holland, and Y. Yamamoto, "Millisecond spin-flip times of donor-bound electrons in GaAs", Phys. Rev. B **74**, 121304 (2006).

[47]S. M. Clark, K.-M. C. Fu, Q. Zhang, T. D. Ladd, C. Stanley, and Y. Yamamoto, "Ultrafast optical spin echo for electron spins in semiconductors", Phys. Rev. Lett. **102**, 247601 (2009).

[48]A. Delteil, Z. Sun, W.-b. Gao, E. Togan, S. Faelt, and A. Imamoğlu, "Generation of heralded entanglement between distant hole spins", Nature Physics **12**, 218–223 (2016).

[49]Y. He, Y.-M. He, Y.-J. Wei, X. Jiang, M.-C. Chen, F.-L. Xiong, Y. Zhao, C. Schneider, M. Kamp, S. Höfling, C.-Y. Lu, and J.-W. Pan, "Indistinguishable tunable single photons emitted by spin-flip raman transitions in ingaas quantum dots", Phys. Rev. Lett. **111**, 237403 (2013).

[50]K. De Greve, L. Yu, P. L. McMahon, J. S. Pelc, C. M. Natarajan, N. Y. Kim, E. Abe, S. Maier, C. Schneider, M. Kamp, S. Höfling, R. H. Hadfield, A. Forchel, M. M. Fejer, and Y. Yamamoto, "Quantum-dot spin–photon entanglement via frequency downconversion to telecom wavelength", Nature **491**, 421–425 (2012).

[51]S. O. Kucheyev, P. N. K. Deenapanray, C. Jagadish, J. S. Williams, M. Yano, K. Koike, S. Sasa, M. Inoue, and K.-i. Ogata, "Electrical isolation of ZnO by ion bombardment", Applied Physics Letters **81**, 3350–3352 (2002).

[52]H. Morkoç and Ü. Özgür, "Processing, Devices, and Heterostructures", in *Zinc oxide* (John Wiley & Sons, Ltd, 2009) Chap. 8, pp. 387–467.

[53]M. R. Wagner, J.-H. Schulze, R. Kirste, M. Cobet, A. Hoffmann, C. Rauch, A. V. Rodina, B. K. Meyer, U. Röder, and K. Thonke, "Γ_7 Valence band symmetry related hole fine splitting of bound excitons in zno observed in magneto-optical studies", Phys. Rev. B **80**, 205203 (2009).

[54]X. Linpeng, M. L. Viitaniemi, A. Vishnuradhan, Y. Kozuka, C. Johnson, M. Kawasaki, and K.-M. C. Fu, "Coherence properties of shallow donor qubits in ZnO", Phys. Rev. Applied **10**, 064061 (2018).

[55]J. M. Taylor, C. M. Marcus, and M. D. Lukin, "Long-Lived Memory for Mesoscopic Quantum Bits", Phys. Rev. Lett. **90**, 206803 (2003).

[56]J. J. L. Morton, A. M. Tyryshkin, R. M. Brown, S. Shankar, B. W. Lovett, A. Ardavan, T. Schenkel, E. E. Haller, J. W. Ager, and S. A. Lyon, "Solid-state quantum memory using the 31p nuclear spin", Nature **455**, 1085–1088 (2008).

[57]J. Rochman, T. Xie, J. G. Bartholomew, K. C. Schwab, and A. Faraon, "Microwave-to-optical transduction with erbium ions coupled to planar photonic and superconducting resonators", Nature Communications **14**, 1153 (2023).

[58]A. I. Lvovsky, B. C. Sanders, and W. Tittel, "Optical quantum memory", Nature Photonics **3**, 706–714 (2009).

[59]N. Sangouard, C. Simon, H. de Riedmatten, and N. Gisin, "Quantum repeaters based on atomic ensembles and linear optics", Rev. Mod. Phys. **83**, 33–80 (2011).

[60]L. V. Hau, S. E. Harris, Z. Dutton, and C. H. Behroozi, "Light speed reduction to 17 metres per second in an ultracold atomic gas", Nature **397**, 594–598 (1999).

[61]A. V. Gorshkov, A. André, M. Fleischhauer, A. S. Sørensen, and M. D. Lukin, "Universal approach to optimal photon storage in atomic media", Phys. Rev. Lett. **98**, 123601 (2007).

[62]Z.-Q. Zhou, C. Liu, C.-F. Li, G.-C. Guo, D. Oblak, M. Lei, A. Faraon, M. Mazzera, and H. de Riedmatten, "Photonic integrated quantum memory in rare-earth doped solids", Laser & Photonics Reviews **17**, 2300257 (2023).

[63]H. Morkoç and Ü. Özgür, "General Properties of ZnO", in *Zinc Oxide: Fundamentals, Materials and Device Technology* (John Wiley & Sons, Ltd, 2009) Chap. 1, pp. 1–76.

[64]D. Ehrentraut, H. Sato, Y. Kagamitani, H. Sato, A. Yoshikawa, and T. Fukuda, "Solvothermal growth of ZnO", Progress in Crystal Growth and Characterization of Materials **52**, 280–335 (2006).

[65]R. Triboulet, "Growth of ZnO bulk crystals: A review", Progress in Crystal Growth and Characterization of Materials **60**, 1–14 (2014).

[66]V. Avrutin, G. Cantwell, J. Zhang, J. J. Song, D. J. Silversmith, and H. Morkoç, "Bulk ZnO: Current Status, Challenges, and Prospects", Proceedings of the IEEE **98**, 1339–1350 (2010).

[67]Y. Kozuka, A. Tsukazaki, and M. Kawasaki, "Challenges and opportunities of ZnO-related single crystalline heterostructures", Applied Physics Reviews **1**, 011303 (2014).

[68]K. Maeda, M. Sato, I. Niikura, and T. Fukuda, "Growth of 2 inch ZnO bulk single crystal by the hydrothermal method", Semiconductor Science and Technology **20**, S49 (2005).

[69]T. Fukuda, Y. Mikawa, and D. Ehrentraut, "State-of-the-art ZnO bulk crystal growth", in Zinc oxide materials and devices ii, Vol. 6474, edited by F. H. Teherani and C. W. Litton (International Society for Optics and Photonics, 2007), p. 647412.

[70]S. Graubner, C. Neumann, N. Volbers, B. K. Meyer, J. Bläsing, and A. Krost, "Preparation of ZnO substrates for epitaxy: Structural, surface, and electrical properties", Applied Physics Letters **90**, 042103 (2007).

[71]S. Akasaka, K. Nakahara, A. Tsukazaki, A. Ohtomo, and M. Kawasaki, "$Mg_xZn_{1-x}O$ Films with a Low Residual Donor Concentration ($<10^{15}$ cm^{-3}) Grown by Molecular Beam Epitaxy", Applied Physics Express **3**, 071101 (2010).

[72]F. Kondev, M. Wang, W. Huang, S. Naimi, and G. Audi, "The NUBASE2020 evaluation of nuclear physics properties", Chinese Physics C **45**, 030001 (2021).

[73]K. J. Button, D. R. Cohn, M. von Ortenbert, B. Lax, E. Mollwo, and R. Helbig, "Zeeman Splitting of Anomalous Shallow Bound States in ZnO", Phys. Rev. Lett. **28**, 1637–1639 (1972).

[74]W. R. L. Lambrecht, A. V. Rodina, S. Limpijumnong, B. Segall, and B. K. Meyer, "Valence-band ordering and magneto-optic exciton fine structure in ZnO", Phys. Rev. B **65**, 075207 (2002).

[75]K. Hümmer, "Interband Magnetoreflection of ZnO", physica status solidi (b) **56**, 249–260 (1973).

[76]B. K. Meyer, H. Alves, D. M. Hofmann, W. Kriegseis, D. Forster, F. Bertram, J. Christen, A. Hoffmann, M. Straßburg, M. Dworzak, U. Haboeck, and A. V. Rodina, "Bound exciton and donor–acceptor pair recombinations in ZnO", physica status solidi (b) **241**, 231–260 (2004).

[77]D. C. Reynolds, D. C. Look, B. Jogai, C. W. Litton, G. Cantwell, and W. C. Harsch, "Valence-band ordering in zno", Phys. Rev. B **60**, 2340–2344 (1999).

[78]Y. Varshni, "Temperature dependence of the energy gap in semiconductors", Physica **34**, 149–154 (1967).

[79]H. Landolt (1831-1910), R. Börnstein (1852-1913), O. Madelung (1922-2017), M. Schulz, and H. Weiss, *Numerical data and functional relationships in science and technology. Group 3, Crystal and solid state physics. Vol. 17, Semiconductors*, English, New series (Springer-Verlag, Berlin, 1982).

[80]R. Börnstein (1852-1913), H. Landolt (1831-1910), O. Madelung (1922-2017), W. Martienssen, U. Rössler, and D. Strauch, *Numerical data and functional relationships in science and technology. Group 3 Crystal and solid state physics Vol. 41 Semiconductors: supplement to Vols. III/17, 22*, English (Springer-Verlag, Berlin, 2001).

[81]X. Wang, C. Zimmermann, M. Titze, V. Niaouris, E. R. Hansen, S. H. D'Ambrosia, L. Vines, E. S. Bielejec, and K.-M. C. Fu, "Properties of Donor Qubits in ZnO Formed by Indium-Ion Implantation", Phys. Rev. Appl. **19**, 054090 (2023).

[82]Planck Collaboration, Ade, P. A. R., Aghanim, N., Arnaud, M., Ashdown, M., Aumont, J., Baccigalupi, C., Banday, A. J., Barreiro, R. B., Bartlett, J. G., Bartolo, N., Battaner, E., Battye, R., Benabed, K., Benoît, A., Benoit-Lévy, A., Bernard, J.-P., Bersanelli, M., Bielewicz, P., Bock, J. J., Bonaldi, A., Bonavera, L., Bond, J. R., Borrill, J., Bouchet, F. R., Boulanger, F., Bucher, M., Burigana, C., Butler, R. C., Calabrese, E., Cardoso, J.-F., Catalano, A., Challinor, A., Chamballu, A., Chary, R.-R., Chiang, H. C., Chluba, J., Christensen, P. R., Church, S., Clements, D. L., Colombi, S., Colombo, L. P. L., Combet, C., Coulais, A., Crill, B. P., Curto, A., Cuttaia, F., Danese, L., Davies, R. D., Davis, R. J., de Bernardis, P., de Rosa, A., de Zotti, G., Delabrouille, J., Désert, F.-X., Di Valentino, E., Dickinson, C., Diego, J. M., Dolag, K., Dole, H., Donzelli, S., Doré, O., Douspis, M., Ducout, A., Dunkley, J., Dupac, X., Efstathiou, G., Elsner, F., Enßlin, T. A., Eriksen, H. K., Farhang, M., Fergusson, J., Finelli, F., Forni, O., Frailis, M., Fraisse, A. A., Franceschi, E., Frejsel, A., Galeotta, S., Galli, S., Ganga, K., Gauthier, C., Gerbino, M., Ghosh, T., Giard, M., Giraud-Héraud, Y., Giusarma, E., Gjerløw, E., González-Nuevo, J., Górski, K. M., Gratton, S., Gregorio, A., Gruppuso, A., Gudmundsson, J. E., Hamann, J., Hansen, F. K., Hanson, D., Harrison, D. L., Helou, G., Henrot-Versillé, S., Hernández-Monteagudo, C., Herranz, D., Hildebrandt, S. R., Hivon, E., Hobson, M., Holmes, W. A., Hornstrup, A., Hovest, W., Huang, Z., Huffenberger, K. M., Hurier, G., Jaffe, A. H., Jaffe, T. R., Jones, W. C., Juvela, M., Keihänen, E., Keskitalo, R., Kisner, T. S., Kneissl, R., Knoche, J., Knox, L., Kunz, M., Kurki-Suonio, H., Lagache, G., Lähteenmäki, A., Lamarre, J.-M., Lasenby, A., Lattanzi, M., Lawrence, C. R., Leahy, J. P., Leonardi, R., Lesgourgues, J., Levrier, F., Lewis, A., Liguori, M., Lilje, P. B., Linden-Vørnle, M., López-Caniego, M., Lubin, P. M., Macías-Pérez, J. F., Maggio, G., Maino, D., Mandolesi, N., Mangilli, A., Marchini, A., Maris, M., Martin, P. G., Martinelli, M., Martínez-González, E., Masi, S., Matarrese, S., McGehee, P., Meinhold, P. R., Melchiorri, A., Melin, J.-B., Mendes, L., Mennella, A., Migliaccio, M., Millea, M., Mitra, S., Miville-Deschênes, M.-A., Moneti, A., Montier, L., Morgante, G., Mortlock, D., Moss, A., Munshi, D., Murphy, J. A., Naselsky, P., Nati, F., Natoli, P., Netterfield, C. B., Nørgaard-Nielsen, H. U., Noviello, F., Novikov, D., Novikov, I., Oxborrow, C. A., Paci, F., Pagano, L., Pajot, F., Paladini, R., Paoletti, D., Partridge, B., Pasian, F., Patanchon, G., Pearson, T. J., Perdereau, O., Perotto, L., Perrotta, F., Pettorino, V., Piacentini, F., Piat, M., Pierpaoli, E., Pietrobon, D., Plaszczynski, S., Pointecouteau, E., Polenta, G., Popa, L., Pratt, G. W., Prézeau, G., Prunet, S., Puget, J.-L., Rachen, J. P., Reach, W. T., Rebolo, R., Reinecke, M., Remazeilles, M., Renault, C., Renzi, A., Ristorcelli, I., Rocha, G., Rosset, C., Rossetti, M.,

Roudier, G., Rouillé d'Orfeuil, B., Rowan-Robinson, M., Rubiño-Martín, J. A., Rusholme, B., Said, N., Salvatelli, V., Salvati, L., Sandri, M., Santos, D., Savelainen, M., Savini, G., Scott, D., Seiffert, M. D., Serra, P., Shellard, E. P. S., Spencer, L. D., Spinelli, M., Stolyarov, V., Stompor, R., Sudiwala, R., Sunyaev, R., Sutton, D., Suur-Uski, A.-S., Sygnet, J.-F., Tauber, J. A., Terenzi, L., Toffolatti, L., Tomasi, M., Tristram, M., Trombetti, T., Tucci, M., Tuovinen, J., Türler, M., Umana, G., Valenziano, L., Valiviita, J., Van Tent, F., Vielva, P., Villa, F., Wade, L. A., Wandelt, B. D., Wehus, I. K., White, M., White, S. D. M., Wilkinson, A., Yvon, D., Zacchei, A., and Zonca, A., "Planck 2015 results - XIII. Cosmological parameters", A&A **594**, A13 (2016).

[83]D. W. Hamby, D. A. Lucca, M. J. Klopfstein, and G. Cantwell, "Temperature dependent exciton photoluminescence of bulk ZnO", Journal of Applied Physics **93**, 3214–3217 (2003).

[84]M. R. Wagner, G. Callsen, J. S. Reparaz, J.-H. Schulze, R. Kirste, M. Cobet, I. A. Ostapenko, S. Rodt, C. Nenstiel, M. Kaiser, A. Hoffmann, A. V. Rodina, M. R. Phillips, S. Lautenschläger, S. Eisermann, and B. K. Meyer, "Bound excitons in ZnO: structural defect complexes versus shallow impurity centers", Phys. Rev. B **84**, 035313 (2011).

[85]S. L. Chen, W. M. Chen, and I. A. Buyanova, "Dynamics of donor bound excitons in ZnO", Applied Physics Letters **102**, 121103 (2013).

[86]T. V. Butkhuzi, T. G. Chelidze, A. N. Georgobiani, D. L. Jashiashvili, T. G. Khulordava, and B. E. Tsekvava, "Exciton photoluminescence of hexagonal ZnO", Phys. Rev. B **58**, 10692–10695 (1998).

[87]M. Bayer, G. Ortner, O. Stern, A. Kuther, A. A. Gorbunov, A. Forchel, P. Hawrylak, S. Fafard, K. Hinzer, T. L. Reinecke, S. N. Walck, J. P. Reithmaier, F. Klopf, and F. Schäfer, "Fine structure of neutral and charged excitons in self-assembled In(Ga)As/(Al)GaAs quantum dots", Phys. Rev. B **65**, 195315 (2002).

[88]E. S. Kumar, F. Mohammadbeigi, L. Boatner, and S. Watkins, "High-resolution photoluminescence spectroscopy of Sn-doped ZnO single crystals", Journal of Luminescence **176**, 47–51 (2016).

[89]D. M. Hofmann, A. Hofstaetter, F. Leiter, H. Zhou, F. Henecker, B. K. Meyer, S. B. Orlinskii, J. Schmidt, and P. G. Baranov, "Hydrogen: A Relevant Shallow Donor in Zinc Oxide", Phys. Rev. Lett. **88**, 045504 (2002).

[90]S. B. Orlinskii, J. Schmidt, P. G. Baranov, V. Lorrmann, I. Riedel, D. Rauh, and V. Dyakonov, "Identification of shallow al donors in al-doped zno nanocrystals: epr and endor spectroscopy", Phys. Rev. B **77**, 115334 (2008).

[91]C. Gonzalez, D. Block, R. Cox, and A. Herve´, "Magnetic resonance studies of shallow donors in zinc oxide", Journal of Crystal Growth **59**, 357–362 (1982).

[92]D. Block, A. Hervé, and R. T. Cox, "Optically detected magnetic resonance and optically detected ENDOR of shallow indium donors in ZnO", Phys. Rev. B **25**, 6049–6052 (1982).

[93]X. Linpeng, "Donor qubits in direct band gap materials", Available at the University of Washington ResearchWorks Archive, PhD thesis (University of Washington, Seattle, WA, USA, 2020).

[94]E. R. Hansen, V. Niaouris, B. E. Matthews, C. Zimmermann, X. Wang, R. Kolodka, L. Vines, S. R. Spurgeon, and K.-M. C. Fu, *Isolation of Single Donors in ZnO*, 2024, arXiv:2310.05806 [cond-mat.mes-hall].

[95]V. Niaouris, M. V. Durnev, X. Linpeng, M. L. K. Viitaniemi, C. Zimmermann, A. Vishnuradhan, Y. Kozuka, M. Kawasaki, and K.-M. C. Fu, "Ensemble spin relaxation of shallow donor qubits in ZnO", Phys. Rev. B **105**, 195202 (2022).

[96]A. V. Rodina, M. Strassburg, M. Dworzak, U. Haboeck, A. Hoffmann, A. Zeuner, H. R. Alves, D. M. Hofmann, and B. K. Meyer, "Magneto-optical properties of bound excitons in ZnO", Phys. Rev. B **69**, 125206 (2004).

[97]V. Niaouris, S. H. D'Ambrosia, C. Zimmermann, X. Wang, E. R. Hansen, M. Titze, E. S. Bielejec, and K.-M. C. Fu, "Contributions to the optical linewidth of shallow donor-bound excitonic transition in ZnO", Optica Quantum **2**, 7–13 (2024).

[98]E. Whiting, "An empirical approximation to the voigt profile", Journal of Quantitative Spectroscopy and Radiative Transfer **8**, 1379–1384 (1968).

[99]G. Zizak, J. D. Bradshaw, and J. D. Winefordner, "Rate equation solution for the temporal behavior of a three-level system", Appl. Opt. **19**, 3631–3639 (1980).

[100]A. V. Khaetskii and Y. V. Nazarov, "Spin-flip transitions between Zeeman sublevels in semiconductor quantum dots", Phys. Rev. B **64**, 125316 (2001).

[101]L. M. Woods, T. L. Reinecke, and Y. Lyanda-Geller, "Spin relaxation in quantum dots", Phys. Rev. B **66**, 161318 (2002).

[102]I. A. Merkulov, A. L. Efros, and M. Rosen, "Electron spin relaxation by nuclei in semiconductor quantum dots", Phys. Rev. B **65**, 205309 (2002).

[103]M. Kroutvar, Y. Ducommun, D. Heiss, M. Bichler, D. Schuh, G. Abstreiter, and J. J. Finley, "Optically programmable electron spin memory using semiconductor quantum dots", Nature **432**, 81–84 (2004).

[104]D. Heiss, M. Kroutvar, J. J. Finley, and G. Abstreiter, "Progress towards single spin optoelectronics using quantum dot nanostructures", Solid State Communications **135**, Fundamental Optical and Quantum Effects in Condensed Matter, 591–601 (2005).

[105]X. Linpeng, T. Karin, M. V. Durnev, R. Barbour, M. M. Glazov, E. Y. Sherman, S. P. Watkins, S. Seto, and K.-M. C. Fu, "Longitudinal spin relaxation of donor-bound electrons in direct band-gap semiconductors", Phys. Rev. B **94**, 125401 (2016).

[106]E. I. Rashba, "Properties of semiconductors with an extremum loop. I. Cyclotron and comninational resonance in a magnetic field perpendicular to the plane of the loop", Fiz. Tverd. Tela **2**, 1224 (1960).

[107]Y. A. Bychkov and E. I. Rashba, "Oscillatory effects and the magnetic susceptibility of carriers in inversion layers", Journal of Physics C: Solid State Physics **17**, 6039–6045 (1984).

[108]L. C. Lew Yan Voon, M. Willatzen, M. Cardona, and N. E. Christensen, "Terms linear in k in the band structure of wurtzite-type semiconductors", Phys. Rev. B **53**, 10703–10714 (1996).

[109]J. D. Zook, "Piezoelectric scattering in semiconductors", Phys. Rev. **136**, A869–A878 (1964).

[110]L. D. Landau and E. M. Lifshitz, *Quantum mechanics: non-relativistic theory. vol. 3* (Pergamon Press, 1977).

[111]O. Madelung, U. Rössler, and M. Schulz, eds., *Landolt-börnstein - group iii condensed matter (ii-vi and i-vii compounds; semimagnetic compounds)*, Vol. 41B (Springer, Berlin, 1999).

[112]E. Janitz, M. K. Bhaskar, and L. Childress, "Cavity quantum electrodynamics with color centers in diamond", Optica **7**, 1232–1252 (2020).

[113]C. Thiel, T. Böttger, and R. Cone, "Rare-earth-doped materials for applications in quantum information storage and signal processing", Journal of Luminescence **131**, Selected papers from DPC'10, 353–361 (2011).

[114]D. B. Higginbottom, F. K. Asadi, C. Chartrand, J.-W. Ji, L. Bergeron, M. L. Thewalt, C. Simon, and S. Simmons, "Memory and transduction prospects for silicon T center devices", PRX Quantum **4**, 020308 (2023).

[115]J. Geng, G. T. Campbell, J. Bernu, D. B. Higginbottom, B. M. Sparkes, S. M. Assad, W. P. Zhang, N. P. Robins, P. K. Lam, and B. C. Buchler, "Electromagnetically induced transparency and four-wave mixing in a cold atomic ensemble with large optical depth", New Journal of Physics **16**, 113053 (2014).

[116]Y.-F. Hsiao, H.-S. Chen, P.-J. Tsai, and Y.-C. Chen, "Cold atomic media with ultrahigh optical depths", Phys. Rev. A **90**, 055401 (2014).

[117]C. Santori, P. E. Barclay, K.-M. C. Fu, R. G. Beausoleil, S. Spillane, and M. Fisch, "Nanophotonics for quantum optics using nitrogen-vacancy centers in diamond", Nanotechnology **21**, 274008 (2010).

[118]N. B. Phillips, A. V. Gorshkov, and I. Novikova, "Optimal light storage in atomic vapor", Phys. Rev. A **78**, 023801 (2008).

[119]B. M. Sparkes, J. Bernu, M. Hosseini, J. Geng, Q. Glorieux, P. A. Altin, P. K. Lam, N. P. Robins, and B. C. Buchler, "An ultra-high optical depth cold atomic ensemble for quantum memories", Journal of Physics: Conference Series **467**, 012009 (2013).

[120]P. Szabó, S. Góger, J. Charry, M. R. Karimpour, D. V. Fedorov, and A. Tkatchenko, "Four-dimensional scaling of dipole polarizability in quantum systems", Phys. Rev. Lett. **128**, 070602 (2022).

[121]B. K. Meyer, J. Sann, S. Eisermann, S. Lautenschlaeger, M. R. Wagner, M. Kaiser, G. Callsen, J. S. Reparaz, and A. Hoffmann, "Excited state properties of donor bound excitons in ZnO", Phys. Rev. B **82**, 115207 (2010).

[122]D. Karaiskaj, M. L. W. Thewalt, T. Ruf, M. Cardona, H.-J. Pohl, G. G. Deviatych, P. G. Sennikov, and H. Riemann, "Photoluminescence of Isotopically Purified Silicon: How Sharp are Bound Exciton Transitions?", Phys. Rev. Lett. **86**, 6010–6013 (2001).

[123]D. Karaiskaj, G. Kirczenow, M. L. W. Thewalt, R. Buczko, and M. Cardona, "Origin of the Residual Acceptor Ground-State Splitting in Silicon", Phys. Rev. Lett. **90**, 016404 (2003).

[124]A. Yang, M. Steger, T. Sekiguchi, M. L. W. Thewalt, J. W. Ager, and E. E. Haller, "Homogeneous linewidth of the ^{31}P bound exciton transition in silicon", Applied Physics Letters **95**, 122113 (2009).

[125]F. Manjón, M. Mollar, M. Hernández-Fenollosa, B. Marí, R. Lauck, and M. Cardona, "Effect of isotopic mass on the photoluminescence spectra of zinc oxide", Solid State Communications **128**, 35–39 (2003).

[126]M. Cardona, "Isotopic Effects in the Phonon and Electron Dispersion Relations of Crystals", physica status solidi (b) **220**, 5–18 (2000).

[127]D. Karaiskaj, M. L. W. Thewalt, T. Ruf, M. Cardona, and M. Konuma, ""intrinsic" acceptor ground state splitting in silicon: an isotopic effect", Phys. Rev. Lett. **89**, 016401 (2002).

[128]A. R. Stegner, H. Tezuka, T. Andlauer, M. Stutzmann, M. L. W. Thewalt, M. S. Brandt, and K. M. Itoh, "Isotope effect on electron paramagnetic resonance of boron acceptors in silicon", Phys. Rev. B **82**, 115213 (2010).

[129]G. T.V., Z. S.M., R. L.N., M. V.A., and B. V.L., "Calculations of the temperature dependences of the band structure and the density of states of hexagonal zinc oxide", Ukr. J. Phys **52**, 458–465 (2007), http://archive.ujp.bitp.kiev.ua/files/journals/52/5/520507p.pdf.

[130]C. W. Thiel, R. M. Macfarlane, Y. Sun, T. Böttger, N. Sinclair, W. Tittel, and R. L. Cone, "Measuring and analyzing excitation-induced decoherence in rare-earth-doped optical materials", Laser Physics **24**, 106002 (2014).

[131]A. Kinos, L. Rippe, A. Walther, and S. Kröll, "Microscopic treatment of instantaneous spectral diffusion and its effect on quantum gate fidelities in rare-earth-ion-doped crystals", Phys. Rev. A **105**, 032608 (2022).

[132]J. J. Longdell, M. J. Sellars, and N. B. Manson, "Demonstration of conditional quantum phase shift between ions in a solid", Phys. Rev. Lett. **93**, 130503 (2004).

[133]C. Santori, D. Fattal, K.-M. C. Fu, P. E. Barclay, and R. G. Beausoleil, "On the indistinguishability of raman photons", New Journal of Physics **11**, 123009 (2009).

[134]J. F. Lilieholm, V. Niaouris, A. Kato, K.-M. C. Fu, and B. B. Blinov, "Photon-mediated entanglement scheme between a ZnO semiconductor defect and a trapped Yb ion", Applied Physics Letters **117**, 154002 (2020).

[135]M. L. K. Viitaniemi, C. Zimmermann, V. Niaouris, S. H. D'Ambrosia, X. Wang, E. S. Kumar, F. Mohammadbeigi, S. P. Watkins, and K.-M. C. Fu, "Coherent spin preparation of indium donor qubits in single ZnO nanowires", Nano Letters **22**, PMID: 35108020, 2134–2139 (2022).

[136]J. M. Smith, S. A. Meynell, A. C. B. Jayich, and J. Meijer, "Colour centre generation in diamond for quantum technologies", Nanophotonics **8**, 1889–1906 (2019).

[137]A. Durand, Y. Baron, W. Redjem, T. Herzig, A. Benali, S. Pezzagna, J. Meijer, A. Y. Kuznetsov, J.-M. Gérard, I. Robert-Philip, M. Abbarchi, V. Jacques, G. Cassabois, and A. Dréau, "Broad diversity of near-infrared single-photon emitters in silicon", Phys. Rev. Lett. **126**, 083602 (2021).

[138]K. De Greve, S. M. Clark, D. Sleiter, K. Sanaka, T. D. Ladd, M. Panfilova, A. Pawlis, K. Lischka, and Y. Yamamoto, "Photon antibunching and magnetospectroscopy of a single fluorine donor in ZnSe", Applied Physics Letters **97**, 241913 (2010).

[139]A. Karasahin, R. M. Pettit, N. von den Driesch, M. M. Jansen, A. Pawlis, and E. Waks, "Single quantum emitters with spin ground states based on cl bound excitons in znse", Phys. Rev. A **106**, L030402 (2022).

[140]S. Strauf, P. Michler, M. Klude, D. Hommel, G. Bacher, and A. Forchel, "Quantum Optical Studies on Individual Acceptor Bound Excitons in a Semiconductor", Phys. Rev. Lett. **89**, 177403 (2002).

[141]J. Melngailis, "Focused ion beam technology and applications", Journal of Vacuum Science & Technology B: Microelectronics Processing and Phenomena **5**, 469–495 (1987).

[142]S. Matsui and Y. Ochiai, "Focused ion beam applications to solid state devices", Nanotechnology **7**, 247 (1996).

[143]A. A. Tseng, "Recent developments in nanofabrication using focused ion beams", Small **1**, 924–939 (2005).

[144]P. J. Moll, "Focused ion beam microstructuring of quantum matter", Annual Review of Condensed Matter Physics **9**, 147–162 (2018).

[145]E. D. Luca, R. Sanatinia, S. Anand, and M. Swillo, "Focused ion beam milling of gallium phosphide nanostructures for photonic applications", Opt. Mater. Express **6**, 587–596 (2016).

[146]Y.-L. D. Ho, R. Gibson, C. Y. Hu, M. J. Cryan, J. G. Rarity, P. J. Heard, J. A. Timpson, A. M. Fox, M. S. Skolnick, M. Hopkinson, and A. Tahraoui, "Focused ion beam etching for the fabrication of micropillar microcavities made of III-V semiconductor materials", Journal of Vacuum Science & Technology B: Microelectronics and Nanometer Structures Processing, Measurement, and Phenomena **25**, 1197–1202 (2007).

[147]M. Manoccio, M. Esposito, A. Passaseo, M. Cuscunà, and V. Tasco, "Focused Ion Beam Processing for 3D Chiral Photonics Nanostructures", Micromachines **12**, 10 . 3390 / mi12010006 (2021).

[148]T. Zhong, J. M. Kindem, J. G. Bartholomew, J. Rochman, I. Craiciu, V. Verma, S. W. Nam, F. Marsili, M. D. Shaw, A. D. Beyer, and A. Faraon, "Optically addressing single rare-earth ions in a nanophotonic cavity", Phys. Rev. Lett. **121**, 183603 (2018).

[149]S. Rubanov and P. Munroe, "FIB-induced damage in silicon", Journal of Microscopy **214**, 213–221 (2004).

[150]S. Rubanov and P. Munroe, "Damage in III–V Compounds during Focused Ion Beam Milling", Microscopy and Microanalysis **11**, 446–455 (2005).

[151]I. Bayn, A. Bolker, C. Cytermann, B. Meyler, V. Richter, J. Salzman, and R. Kalish, "Diamond processing by focused ion beam—surface damage and recovery", Applied Physics Letters **99**, 10.1063/1.3658631 (2011).

[152]F. Sarcan, N. J. Fairbairn, P. Zotev, T. Severs-Millard, D. J. Gillard, X. Wang, B. Conran, M. Heuken, A. Erol, A. I. Tartakovskii, T. F. Krauss, G. J. Hedley, and Y. Wang, "Understanding the impact of heavy ions and tailoring the optical properties of large-area monolayer ws2 using focused ion beam", npj 2D Materials and Applications **7**, 23 (2023).

[153]S. Chakravarthi, C. Pederson, Z. Kazi, A. Ivanov, and K.-M. C. Fu, "Impact of surface and laser-induced noise on the spectral stability of implanted nitrogen-vacancy centers in diamond", Phys. Rev. B **104**, 085425 (2021).

[154]S. B. van Dam, M. Walsh, M. J. Degen, E. Bersin, S. L. Mouradian, A. Galiullin, M. Ruf, M. IJspeert, T. H. Taminiau, R. Hanson, and D. R. Englund, "Optical coherence of diamond nitrogen-vacancy centers formed by ion implantation and annealing", Phys. Rev. B **99**, 161203 (2019).

[155]S. Ourari, Ł. Dusanowski, S. P. Horvath, M. T. Uysal, C. M. Phenicie, P. Stevenson, M. Raha, S. Chen, R. J. Cava, N. P. de Leon, and J. D. Thompson, "Indistinguishable telecom band photons from a single Er ion in the solid state", Nature **620**, 977–981 (2023).

[156]C. Feng, L. Wu, P. Chen, T. Yang, B. Yu, and L. Qian, "Repairing slight damages on monocrystalline silicon surface by thermal annealing", Materials Research Express **8**, 045005 (2021).

[157]N. Aslam, G. Waldherr, P. Neumann, F. Jelezko, and J. Wrachtrup, "Photo-induced ionization dynamics of the nitrogen vacancy defect in diamond investigated by single-shot charge state detection", New Journal of Physics **15**, 013064 (2013).

[158]P. Tamarat, T. Gaebel, J. R. Rabeau, M. Khan, A. D. Greentree, H. Wilson, L. C. L. Hollenberg, S. Prawer, P. Hemmer, F. Jelezko, and J. Wrachtrup, "Stark Shift Control of Single Optical Centers in Diamond", Phys. Rev. Lett. **97**, 083002 (2006).

[159]D. Karaiskaj, J. A. H. Stotz, T. Meyer, M. L. W. Thewalt, and M. Cardona, "Impurity Absorption Spectroscopy in ^{28}Si: The Importance of Inhomogeneous Isotope Broadening", Phys. Rev. Lett. **90**, 186402 (2003).

[160]N. Perret, D. Morris, L. Franchomme-Fossé, R. Côté, S. Fafard, V. Aimez, and J. Beauvais, "Origin of the inhomogenous broadening and alloy intermixing in InAs/GaAs self-assembled quantum dots", Phys. Rev. B **62**, 5092–5099 (2000).

[161]E. Baldit, K. Bencheikh, P. Monnier, J. A. Levenson, and V. Rouget, "Ultraslow Light Propagation in an Inhomogeneously Broadened Rare-Earth Ion-Doped Crystal", Phys. Rev. Lett. **95**, 143601 (2005).

[162]B. Machielse, S. Bogdanovic, S. Meesala, S. Gauthier, M. J. Burek, G. Joe, M. Chalupnik, Y. I. Sohn, J. Holzgrafe, R. E. Evans, C. Chia, H. Atikian, M. K. Bhaskar, D. D. Sukachev, L. Shao, S. Maity, M. D. Lukin, and M. Lon čar, "Quantum Interference of Electromechanically Stabilized Emitters in Nanophotonic Devices", Phys. Rev. X **9**, 031022 (2019).

[163]E. R. Schmidgall, S. Chakravarthi, M. Gould, I. R. Christen, K. Hestroffer, F. Hatami, and K.-M. C. Fu, "Frequency Control of Single Quantum Emitters in Integrated Photonic Circuits", Nano Letters **18**, PMID: 29381364, 1175–1179 (2018).

[164]C. F. de las Casas, D. J. Christle, J. Ul Hassan, T. Ohshima, N. T. Son, and D. D. Awschalom, "Stark tuning and electrical charge state control of single divacancies in silicon carbide", Applied Physics Letters **111**, 262403 (2017).

[165]S. Aghaeimeibodi, C.-M. Lee, M. A. Buyukkaya, C. J. K. Richardson, and E. Waks, "Large stark tuning of InAs/InP quantum dots", Applied Physics Letters **114**, 071105 (2019).

[166]L. C. Bassett, F. J. Heremans, C. G. Yale, B. B. Buckley, and D. D. Awschalom, "Electrical Tuning of Single Nitrogen-Vacancy Center Optical Transitions Enhanced by Photoinduced Fields", Phys. Rev. Lett. **107**, 266403 (2011).

[167]S. Aghaeimeibodi, D. Riedel, A. E. Rugar, C. Dory, and J. Vu čkovi ć, "Electrical Tuning of Tin-Vacancy Centers in Diamond", Phys. Rev. Appl. **15**, 064010 (2021).

[168]E. Merzbacher, *Quantum Mechanics*, 3rd, Chapter 18, Section 4, Page 462 (John Wiley & Sons, Inc., New York, 1998).

[169]W. A. Bowers, "The classical polarizability of the hydrogen atom", American Journal of Physics **54**, 347–350 (1986).

[170]Q. Zhang, J. Qi, Y. Yang, Y. Huang, X. Li, and Y. Zhang, "Electrical breakdown of ZnO nanowires in metal-semiconductor-metal structure", Applied Physics Letters **96**, 253112 (2010).

[171]Benlamri, Mourad and Wiltshire, Benjamin D. and Zhang, Yun and Mahdi, Najia and Shankar, Karthik and Barlage, Douglas W., "High Breakdown Strength Schottky Diodes Made from Electrodeposited ZnO for Power Electronics Applications", ACS Applied Electronic Materials **1**, 13–17 (2019).

[172]B. J. Coppa, R. F. Davis, and R. J. Nemanich, "Gold Schottky contacts on oxygen plasma-treated, n-type ZnO(0001)", Applied Physics Letters **82**, 400–402 (2003).

[173]K. Ip, B. P. Gila, A. H. Onstine, E. S. Lambers, Y. W. Heo, K. H. Baik, D. P. Norton, S. J. Pearton, S. Kim, J. R. LaRoche, and F. Ren, "Improved Pt/Au and W/Pt/Au Schottky contacts on n-type ZnO using ozone cleaning", Applied Physics Letters **84**, 5133–5135 (2004).

[174]M. W. Allen, "Schottky Contact Formation to Bulk Zinc Oxide", Available at the University of Canterbury Library, PhD thesis (University of Canterbury, Christchurch, New Zealand, 2008).

[175]A. M. Hyland, R. A. Makin, S. M. Durbin, and M. W. Allen, "Giant improvement in the rectifying performance of oxidized Schottky contacts to ZnO", Journal of Applied Physics **121**, 024501 (2017).

[176]O. Synhaivskyi, D. Albertini, P. Gaffuri, J.-M. Chauveau, V. Consonni, B. Gautier, and G. Bremond, "Evidence of Piezoelectric Potential and Screening Effect in Single Highly Doped ZnO:Ga and ZnO:Al Nanowires by Advanced Scanning Probe Microscopy", The Journal of Physical Chemistry C **125**, 15373–15383 (2021).

[177]Y. Chen, A. Ryou, M. R. Friedfeld, T. Fryett, J. Whitehead, B. M. Cossairt, and A. Majumdar, "Deterministic Positioning of Colloidal Quantum Dots on Silicon Nitride Nanobeam Cavities", Nano Letters **18**, 6404–6410 (2018).

[178]D. Riedel, H. Lee, J. F. Herrmann, J. Grzesik, V. Ansari, J.-M. Borit, H. S. Stokowski, S. Aghaeimeibodi, H. Lu, P. J. McQuade, N. A. Melosh, Z.-X. Shen, A. H. Safavi-Naeini, and J. Vučković, "Efficient Photonic Integration of Diamond Color Centers and Thin-Film Lithium Niobate", ACS Photonics **10**, 4236–4243 (2023).

[179]N. H. Wan, T.-J. Lu, K. C. Chen, M. P. Walsh, M. E. Trusheim, L. De Santis, E. A. Bersin, I. B. Harris, S. L. Mouradian, I. R. Christen, E. S. Bielejec, and D. Englund, "Large-scale integration of artificial atoms in hybrid photonic circuits", Nature **583**, 226–231 (2020).

[180]V. Heine and C. H. Henry, "Theory of the isotope shift for zero-phonon optical transitions at traps in semiconductors", Phys. Rev. B **11**, 3795–3803 (1975).

[181]J. Puls, F. Henneberger, and J. Voigt, "Excited states of bound excitons in wurtzite-type semiconductors", physica status solidi (b) **119**, 291–298 (1983).

[182]O. Bayrak, I. Boztosun, and H. Ciftci, "Exact analytical solutions to the Kratzer potential by the asymptotic iteration method", International Journal of Quantum Chemistry **107**, 540–544 (2007).

[183]S. B. Doma, A. A. Gohar, and M. S. Younes, "Analytical Solutions of the Molecular Kratzer-Feus potential by means of the Nikiforov-Uvarov Method", Journal of Mathematical Chemistry **61**, 1301–1312 (2023).

[184]D. Dexter, "Theory of the optical properties of imperfections in nonmetals", in *Advances in research and applications*, Vol. 6, edited by F. Seitz and D. Turnbull, Solid State Physics (Academic Press, 1958), pp. 353–411.

[185]R. C. Hilborn, "Einstein coefficients, cross sections, f values, dipole moments, and all that", American Journal of Physics **50**, 982–986 (1982).

[186]E. Nichelatti, "Complex refractive index of a slab from reflectance and transmittance: analytical solution", Journal of Optics A: Pure and Applied Optics **4**, 400–403 (2002).

[187]Josef Plíva, "A Closed Rovibrational Energy Formula Based on a Modified Kratzer Potential", Journal of Molecular Spectroscopy **193**, 7–14 (1999).

[188]W. Rühle and W. Klingenstein, "Excitons bound to neutral donors in InP", Phys. Rev. B **18**, 7011–7021 (1978).

[189]A. R. H. Preston, B. J. Ruck, L. F. J. Piper, A. DeMasi, K. E. Smith, A. Schleife, F. Fuchs, F. Bechstedt, J. Chai, and S. M. Durbin, "Band structure of ZnO from resonant x-ray emission spectroscopy", Phys. Rev. B **78**, 155114 (2008).

[190]M. H. Mohammady, G. W. Morley, A. Nazir, and T. S. Monteiro, "Analysis of quantum coherence in bismuth-doped silicon: A system of strongly coupled spin qubits", Phys. Rev. B **85**, 094404 (2012).

[191]U. Rössler, R. Blachnik, J. Chu, R. Galazka, J. Geurts, J. Gutowski, B. Hönerlage, D. Hofmann, J. Kossut, R. Levy, et al., *II-VI and I-VII Compounds; Semimagnetic Compounds: Supplement to Vols. III/17b, 22a (Print Version) Revised and Updated Edition of Vols. III/17b, 22a (CD-ROM)*, Landolt-Börnstein: Numerical Data and Functional Relationships in Science and Technology - New Series (Springer Berlin Heidelberg, 1999).

[192]M. Cardona and M. L. W. Thewalt, "Isotope effects on the optical spectra of semiconductors", Rev. Mod. Phys. **77**, 1173–1224 (2005).